COUPLING BETWEEN THE NORTH INDIAN

OCEAN AND THE MONSOONS

(A MODEL BASED STUDY OF THE THERMAL STRUCTURE CYCLING

IN THE CENTRAL ARABIAN SEA)

THESIS SUBMITTED TO THE GOA UNIVERSITY

FOR THE DEGREE OF

DOCTOR OF PHILOSOPHY

IN

PHYSICS

BY

RABINDRA KUMAR NAYAK

NATIONAL INSTITUTE OF OCEANOGRAPHY

COUNCIL OF SCIENTIFIC AND INDUSTRIAL RESEARCH
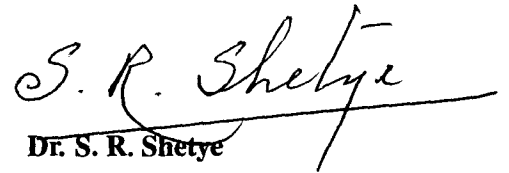
DONA PAULA. GOA. INDIA

2005

to my parents

CERTIFICATE

This is to certify that the thesis entitled "**Coupling between the North Indian Ocean and the Monsoons**" submitted by **Mr. Rabindra Kumar Nayak** for the award of the degree of Doctor of Philosophy in Physics is based on his original studies carried out by him under my supervision. The thesis or any part thereof has not been previously submitted for any other degree or diploma in any university or institution.
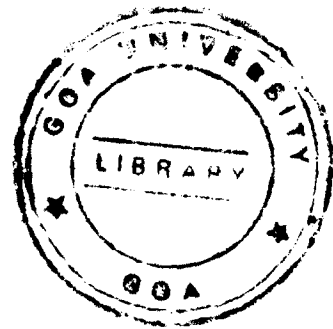
Place: Dona Paula

Date: 29. 5. 06

S. R. Shetye

Dr. S. R. Shetye

Research Guide

Director

National Institute of Oceanography

Dona Paula-403 004, Goa, India.

STATEMENT

As required under the University ordinance 0.19.8 (vi), I state that the present thesis entitled "**The coupling between the North Indian Ocean and the Monsoons**" is my original contribution and the same has not been submitted on any previous occasion. To the best of my knowledge the present study is the first comprehensive work of its kind from the area mentioned.

The literature related to the problem investigated has been cited. Due acknowledgements have been made wherever facilities and suggestions have been availed of.

R. K. Nayak

National Institute of Oceanography, Goa

June 2005

ACKNOWLEDGEMENTS

Contents

Contents   ii

List of Tables

List of Figures

Synopsis

The ocean plays a significant role in determining the Earth's climate and weather through its interaction with the atmosphere. Since it is the radiation from the Sun heating the Earth that drives motion in both these fluids, an understanding of climate and weather, and how they evolve, necessarily requires an understanding of how energy is transported within, and exchanged between, the ocean and the atmosphere. The Indian Ocean is a unique environment having very special dynamics and thermodynamics due to its small size and geographical location (i.e. a tropical basin having no connection with the northern polar seas). The near-surface circulation of the North Indian Ocean (NIO) is driven by the seasonally reversing winds associated with the monsoons. The NIO in turn provides the moisture and energy to drive the summer monsoon. Hence, the ocean and the atmosphere are coupled — they work together to create the monsoon system.

The Arabian Sea of the NIO is an active region of the air-sea interaction processes and plays a major role in driving the monsoon system over the Indian subcontinent. Two important issues about the Arabian Sea have to be noted. (1) The annual evolution of the near-surface layer thermal structure undergoes a unique biannual cycle: the temperature decreases during the monsoonal periods (winter and summer) and it increases during the inter-monsoonal periods (spring and autumn). This is in contrast to the annual march of the near-surface layer thermal structure over most of the world oceans, which do not undergo a summer cooling. (2) The central Arabian Sea is a region of net heat gain across the air-sea interface over a year. It is thus of interest to determine how the heat is transported and ultimately removed from the region.

At small time scales as well as on an annual cycle, the heat budget is a delicate balance between various concurrent processes, namely heat exchange at the surface, turbulent mixing, and horizontal and vertical advection. To quantify these processes, time-series of high frequency observations of both the atmosphere and the ocean are required. Such data, over a full annual cycle, have been lacking for a long time, and the numerous studies carried out in the past to examine the above two issues have been based on climatologies. Thus, there has been some uncertainties regarding the role of local air-sea interaction versus ocean processes in the observed annual evo-

lution of upper ocean properties and the heat balance of the Arabian Sea as a whole. Recently, a field study of moored-array observations was carried out in the central Arabian Sea at (61.5° E, 15.5°N) during October 1994 to October 1995 under the US Joint Global Ocean Flux Studies (JGOFS) programme with the aim of quantifying the contributions of various processes to the annual evolution of the upper ocean thermal structure. An accurate, year-long, high frequency, concurrent time-series data of atmospheric-forcing fluxes and upper ocean response thus became available.

In the recent past, these data were used to describe the temperature evolution and to estimate the contribution of the various terms of the heat budget. The difficulty with such an approach is that all processes are at work simultaneously. Its success thus rely on accurate observation of each process. A concurrent fruitful approach is to use a model, to predict explicitly each process. The observations are used to force the model as well as to constrain or validate its predictions.

A critical feature of the above time-series, is that the high frequency data is essentially available at a single point. The vertical dimension is thus strongly privileged. This naturally calls for the use of a one dimensional mixed-layer physics model. To account for horizontal and vertical advection, such a model has to be forced with the estimates of the corresponding contributions.

In view of the above, this thesis has three goals. The first goal is to achieve a proper simulation of the seasonal cycle of the upper ocean thermal structure in the central Arabian Sea at the location of JGOFS moored-array observations. For this an upper-ocean thermodynamical model will be forced with atmospheric fluxes at the surface and advective heat fluxes will be prescribed in order to correct the prediction. The second goal is to use the model simulation to achieve a diagnostic of the processes contributing to the seasonal heat budget. The third goal is to examine the sensitivity of the thermal structure to auxiliary parameters that are not generally accounted for (these include salinity and biomass concentration), and to various surface forcing fluxes: momentum fluxes (wind stress), heat fluxes (fluxes of solar radiation and infrared radiation, and turbulent latent and sensible heat fluxes).

After presenting the introduction of the thesis in chapter 1, a brief overview of the ocean-atmosphere coupled system with emphasis on the NIO, the background knowledge for the present study, is presented in chapter 2.

The data and methods used in the thesis is described in chapter 3. To examine the role of various intervening processes in controlling the upper ocean thermal structure in the central Arabian Sea, a 1-D mixed-layer model based on turbulent closure scheme is forced by atmospheric fluxes and advective heat fluxes over the one-year period of the JGOFS time-series starting from

mid-October 1994 in the central Arabian Sea at (61.5°E & 15.5°N). Atmospheric forcing data are available from the moored array observations. The horizontal advective contributions at the study location are available from two different sources. The first estimate is based on local *in situ* measurements. The second estimate is based on optimally interpolated satellite SST field and *in situ* currents. The vertical velocity, as in all oceanography problem, poses a challenge. Two possible approaches have been considered for the diagnostic analysis. In the first approach, the model was used to predict the temperature profile (using atmospheric fluxes and estimates of horizontal and vertical advection). In the second approach, the observed temperature profiles (and atmospheric fluxes and estimates of horizontal advection) were used to force the model in order to predict the vertical velocity.

Several numerical experiments, using the above two approaches, are described in chapter 4. Besides the main experiments, several additional experiments were also performed for two purposes: (i) to support the analysis of the results obtained from the main experiments, and (ii) to examine the role of auxiliary parameters (salinity and biomass) in the seasonal evolution of upper-ocean temperature. The model-based heat-budget analysis for the four monsoon seasons: winter, spring, summer, and autumn has been carried out in chapter 5.

The thesis is concluded by summarizing the results, and by describing outlines of some future research areas where the present study can help. The following are the important conclusions of the thesis.

(1) Vertical advection is an important process, as important as atmospheric fluxes and horizontal advection, throughout the year in controlling the upper ocean thermal structure and the heat budget of the central Arabian Sea.

(2) The general trends of ML deepening and SST cooling in the central Arabian Sea during the NE monsoon are due to buoyancy driven convective entrainment mixing, whereas the trends of ML deepening and SST cooling during the SW monsoon are due to both wind driven mixing and buoyancy driven convective mixing. However, the observed trends of ML and SST during the whole year can only be reproduced when all the intervening process are accounted for: advection together with atmospheric fluxes.

(3) Ocean dynamics plays a primary role in controlling the thermodynamics of the upper ocean in the central Arabian Sea, whereas salinity and phytoplankton biomass concentration evolution do not have a significant control over the thermal structure.

(4) Some results of the present study have their validity limited by the uncertainties in Fischer-based horizontal advective heat fluxes. The deployment of a four/five mooring system to quantify

the contributions of horizontal variability is believed not to be satisfactory as far as quantitative estimation is concerned. The information obtained from the central mooring in combination with satellite altimeter imagery proves to be at least as good, and may be better.

At the end of this thesis, we do not know whether the conclusions obtained for the central Arabian Sea are still valid in other parts of the Arabian Sea. This issue still remains an open question. This can be answered by achieving similar model-based diagnostic studies or by carrying out a basin scale study using a 3D model.

This model can be used for studies similar to those presented in this thesis to understand the eastern and southeastern Arabian Sea, where time-series observation were carried out during the Arabian Sea Monsoon Experiment (ARMEX) during 2002–2003.

Thermodynamics of the ocean influences the biogeochemical system of the ocean environment. Another perspective is to couple a biogeochemical model to an upper ocean thermodynamical model to perform a simulation of carbon and nitrogen fluxes along an annual cycle in the central Arabian Sea.

Chapter 1

Introduction

The ocean plays a significant role in determining the Earth's climate and weather through its interaction with the atmosphere. Since it is the radiation from the Sun heating the Earth that drives motion in both these fluids, an understanding of climate and weather, and how they evolve, necessarily requires an understanding of how energy is transported within, and exchanged between, the ocean and the atmosphere. The Indian Ocean (see Fig. 1.1) is a unique environment having very special dynamics and thermodynamics due to its small size and geographical location (i.e. a tropical basin having no connection with the northern polar seas). The near-surface circulation of the North Indian Ocean (NIO) is driven by the seasonally reversing winds associated with the monsoons. The NIO in turn provides the moisture and energy to drive the summer monsoon. Hence, the ocean and the atmosphere are coupled — they work together to create the monsoon system. A brief overview of this system is presented in sections 2.1 and 2.2.

The Arabian Sea, the western half of the NIO (see Fig. 1.2), is an active region of air-sea interaction processes and plays a major role in driving the monsoon system over the Indian subcontinent. Two important issues about the Arabian Sea have to be noted. (1) The annual evolution of the near-surface layer thermal structure undergoes a unique biannual cycle: temperature decreases during the monsoonal periods (winter and summer) and increases during the inter-monsoonal periods (spring and autumn). This is in contrast to the annual march of the near-surface thermal structure in most of the world ocean, which do not undergo summer cooling. (2) The central Arabian Sea is a region of net heat gain across the air-sea interface over a year. It is thus of interest to determine how the heat is transported and ultimately removed from the region.

At small time scales as well as on an annual cycle, the heat budget is a delicate balance between various concurrent processes, namely heat exchange at the surface, turbulent mixing, and horizontal and vertical advections. To quantify these processes, high-frequency time-series obser-

1
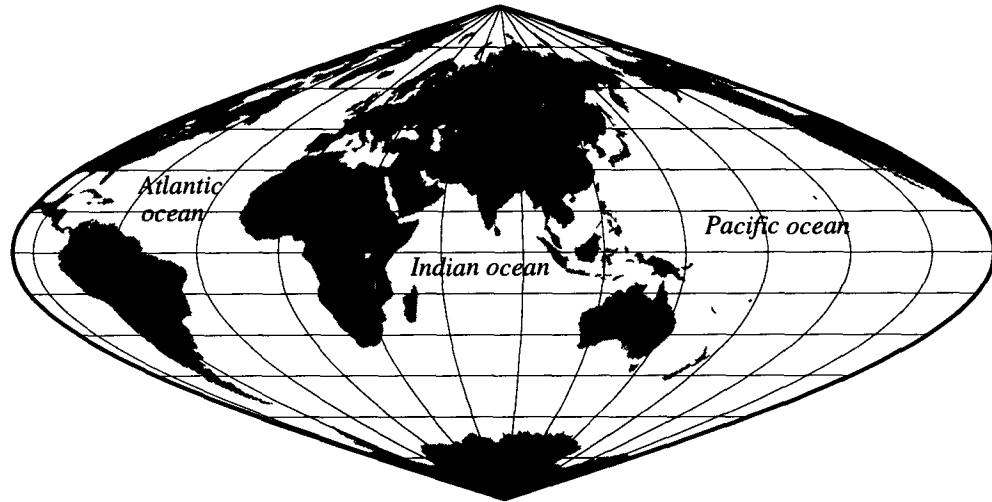
Figure 1.1: The geography of the Indian Ocean. The zonal extent of the Indian Ocean is much less than that of the Pacific or the north Atlantic. Its southern boundary is arbitrary, but is chosen to distinguish it from the Antarctic, or southern, Ocean. Unlike the Pacific and the Atlantic, the Indian Ocean is bounded in the north by Asia; this makes it a tropical basin. This has profound consequences for the meteorology and oceanography of this region: the land-ocean contrast forces seasonally reversing winds, the monsoons, over the north Indian Ocean, unlike in the north Atlantic or the north Pacific.
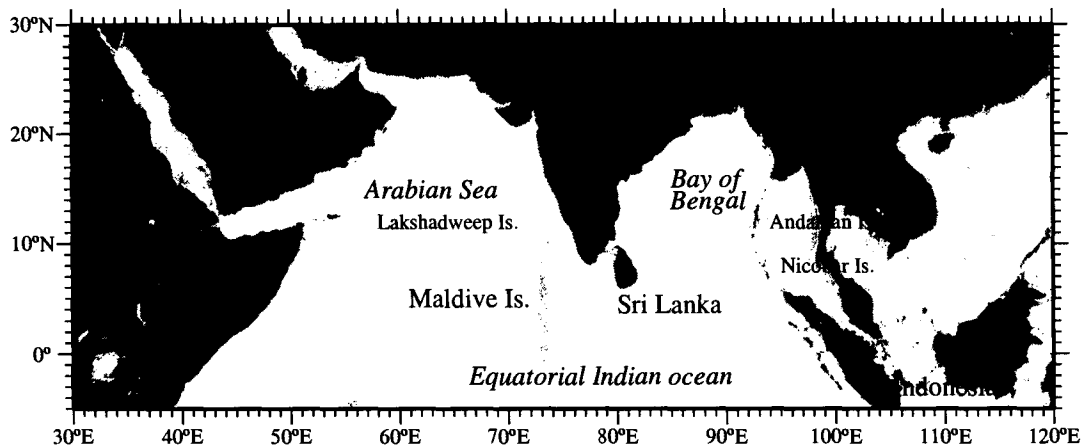
Figure 1.2: The domain of the North Indian Ocean (NIO). The Indian subcontinent divides the NIO into two semi-enclosed tropical basins, the Arabian sea and the Bay of Bengal.

vations of both atmosphere and ocean are required. Such data, over a full annual cycle, have been lacking for a long time, and the numerous studies carried out in the past to examine the above two issues have been based on climatologies (see section 2.2.2). Thus, there has been some uncertainty regarding the role of local air-sea interaction versus ocean processes in the observed annual evolution of upper ocean properties and the heat balance of the Arabian Sea as a whole.

Recently, a field study was carried out during October 1994 to October 1995 in the central Arabian Sea as a part of the US Joint Global Ocean Flux Studies (JGOFS) programme with the aim of quantifying the contributions of various processes (surface forcing, horizontal and vertical advective processes) to the annual evolution of upper ocean thermohaline structure in the Arabian Sea (see Fig. 1.3). The location of the moorings, centred at (61.5° E and 15.5°N) was selected for its proximity to the climatological axis of the atmospheric Findlater Jet (Findlater [1]) (the area of strongest surface forcing) and for its distance from the complicating effects of the coast. An array of five moorings was deployed, forming a square of approximately 50 km on a side with a fifth mooring located in the centre. Surface meteorological and sub-surface oceanographic instrumentation mounted on the central mooring yielded the first concurrent, high-quality record of atmospheric forcing and upper-ocean response over a monsoonal cycle (Weller et al. [2] and Weller et al. [3]). Three of the four corner moorings provided temperature profiles over most of the study period. Using the same time-series, Fischer et al. [4] estimated the heat fluxes due to horizontal advection in the upper 125 m layer using the current measurements on the central mooring and the horizontal temperature gradient estimated from the combinations of all mooring data.

These data were used to describe the temperature evolution and to estimate the contribution of the various terms of the heat budget (Weller et al. [3]; Fischer et al. [4]). The difficulty with such an approach is that all processes are at work simultaneously. Its success thus relies on accurate observation of each process. An alternative approach is to use a model to predict explicitly each process. The observations are used to force the model as well as to constrain or validate its predictions.

A critical feature of the above time-series is that the high-frequency data are essentially available at a single point. The vertical dimension is thus strongly privileged. This naturally calls for the use of a one-dimensional mixed-layer physics model. To account for horizontal and vertical advection, such a model has to be forced with estimates of the contributions of these processes.

In view of the above, this thesis has three goals. The first goal is to achieve a proper simulation of the seasonal cycle of the upper ocean thermal structure in the central Arabian Sea at the location

of JGOFS moored-array observations. For this an upper-ocean thermodynamical model will be forced with atmospheric fluxes at the surface and advective heat fluxes will be prescribed in order to correct the prediction. The second goal is to use the model simulation to achieve a diagnostic of the processes contributing to the seasonal heat budget. The third goal is to examine the sensitivity of the thermal structure to auxiliary parameters that are not generally accounted for (these include salinity and biomass concentration), and to various surface forcing fluxes: momentum fluxes (wind stress), heat fluxes (fluxes of solar radiation and infrared radiation, and turbulent latent and sensible heat fluxes).

The thesis is divided into five chapters (including this introduction). A brief overview of the ocean-atmosphere coupled system (with emphasis on the NIO), the background knowledge for the present study, will be presented in chapter 2. (A reader desirous of going straight to the new results may skip this chapter.) The data and methods used in the thesis will be described in chapter 3. Several numerical experiments are carried out to simulate the thermal structure at the moored-array location. These experiments and their results form the subject of chapter 4. The heat-budget analysis (based on our simulations) are presented in chapter 5. The final chapter provides concluding remarks.
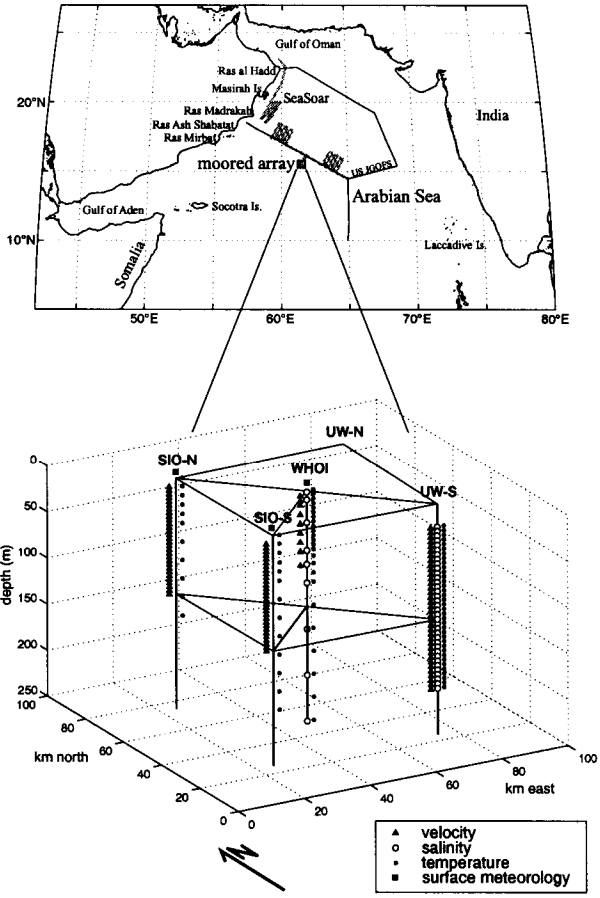
Figure 1.3: Location of Arabian sea moored-array observations during October 1994 to October 1995 (adopted from Fischer et al. [4])

Chapter 2

The background

A brief overview of the coupled ocean-atmosphere system is presented at the beginning of this chapter. The focus will then shift to the monsoon climate system of the NIO.

2.1 The coupled ocean— atmosphere system

The ocean plays a significant role in determining the Earth's climate and weather through its interaction with the atmosphere. Since it is the radiation from the Sun heating the Earth that drives motion in both these fluids, an understanding of climate and weather, and how they evolve, necessarily requires an understanding of how energy is transported within, and exchanged between, the ocean and the atmosphere. The following sections provide a description of these topic; much of what follows is based on Peixoto and Oort [5] and Houghton et al. [6].

2.1.1 The components of the Earth's climate system

Weather can be defined as the state of the atmosphere at a given location. It is characterized by short-lasting meteorological events (with a typical time scale of a few days). Climate proceeds from the average weather patterns over at least a score of years (based on higher momentum statistics) modulated by the seasonal cycle. The state of the atmosphere is determined by state parameters such as density, temperature, pressure, moisture, etc. The atmosphere is an open thermodynamical system that exchanges matter and energy with its environment at its boundary. The oceans, the land surface, the biosphere, and the cryosphere (sea- and land-ice) are open thermodynamical systems, and all together constitute the environment of the atmosphere. Complex interactions are at work between these systems. Complex feedback mechanisms within the individual systems respond to internal stability. Any change in the state of any of the systems can induce

6
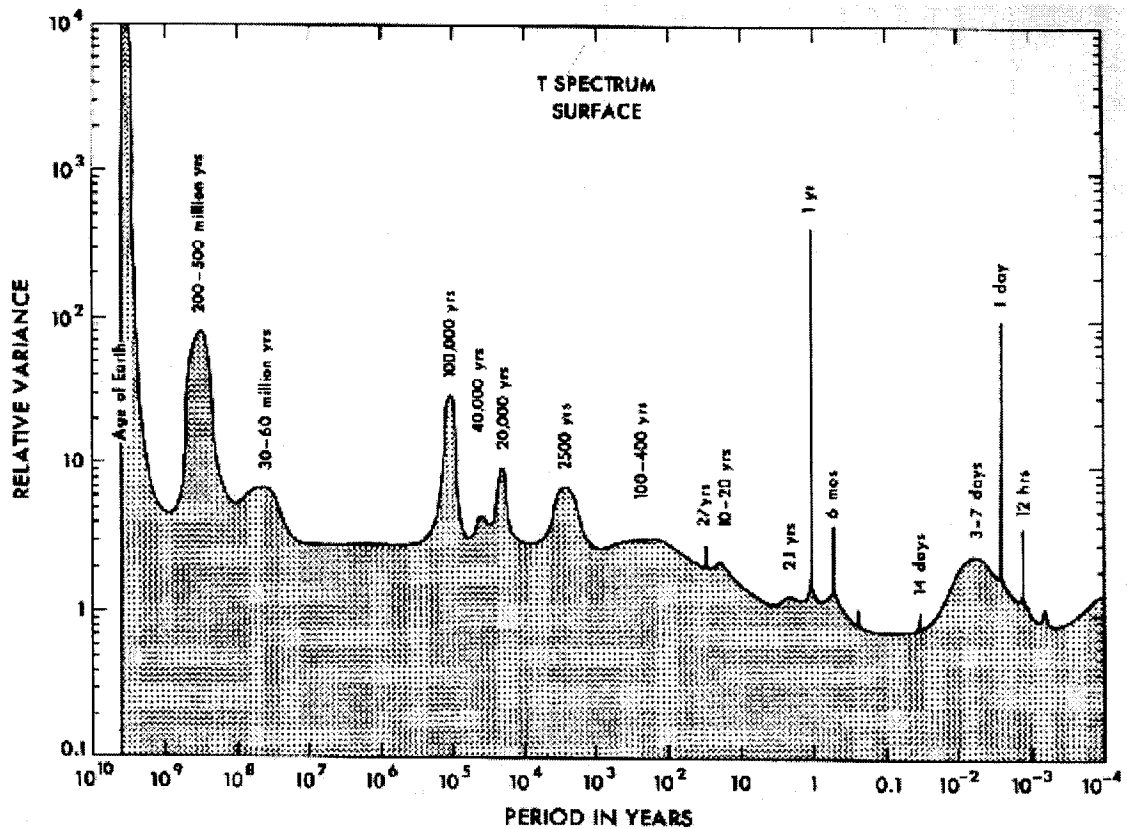
Figure 2.1: Idealized, schematic spectrum of atmospheric temperature between $10^{-4}$and 10^{10}year [after Peixoto and Oort [5], their Fig. 2.7]

some change (fluctuation) in the adjacent components. All these interlinked component-systems form the Earth's climate system with the atmosphere as the central component in which we live.

The interaction of the atmosphere with other components of the Earth's climate system can take a number of forms which induce a number of processes at time scales ranging from very small scales (fraction of a second) to very large scales (tens of thousands of years or even more). This is evident from the observed spectrum of the surface air temperature during its past history as evaluated by Mitchell [7] (Fig. 2.1). Analysis of the spectrum shows several spikes and broader peaks. The spikes correspond to astronomically dictated, strictly periodic climate variations, such as the diurnal and annual variations and their harmonics, whereas the broad peaks represent variations that are, according to Mitchell [7], either quasi-periodic or aperiodic, with, however, a preferred time scale of energization. Many of these broad peaks cannot be directly explained by the known external forcing. This indicates strong coupling between the atmosphere and other components of the earth's climate system or internal feedback mechanisms within the atmosphere itself.

2.1.2 The ocean as the flywheel for the Earth's climate system

The major energy source and sink of of the climate system are the solar and the terrestrial radiations respectively. The energy from the Sun is received in the form of radiation, with nearly all energy in between 0.2 and 4 μm. Some solar radiation is either absorbed or scattered by the atmospheric gases, water vapour, particles, and clouds, the remaining is either absorbed or reflected by the Earth's surface.

The amount of solar radiation reflected or scattered into space without any change in wavelength is defined as the albedo of the surface. The albedo varies in space and time and also varies for different surface types. The albedo of the ocean is significantly smaller than that of land. The mean global albedo is 30%. The remaining 70% of the incoming solar radiation must be absorbed. Of this remaining flux, about three-quarters (about half of the total incoming flux) penetrates the atmosphere and is absorbed by the Earth's surface. The remainder (i.e. 16% of the total incoming flux) is absorbed directly by the atmosphere. Both the atmosphere and the surface re-radiate this absorbed energy as long-wave radiation.

How the solar radiation is absorbed at the Earth's surface differs profoundly on land and at sea. On land, most of the energy is absorbed close to the surface (a few centimetres). The near surface warms up rapidly, leading to increase of outgoing terrestrial radiation (long wave). At sea, the solar radiation penetrates much deeper, with 20% reaching a depth of 10 m or more. Turbulent diffusion can transport heat from surface to sub-surface layers. So the sea is heated to a much greater depth and the surface warms up much more slowly. The ocean also has a large thermal inertia and it can store heat for a long period, from several months to several years (in contrast to the period of minutes to a few hours exhibited by land). This implies that more energy is stored in the top layer of the ocean and less is lost to space in the form of long-wave radiation. This absorptive capacity of the oceans plays an important part in the dynamics of the Earth's climate system. In effect, ocean act as a huge climatic flywheel, damping down fluctuations in other parts of the climate of the globe.

Because the atmosphere and the oceans transport energy from one place to another, this motion is an integral part of the Earth's radiation balance. On a global scale the most important feature is that, while most solar energy is absorbed at low latitudes (net radiation balance toward the earth), a large amount of energy is radiated toward space at high latitudes (net radiation balance away from the earth). This loss must be balanced by energy transport from lower latitudes. This provides the energy to fuel the engine that drives the global atmospheric and oceanic circulation throughout the year. Peixoto and Oort [5] show that both atmosphere and ocean transport about the same amount

of energy pole-ward. It can be noted that the oceanic component of the meridional heat transport is significantly larger in the tropical region than the atmospheric component, while the opposite occurs in the mid-latitude regions. As regard the oceanic heat transports, the Atlantic carries more heat north-ward than the Pacific. In the southern hemisphere the Pacific transports roughly twice as much energy south-ward than the Indian Ocean, while the Atlantic has a small negative effect, carrying energy north-ward across the Equator.

An interesting feature of the Indian ocean is that the meridional heat transport in the northern basin is negative (toward the equator) in contrast to the other oceans. This is because the Indian Ocean, unlike the other oceans, is blocked by the land masses of the Asian continent to the north around 25° N. The meridional heat transport toward the south pole in the Indian Ocean is smaller than in the other oceans. These unique features of the Indian Ocean have important consequences for the climate of the surrounding regions.

The role of the oceans in the meridional heat transport process cannot be thought as independent of the atmosphere. There is continual exchange of energy in the form of heat, momentum (as winds stir up waves), and moisture (in the form of evaporation and precipitation). This energy flux is particularly large in the vicinity of the major currents, and where cold polar air moves to lower latitudes over warmer water. These regions are the breeding grounds of many of the storm systems that are a feature of the mid-latitude weather.

Maintaining an energy balance by transport from low to high latitudes has another fundamental implication. This relates to the mean temperatures of different latitude belts. Although these temperatures can fluctuate by a certain amount at any time of the year, they will be close to the current climatic normal. Moreover, if one region is experiencing exceptional warmth, adjacent regions at the same latitudes will experience compensating cold conditions. This means that, at short scales, climatic fluctuations are principally a matter of regional patterns. These are often the product of the occurrence of certain extremes (e.g. cold winters, hot summers, droughts, and excessive rainfall) becoming more frequent than usual, but in the long term, it is possible for mean latitudinal temperatures to vary while maintaining the global energy balance. For the most part, however, these overall changes are small compared to the regional fluctuations.

In view of the above description, it is clear that the ocean plays a significant role, in fact a regulating role, in the earth's weather and climate through its interaction with the atmosphere. Understanding this air-sea interaction process at global as well as regional scales is fundamentally important for understanding and predicting the weather and climate of the Earth. In what follows, some specific aspects of these processes will be described.

2.1.3 Air-sea coupling processes and sea surface temperature

The interface between the ocean and the atmosphere is dynamic. Matter and energy are continually being transferred in both directions (see Fig. 2.2). Matter exchange takes place through freshwater flux in the form of evaporation from ocean to atmosphere and of precipitation from atmosphere to ocean. Energy can be exchanged between the two systems in the form of fluxes of momentum, radiation, and heat. The characteristics of these energy fluxes are as follows.

1. Momentum (kinetic energy): The atmosphere supplies energy to the upper ocean by transferring momentum through wind stress. This momentum exchange creates ocean waves and currents, which are mainly responsible for the transport of heat and momentum in the ocean. In contrast, the ocean plays a very sluggish role in momentum transfer to the atmosphere.

2. Radiation: (a) Solar short-wave radiation enters the ocean and constitutes the main energy source for the ocean; (b) long-wave radiation is exchanged between the ocean and the atmosphere in both directions. As far as net long-wave radiation is concerned, it is from the ocean to the atmosphere.

3. Turbulent heat exchanges: There are two ways for energy to be exchanged in the form of turbulent heat fluxes. (a) The sensible heat flux (conduction process) can be exchanged in either of the directions depending on the difference between sea surface temperature (SST) and the temperature of the overlying atmosphere. If the difference is positive, heat flows to the atmosphere. (b) Latent heat flux: In the process of evaporation heat is carried by the water molecules in latent form from the ocean surface to the atmosphere. (This depends on SST, wind speed, and the moisture content of the atmosphere.) The net result is a cooling of the ocean surface.

These flux exchanges are the mediators of the coupling processes, which drive many physical processes (in space and time scales) inside both the systems. These fluxes are directly and indirectly related to SST, which is thus an important indicator of these coupled processes, and hence many investigators put forth their efforts to understand the links between the SST and the various air-sea interaction processes. Some of these studies are reviewed below.

Air-sea interaction is most intense in the tropics (Oceanography Course Team [8]). The intensity of the Hadley circulation and the position of the Inter-Tropical Convergence Zone (ITCZ) are dependent on SST (Bjerknes [9] & [10]). Numerous studies (Gray [11], McBride [12], Briegel and Frank [13], etc.) indicate that SST is crucial for the development and intensification of tropical

cyclones. Tropical cyclones are observed to form only when the SST is greater than 26.5°C, and passage over cooler water causes them to lose intensity. In reverse, cyclones affect the ocean surface/SST, causing strong surface cooling (through an enhanced mixing, owing to string winds, of cooler sub-surface waters with the surface waters) that can then act to limit the intensity of subsequent cyclones. Lindzen and Nigam [14] suggest that SST gradients are important in determining the location of precipitation over the tropics, including the monsoon region.

On longer time-scales, ocean-atmosphere interactions occur on large spatial scales. The main mode of oscillation on time-scales of a year or more is the El-Niño/Southern Oscillation phenomenon (ENSO). The phase of ENSO (El Niño or La Niña) strongly influences the formation of tropical cyclones in many formation regions. In the Atlantic, during an El Niño (La Niña) event, vertical wind shear is increased (reduced) as a result of stronger (weaker) upper-level wind-shear westerlies over the Caribbean basin and tropical Atlantic (Gray [15], Goldenberg and Shapiro [16]). In the western North Pacific, the relationship with ENSO is weak, but, it still exists (Lander [17], Chan [18]), as for the relationship in the central North Pacific (Chu and Wang [19]). In the south-west Pacific, El Niño causes strong changes in the regions of storm formation, again largely associated with changes in the typical vertical wind shear (Hastings [20], Evans and Allan [21], Basher and Zheng [22]). A similar relationship exists between El Niño and the number of tropical cyclones off the western coast of Australia (Broadbridge and Hanstrum [23]). These changes are fundamentally driven by the large-scale variation in the SST patterns. These cause the zones of cyclone formation to shift eastwards, away from the coast of Australia. The opposite pattern is typically observed in La Niña years. These relationships are used as the basis of a number of statistically-based seasonal forecasting schemes of tropical cyclone formation for various regions of the globe (Gray [24], Elsner et al. [25], Chan et al. [26])

(While SST plays a highly significant role in controlling the climate and weather of the tropical regions, its effect at higher latitudes cannot be ignored. The most frequent mid-latitude (frontal) disturbances are mostly driven by sensible heating (temperature difference between the sea surface and the overlying atmosphere) (Oceanography Course Team [8])).

2.1.4 SST and the concept of mixed layer

Numerous factors affect SST. The local air-sea fluxes have a very direct and strong control. Besides local-air sea fluxes, SST is also controlled by internal processes occurring in the ocean. These processes include horizontal advection, vertical advection (upwelling and downwelling), and vertical diffusion. Horizontal diffusion of heat is much slower in the ocean. How these processes work
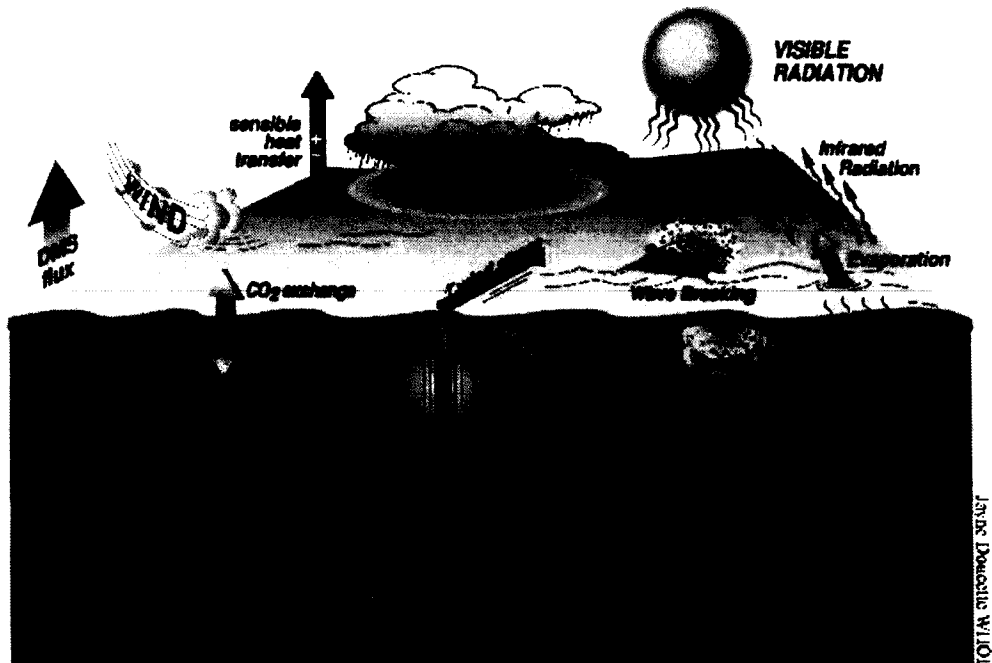
Figure 2.2: A schematic of various processes active in the upper ocean (NOAA [27])

together in the ocean is presented schematically in Fig. 2.2.

The surface mixed layer is a quasi-homogeneous layer (also known as oceanic boundary layer), the site of active air-sea exchange formed in the top layers of the ocean owing to quasi-balance among the various forcing fluxes. Forcing from winds, heating and cooling, and rainfall and evaporation, have a profound influence on the distribution of mass, energy, and momentum in the ocean. Although the effects from this wind and buoyancy forcing are ultimately felt throughout the ocean, the most immediate impact is in the surface mixed layer. The mixed layer is warmed by solar (short-wave) radiation and cooled by (long-wave) radiation emitted from the surface and by latent heat loss due to evaporation. The mixed layer tends to be cooled by sensible heat loss since the surface air is generally cooler than the ocean surface. Evaporation and precipitation change the mixed-layer salinity. These salinity and temperature changes define the surface buoyancy. As the surface loses buoyancy, it becomes denser than the sub-surface waters, causing convective overturning and mixing. Wind forcing can also cause surface overturning and mixing, as well as localized overturning at the base of the mixed layer through shear-flow instability. This wind- and buoyancy-generated turbulence causes the surface water to be well-mixed and leads to vertically uniform temperature, salinity, and density profiles. Furthermore, turbulence can entrain deeper water into the surface mixed layer, causing the surface temperature and salinity to change and the layer of well-mixed, vertically uniform water to thicken. Wind forcing can also set up oceanic

currents and cause changes in the mixed-layer temperature and salinity through horizontal and vertical advection.

Salinity affects the thermal structure by affecting the density field. Density is a strong function of temperature and a weak function of salinity (see Appendix-A). Furthermore, the salinity of the upper ocean usually varies very slowly in space and time. Therefore, in most cases, salinity does not have much control over the thermal field. However, there are some situations where the salinity has strong control over the thermal field. This is due to the so-called "barrier layer" (BL) phenomenon (Vialard and Delecluse [28]). A BL is present when the isohaline layer is shallower than the isothermal layer. In such a case, the mixed-layer (ML) depth is controlled by salinity stratification. The under lying water has a potential temperature close to the SST. A deepening of the ML (e. g., under the effect of a wind burst) will not affect surface temperature via entrainment cooling. This is why the water column between the bottom of the ML and the top of the thermocline has been named barrier layer: it acts as a barriers to cooling owing to entrainment. Using the data from Levitus [29], the presence of the BL in the three tropical oceans has been recognized to be not just a sporadic event but a climatological feature (Sprintall and Tomczack [30]). Moreover, a strong time variability of the BL has been observed and linked to inter-annual variability (Delcroix et al. [31]; Sprintall and Mcphaden [32]). Vialard and Delecluse ([28] & [33]) examined the role of salinity in the formation of the tropical Pacific warm pool. They showed that there are occasions of formation of BL in the equatorial region due to very large bursts of fresh-water flux owing to heavy rain events. The indirect study by Shenoi et al. [34] suggests that salinity stratification has a significant effect on the surface layer heat budget of the Bay of Bengal (eastern NIO), while it has a negligible role in the Arabian Sea (western NIO). The recent model study by Durand et al. [35] has shown that the SST of the eastern Arabian Sea increased by 1.1°C during November–March owing to the presence of a BL below the mixed layer, whereas the atmospheric fluxes cooled the surface by 0.3°C over the same period.

Another important issue related to mixed-layer processes study is the impact of biomass (chlorophyll concentration) on the thermodynamics of the upper ocean through the vertical atten-uation of solar irradiance. When biomass concentration increases, the solar irradiance is trapped within a thinner upper layer. This stabilises the ML by reducing the vertical mixing due to con-vection and wind mixing, and it increases the SST. In reverse, biomass is affected by the local thermodynamics. Such a study was done for the Arabian Sea by Sathyendranath et al. [36] using a coupled bio-optical/physical model. They showed that the rate of biological heating effect is significant (upto 4.0 °C month^{-1}) during the August.

2.2 Coupling between the North Indian Ocean and the Monsoons

The portion of the Indian Ocean that lies north of 10°S is considered here as the North Indian Ocean (NIO) (see Fig. 2.3). The NIO is a small tropical basin, closed by the land masses of south-Asian countries in the north around 25°N. The tropical part of the NIO is divided by the Indian subcontinent into two semi-enclosed basins, the Arabian Sea and the Bay of Bengal. Unlike other world oceans (Atlantic and Pacific), the NIO has no connection to the northern polar seas. This unique size and geographical location has significant consequences for the climate of the surrounding regions. The differential heating between the NIO and the surrounding land masses with the seasonal movement of the Sun causes a north-south pressure gradient. This pressure gradient drives the seasonally reversing (monsoon) winds over the NIO (see Figure 2.3a-b). The monsoon winds generally blow from the south-west during May–September (the SW monsoon or summer monsoon) and from the north-east during November–February (the NE monsoon or winter monsoon), March–April and October being the months of transition with weak winds. The winds are stronger during summer than during winter. Since the SW monsoon winds blow from the NIO to the land, they are loaded with moisture and this brings heavy precipitation to the coastal region. Rainfall during the SW monsoon is the major source of freshwater in the coastal region of the NIO (including India). The NE monsoon winds blow from land to the ocean; hence they are basically dry and do not cause significant rainfall over the Indian sub-continent (except over south-east India). Of the two monsoon seasons, the summer and the winter, the summer (SW monsoon) is particularly important for India. The monsoonal activities over the Indian subcontienent are strongly dependent on the thermodynamical state of the NIO. During the SW monsoon, the SST over the major part of the tropical NIO are warmer than 28°C (a threshold for the atmospheric instability over tropical Indian ocean) (Gadgil et al. [37]). In contrast, during the NE monsoon, the SST over the major part of the tropical NIO remains below the threshold value (see Fig. 2.3c-d).

Numerous attempts were made in the past to understand the various aspects of the Indian summer monsoon (which include genesis, onset, and intensification) and its possible link to the thermodynamical state of the NIO. Reviews of such studies were published by Webster et al. [38], in the Science Plan of the Indian Climate Research Programme [39], and in the monograph by Varadachari [40]. In the following section, some of the important aspects of the Indian summer monsoon (ISM) (air-sea coupling processes) are briefly described .
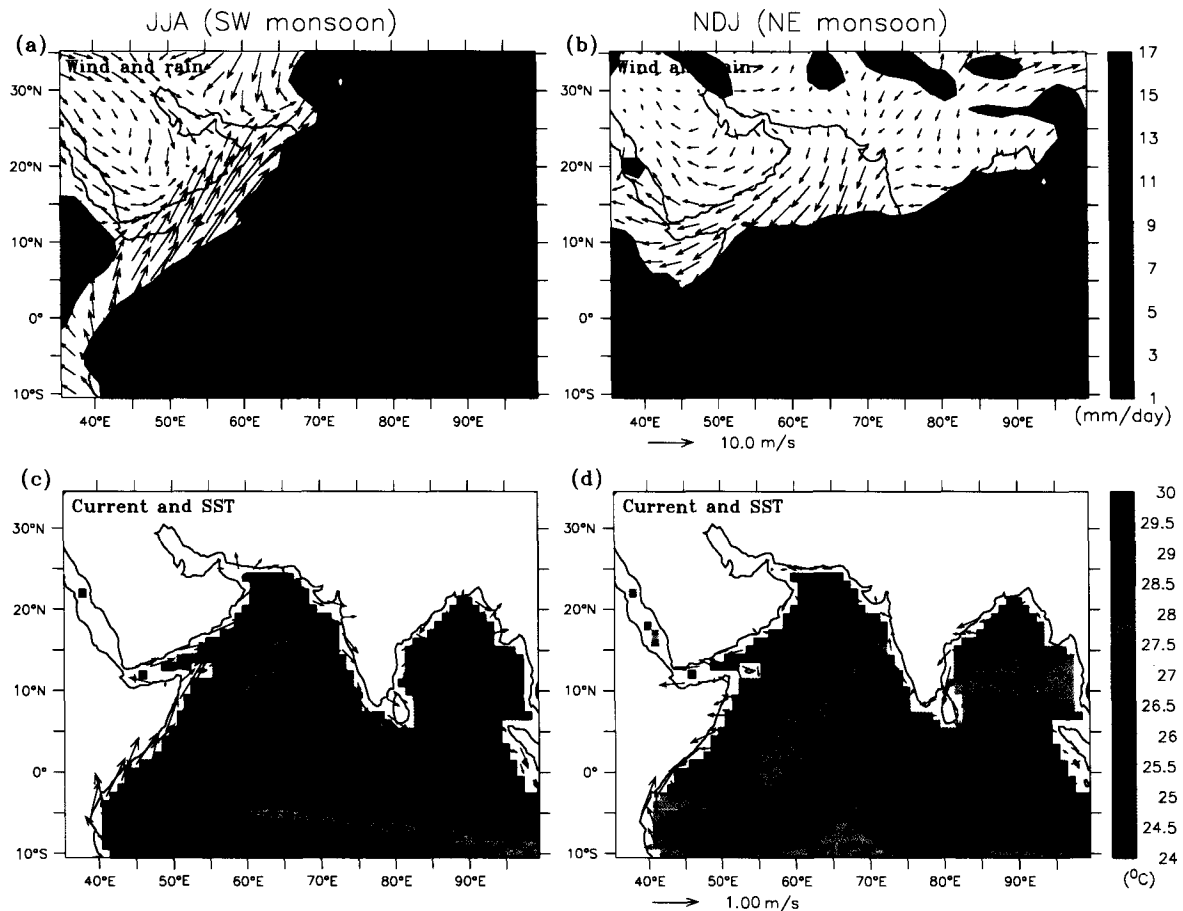
Figure 2.3: (a) Climatologies of wind-vectors and rainfall (color) over the NIO and the surrounding regions during the peak period of the SW monsoon. (b) The same as (a), but for the peak period of the NE monsoon. (c) Climatologies of surface currents (vector) and SST (color) in the NIO during the peak period of the NE monsoon. (d) The same as (c), but for the peak period of the NE monsoon season.

2.2.1   SST and the ISM

SST is an important indicator of the ocean-atmosphere coupling process. There have been numerous attempts to study the possible connections between the SST of the NIO and the ISM variability.

2.2.1.1   Genesis and onset of the summer monsoon

With the northward seasonal advance of the Sun, a progressive shift of the axis of the zone of high SST occurs, and the west-east oriented Inter-Tropical Convergence Zone (ITCZ) can be located along this zone (Choudhury and Karmarkar [41]). Hastenrath [42] showed that some of the precursor characteristics of the ISM are: (i) temperatures over land and the neighboring Arabian Sea

are spatially coherent, as is the surface pressure; and (ii) pressure over land and the wind speed over the Arabian Sea are inversely coupled.

From the climatological atlas of Hastenrath and Lamb [43], the following features can be inferred. The domain of warmest surface water moves northward from February to July with similar changes in the surface pressure patterns. In April, the highest SST is found in a broad southwest-to-northeast oriented band extending from the equatorial region of the Arabian Sea to the Bay of Bengal, this being also the domain of low surface pressure. As the domain of the warmest surface waters moves to the central Arabian Sea and Bay of Bengal, a surface pressure pattern with a meridional decrease from the south Indian Ocean to the Indian subcontinent is established. Saha ([44]& [45]) suggested that the existence of a well-defined SST anomaly between the equatorial west and east Indian Ocean could possibly explain phenomena like the equatorial westerlies, the double ITCZ, and the Somali jet (also known as Findlater jet (Findlater [1])).

A number of atmospheric phenomena over the Arabian Sea during summer might arise as feedback effects of the sea, with a complex distribution of SST, on the overlying atmosphere, and the advection of cold water from the coasts of Somalia and Arabia towards the east from June through August could play a dominant role in the interaction. The study by Rao et al. [46] on the thermal structure showed that the SST was higher in May throughout the Arabian Sea (the highest temperature of 31°C being located around 11°N , 65°E) and that there was a decrease of SST ranging from 0.5°C in the northern Arabian Sea to 3°C or more in the western Arabian Sea, and a general increase in the thickness of the mixed layer from May to June–July. The tongue of cold water resulting from the Somali upwelling in summer in the southwestern Arabian Sea extends northward and eastward, and is present throughout the central Arabian Sea between 11°N and 15°N during June-July. Rao et al. [47] studied the time variation of SST and moisture over the Arabian Sea during 25 May to 15 June 1973, covering the pre-onset and onset phases of the ISM. They reported that the onset of ISM was associated with a decrease in the SST especially north of 5°N. This was more marked upto 65°E, probably due to the northeast-ward transport of the cold water from the Somali coast and the strengthening of the low-level Findlater jet.

Studies by Nuzhdin [48] on the energetics of the atmosphere and ocean during MONEX-79, revealed the important role of the Arabian Sea surface-layer heat content in the process of summer-monsoon development. Ocean areas of pronounced heat storage can be viewed as the centres of air-sea interaction (energy-active areas), where evaporation, transfer of sensible heat to the atmosphere, and updraft of warm and moist air masses take place. Such conditions, which promote the onset of monsoon, are characteristic of the central Arabian Sea. Simultaneously,

negative anomalies of the ocean enthalpy are found in the western Arabian Sea during April–May. Therefore, the energy exchange is directed from the atmosphere to the ocean and a downdraft prevails. This contrast between the western Arabian Sea (Somali current region) and the central Arabian Sea energy-active area is one of the factors causing sharp intensification of the south-westerlies and the ITCZ migration northwards to 20°N. This contrast generally becomes critical at the beginning of June (Nuzhdin [48]). In 1979, the onset of monsoon was delayed by 10 days. A strong positive ocean enthalpy in the central Arabian Sea was observed at this time, indicating that the aforementioned contrast would have conditioned the slow-down of the process. It has been observed that lower than normal enthalpy in the central Arabian Sea as compared to the long-term normals favours the SW monsoon to set in.

Gadgil et al. [37] investigated the interaction between the large-scale convective system associated with the continental ITCZ and the ocean over which they were generated, concentrating on the relationship between organized convection and the Indian Ocean SST. They reported that on a monthly basis, the degree of cloudiness correlated well with SST for the relatively cold ocean, but when SST was maintained over 28°C, it ceased to be an important factor in determining the variability of cloudiness. Over the major regions of convection east of 70°E, which are warm year after year, the observed cloudiness could not be correlated with variations in SST.

2.2.1.2 Intensity of the summer monsoon

Jambunathan and Ramamurty [49] showed that during an active monsoon, the sea surface was warmer than the air over the Arabian Sea, and during a weak monsoon the sea surface was colder. They reported that the sea and air temperatures were lowest off the coasts of Somalia, Arabia, and Kerala, and highest over the Gulf of Aden, and north and east of Arabia during both the active and weak monsoon spells. Anjaneyulu [50] concluded that the positive anomalies of SST during May over the west and the adjoining central Arabian Sea, though small, were associated with subsequent good[1] monsoon and vice versa. He also found that in good monsoon years, the difference between the highest SST during the premonsoon and the lowest SST during the monsoon in areas off Arabia and Somalia was large and suggested that the negative anomalies of SST during August, over the western Arabian Sea and the adjoining central Arabian Sea, were associated with good monsoon and vice versa.

Joseph [51] indicated that monsoon failures during the decade 1964–1973 were followed by

---

[1]Monsoon of a region in the Indian subcontinent is good, if it receives 10% more rain fall than its climatological normal.

above normal SST over large areas of the NIO, and these anamolies persisted for one year. These failures in 1965–66, 1968-1969 and 1971–72, were associated with spells of seasonal scale of upper tropospheric westerly intrusion over South Asia. A bad^2 monsoon warms up the NIO through a decreased upwelling along the Somali and Arabian coasts, weaker surface winds over the Arabian Sea and the Bay of Bengal, reduced mixing and evaporative cooling, and reduced cloud cover (Joseph [52]; Joseph and Pillai [53]). High SST was found to cause the formation of a warm anticyclone in the upper troposphere over the Indian seas during the following winter and the pre-summer monsoon seasons. This was followed by a good monsoon which led to a cooling of the NIO. It was suggested that such a mechanism could be responsible for the three-year oscillation in the upper tropospheric wind over South Asia, the ISM rainfall over India, and the tracks of the post-monsoon cyclonic storms of the Bay of Bengal (Joseph [54]). The SST over the NIO was also found to have a three-year oscillation (Joseph and Pillai [55]). It is interesting to note that Golovastov et al. [56] reported quasi-triennial periodicity of the heat content in the upper layer of the Arabian Sea, an intensification of the Somali Current and the consequent increase in the upwelling. There are reasons to believe that tropospheric wind anomalies could be caused by SST anomalies. Joseph and Pillai [53] studied the relationship between SST and the tropospheric circulation using a Global Circulation Model (GCM) and concluded that SST anamoly over the Pacific (but not over the NIO) can drive the tropospheric circulation as observed over the NIO.

2.2.1.3 Correlation studies

A number of correlation studies were carried out to link the variability of various part of the NIO to variability of ISM. Shukla and Mishra [57] calculated the correlation coefficients between SST anomalies at about 10°N, between 60 and 70°E, and the seasonal mean rainfall over the Indian meteorological sub-divisions, and found that the correlation between SST during July and the rainfall during August over the central and western India was positive and significant. They hypothesized that cold temperatures over the Arabian Sea cause a decrease in evaporation and thus a decrease in the moisture available for downstream precipitation, leading to a rainfall deficit over India. Weare [58] concluded that a warmer Arabian Sea was weakly associated with a decreased rainfall and increased pressure over much of the Indian subcontinent. He explained that periods of higher SST, which might be expected to lead to deeper monsoon lows, were usually accompanied by periods of higher than average pressure over the sub-continent, which would tend to offset the

---

^{2}Monsoon of a region in the Indian subcontinent is bad, if it receives 10% less rain fall than its climatological normal.

effect of temperature variation. Joseph and Pillai [55] also worked out the correlations between the monsoon rainfall over India and the SST in three selected representative areas in the Arabian Sea and the Bay of Bengal. They found that the SST of the pre-monsoon months is positively correlated with the following monsoon rainfall, but the correlation was low and not statistically significant. However, the monsoon rainfall was found to be significantly negatively correlated with the post-monsoon SST. Joseph and Pillai [53] also concluded that a good monsoon produced a negative SST anomaly in the NIO.

Later, a number of correlation studies (Ramesh Kumar et al. [59] & [60]; Cadet and Diehl [61]) established a positive connection between the SST variability of different parts of the Arabian Sea and the genesis and intensity of the ISM. In general, the correlation between the summer rainfall over India and the anomaly in surface fields (pressure, wind, SST, air temperature) showed that weaker trade winds during the different months of the year, a weaker Somali jet during summer, and higher SST in the Indian Ocean were associated with weaker rainfall over India (Cadet and Diehl [61]). The weaker winds lead to less evaporation, less turbulent mixing, reduced upwelling, and, consequently, less cooling of the ocean surface (Webster [62]).

2.2.1.4 Model studies

The studies described above were mostly based on observations. There were also several model studies carried out to examine possible connection between SST of the NIO and the Monsoon. Washington et al. [63] and Druyan [64] simulated the effect of SST anomalies in the Arabian Sea on the ISM rainfall. They found that the resultant rainfall departures were not statistically significant. Washington et al. [63] showed that global-scale changes in circulation could be caused only by an anomaly of a larger spatial scale and that small spatial anomalies were able to generate only local effects. Washington [65] concluded that the experiments with two Atmospheric General Circulation Models (AGCM) suggested the existence of a local response of SST in the Arabian Sea to precipitation over the Indian sub-continent. The extent to which the Indian Ocean SST anomalies correlate with precipitation over the Indian sub-continent, however, remained to be established.

Shukla [66] pointed out that the results of some of these studies should be viewed with caution. Shukla used about 80 years data to study the correlations of SST anomaly in the NIO with the monsoon rainfall over India. He pointed out that warm (cool) SST anomaly during April, May, and June was not necessarily indicative of an above (below) average monsoon rainfall, though heavy rainfall was followed by negative SST anomalies. He further stated that the predictive value

of this relationship was rather limited because the magnitude of SST anomalies during the pre-monsoon months was within the range of observational error. Shukla also found negative bias in the SST data before the 1940s and positive bias thereafter. Shukla and Fennessy [67] carried out a GCM study in which the solar forcing of the land and ocean were incorporated separately. They showed that the annual cycle of SST in the NIO was crucially important in establishing the monsoon circulation and rainfall. Model simulations also confirmed that the Arabian Sea SST influences subsequent rainfall on time-scales less than 1 month. A cool Arabian Sea SST led to reduced Indian rainfall and vice versa (Shukla [68]; Kershaw [69]; Yang and Lau [70]).

In summary, most of studies described above tried to establish a relationship between SST of the NIO and variability of ISM. Despite contradictions between these studies, most of them agreed that the ISM is dependent on the variability of SST of the NIO, in particular of the Arabian Sea. Thus, examining the SST (ocean state) of the NIO is important for understanding the monsoonal climate over the Indian subcontinent. A number of studies were carried out in the past to understand the upper ocean thermal structure and heat budget of the Arabian Sea and of the NIO. A brief review of such studies follows.

2.2.2 Upper ocean thermal structure and heat budget

2.2.2.1 Basin–scale studies of the NIO

A number of basin-scale studies have been carried out to understand the thermal structure and heat budget of the NIO. A review of such studies is presented here. In the course of the year, the ocean gains a substantial amount of heat from the atmosphere in the northern hemisphere and the equatorial region. In contrast, the southern ocean experiences a net heat loss to the atmosphere. The annual range of the net oceanic heat gain increases with distance from the equatorial belt in both the hemispheres. Hastenrath and Lamb [43] suggested that the ocean operates as an effective heat exporter in the northern hemisphere and the equatorial belt of the Indian Ocean and the adjacent tropical seas, whereas it acts as a heat importer in the higher latitudes of the Southern Indian Ocean. They showed that the oceanic heat budgets in the Arabian Sea and Bay of Bengal exhibit greater annual variations than the other regions in the Indian Ocean because of the reversal of the monsoon systems. The net oceanic heat gain shows large positive values in the Arabian Sea and Bay of Bengal around March to April and September to October, broadly coinciding with the net radiation maxima and latent heat flux minima. The ocean loses heat to the atmosphere in these areas at the start of the summer monsoon and during winter, when enhanced evaporation accompanies reduced net radiation.

Latitudinal and annual variation of residually determined net oceanic heat gain in the Indian Ocean is presented by Hastenrath and Lamb [71]. The equatorial and northern Indian Ocean experience a sizeable heat gain, except for the more northerly region, during the northern winter, while a heat loss prevails in the south tropical Indian Ocean in the northern summer. During the northern winter, the radiative heat input at the top of the atmosphere and the precipitational heating of the atmosphere are very small for the northern Indian Ocean, and are much larger to the south of the equator (and vice versa during the northern summer).

Golovastov [72] computed the heat storage in the surface (0–100 m), sub-surface (100–400 m), and intermediate waters (400–1000 m) in the Indian Ocean using the MONEX-79 data during the SW monsoon. One of the features in the surface thermal field, brought out by the study, was high heat storage north of 2°S and low heat storage south of 2°S. During the development of the SW monsoon, the distribution of heat storage in the different layers was quite unequal. This was closely related to the peculiarities of the water-mass formation and the thickness of the surface layer. The frontal zone between the Arabian Sea and the cold waters of the south equatorial divergence was distinctly outlined in the maximum gradient of heat storage between 3° and 5°S. The ITCZ, located over 3–4°S in April–May, 1979, was associated with it. Analysis of the surface and sub-surface heat storage revealed that the late commencement of the SW monsoon and the ITCZ migration along the Somali coast from the southern to the northern hemisphere occurred mainly due to the weak development of the Somali current and the associated upwelling. It resulted in the formation of positive anomalies in heat storage in the Arabian Sea surface waters and negative anomalies in the sub-surface layer. The large-scale anomalies in turn, have been found to have considerable impact on the development of the atmospheric monsoon circulation (Golovastov [72]).

Golovastov et al. [56] also examined the formation and variability of heat content in different layers in the tropical Indian Ocean using data from 1959 to 1979. Analysis of seasonal variations in the heat content showed that the thermal field varied significantly under the effect of both outer radiative and inner dynamic factors. In several cases, values of heat content variations seem to be higher than the ocean surface heat budget, indicating that dynamic factors prevail in these regions. Analysis of the annual cycle of the heat content also reveals that variations over most of the regions are dependent on the intensity of the ocean general circulation development. A quasi-triennial periodicity in the interannual variation of the heat content is also found. During the north-east monsoon and the spring season, the variations in the surface water heat content of the monsoonal Indian Ocean are mainly dependent upon the heat budget, while during the SW monsoon and the

autumn seasons, it depends on the advective and turbulent heat exchange (Golovastov et al. [56]).

2.2.2.2 Studies focused on the Arabian Sea

The Arabian Sea is an active region of the air-sea interaction process and is recognized as an important driver of the monsoon system over the Indian subcontinent (Nuzhdin [48]). It is characterized by a pronounced summer cooling (Wyrtki et al. [74]), whereas water bodies similarly situated geographically (except the Bay of Bengal) show an increase in SST with the advance of the northern summer. The amplitude of the cooling varies from region to region. Off the coast of Somalia, it has been found to be as high as 10°C or more between May and July, while off the west coast of India, it is about 2–3°C. There exists a region of minimum cooling around 70°E, separating the regions of cooling in the eastern and western Arabian Sea. Like other tropical oceans, a major portion of the Arabian Sea undergoes winter cooling. Thus, the Arabian Sea exhibits a unique bimodal variation in the annual evolution of surface layer temperature and heat storage (Colborn [75]).

Düing and Leetma [76] computed a preliminary heat budget for the upper ocean layer in the Arabian Sea during the SW monsoon (April–August) in order to assess the importance of possible feedbacks between the ocean and the atmosphere. They suggested that the net radiation gain minus the heat loss through evaporation and sensible heat was positive in the Arabian Sea. The net heat gain at the surface is more than offset by the large south-ward heat flux across the equator and the intense upwelling off Somalia and Arabia. During the rest of the year, the heating more than balances the summer cooling. There must therefore be a mean transport of heat southward across the equator to balance the heat gain in the Arabian Sea on an yearly average (as suggested by Düing and Leetma [76]).

They also suggested various possible mechanisms such as winter cooling in the northern Arabian Sea and southward flow at intermediate depths under the Somali Current for exporting heat out of the Arabian Sea. As indicated earlier, upwelling and advection of cold water appear to be responsible for the surface cooling during summer in the northern Arabian Sea (Düing and Leetma [76]; Sastry and Ramesh Babu [77]), whereas in the eastern Arabian Sea, the entrainment of cold waters into the surface layers and the subsequent turbulent mixing play a dominant role (Sastry and Ramesh Babu [77]). Murty et al. [78] computed the total heat transfer during 15–17 June 1973 over the east-central Arabian Sea and found that the surface heat loss accounted for only about 40% of the total heat loss in the surface layer and the balance heat is lost to the ocean interior owing to mixing across the thermocline. Shenoi et al. [34] examined the role of advection

and of vertical diffusion for the Arabian Sea north of 6°N. They concluded that the net heat gain by the surface layer (upper 50 m) through the air-sea interface during the SW monsoon was offset by southward transport of heat across the equator, by heat losses through coastal pumping (upwelling off Somalia and Arabia), and through diffusion at the bottom of the surface layer.

Recently, the heat budget study by Weller et al. [3] using the high-frequency time-series data of surface meteorology and sub-surface oceanography achieved from the moored-array observations in the central Arabian Sea during October 1994 to October 1995, concluded that the SW monsoon cooling results from horizontal advection, whereas the NE monsoon cooling is due to convective entrainment driven by the net heat loss at the interface. Fischer et al. [4] later estimated the heat fluxes due to horizontal advection using the same time-series data as used by Weller et al. [3]. Their estimate shows strong warming and cooling events during the monsoons. In many cases, these events roughly match the observed temperature trend. They also estimated the vertical advective heat fluxes by balancing the surface layer budget, and then the heat-conserving vertical velocity at 125 m. They found that several strong episodic downwelling events (~ 0.02 cm s^{-1}, corresponding to ~ 18 m day^{-1}) and some smaller upwelling events are necessary to balance the heat budget.

2.2.2.3 Model studies

A number of model studies have also been carried out to examine the upper ocean thermal structure and heat budget of the Arabian Sea and of the NIO. Shetye [79] used the one-dimensional mixed-layer model of Kraus and Turner [80], as modified by Denman [81], to examine the role of various oceanic processes in the annual evolution of surface layer thermal structure of the Arabian Sea. His study was restricted to a 2° latitude zonal strip, centred at 10°N and stretching from the coast of Somalia to the SW coast of India. He concluded that the local surface fluxes alone control the surface layer thermal structure over a year except during the summer (June–August) monsoon. During the summer horizontal and vertical advections play significant roles in removing the heat gained by the mixed layer. Rao [82] used the air-sea fluxes measured during the MONSOON-77 experiment (7–21 of June 1977) in the south-central Arabian Sea at (66°E, 10.5°N) as input to the same mixed-layer model. He showed that part of the cooling was due to wind-driven convective entrainment, but suggested that some additional cooling must be due to horizontal advection (not explicitly examined in his study).

McCreary et al. [83] used a $2\frac{1}{2}$ layer thermodynamical numerical model to study the dynamics, thermodynamics, and mixed-layer physics of the Indian Ocean. They concluded that wind-driven entrainment mixing and horizontal advection are both responsible for the Arabian Sea summer

cooling. Another of their results is that the winter cooling of the northern Arabian Sea is due to the convective entrainment driven by the net heat loss at the air-sea interface.

Wacogne and Pacanowski [84], using a primitive equation model, showed that meridional circulation moves 1×10^{15}W of heat northward across the equator in the Northeast Monsoon (February) and 1.2×10^{15}W of heat southward in the Southwest Monsoon (August). Later, Loschning and Webster [85] used the same model as used by McCreary et al. [83] and drew similar conclusions as Wacogne and Pacanowski [84]: the meridional transport of heat across the equator is important for the heat budget of the Arabian Sea.

It is to quantify the process involved in the upper ocean thermal structure (heat budget) of the central Arabian Sea and to quantify the meridional transport that the mooring array of Weller et al. [2] was deployed during the US JGOFS programme. We use the data from this mooring array and a numerical model to simulate the upper ocean thermal structure at the mooring location. This allows us to quantify the processes involved and to diagnose their contributions to the heat budget in the region. We begin by describing the data and methods in the nest chapter.

Chapter 3

Data and Methods

3.1 JGOFS moored-array observations

During the US JGOFS programme, a year-long, high-frequency, concurrent time-series of the surface forcing fluxes and of the upper ocean response were measured in the central Arabian Sea at (61.5°E, 15.5°N) using an array of moorings (starting from mid-October 1994) (see Fig. 1.3). The surface fluxes include the fluxes of heat (i.e., solar short-wave radiation, net long-wave radiation, turbulent latent and sensible heat fluxes), momentum (wind stress), and fresh water (evaporation and precipitation rates). The data of oceanic response include temperature, salinity, horizontal current, and chlorophyll-concentration profiles. All these data were measured over one year with a 7.5 minute resolution (with 2 day-gap during 20–21 April 1995). This time-series data set has been used extensively in this study. In particular, the time-series provides a unique opportunity to force a numerical model with an accurate estimate of local air-sea fluxes.

3.1.1 Air-sea fluxes

These data were published by Weller et al. [2] and are shown in Figs. 3.1 and 3.2. These fluxes are dominated by the monsoonal cycle. During the NE monsoon, when the wind is moderate, the ocean loses on average 20 W m^{-2} to the atmosphere owing to high evaporation and reduced solar radiation. During the SW Monsoon, strong winds prevail, but the ocean gains an average of 90 W m^{-2} through its surface owing to reduced losses through long-wave radiation and evaporation. The net heat gain at the surface during the beginning of this period (June and July) is significantly less than the average value (approximately half). This is due to the reduction of the solar input in response to the increase in cloud cover and latent heat flux. During the inter monsoons (IMs), the winds are weak and the ocean gains on average 100 W m^{-2} through its surface owing to the

25

increase in solar radiation and decrease in latent heat flux. Except during the NE monsoon, the ocean gains heat at its surface. The net flux over the studied year is $+2.01 \times 10^9$ J m^{-2}. The fresh-water flux is mostly dominated by evaporation throughout the year. According to Weller et al. [3], the nature of these surface fluxes is mostly similar to the climatological features.
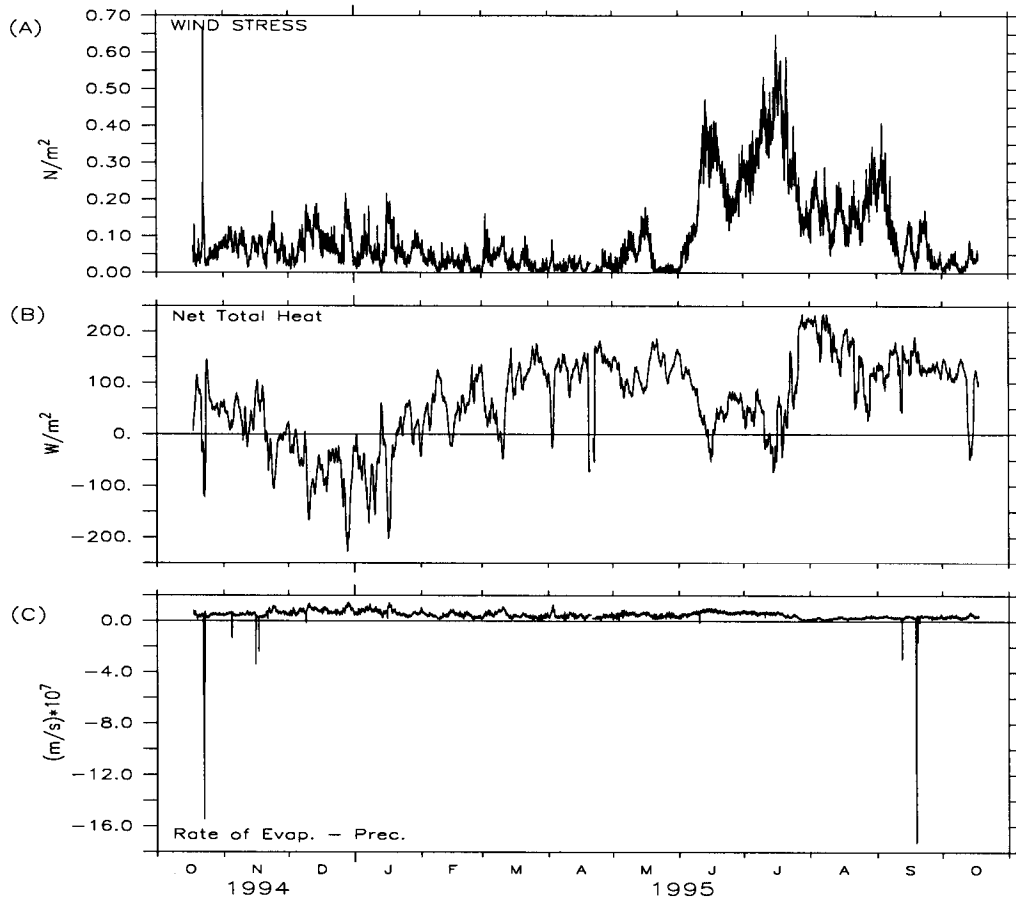
Figure 3.1: Observed wind stress, net heat flux, and fresh water flux (evaporation minus precipitation) at the ocean surface estimated from the meteorological measurements at the central mooring. All data are daily averages. The heat fluxes are positive towards the ocean and are negative away from it.
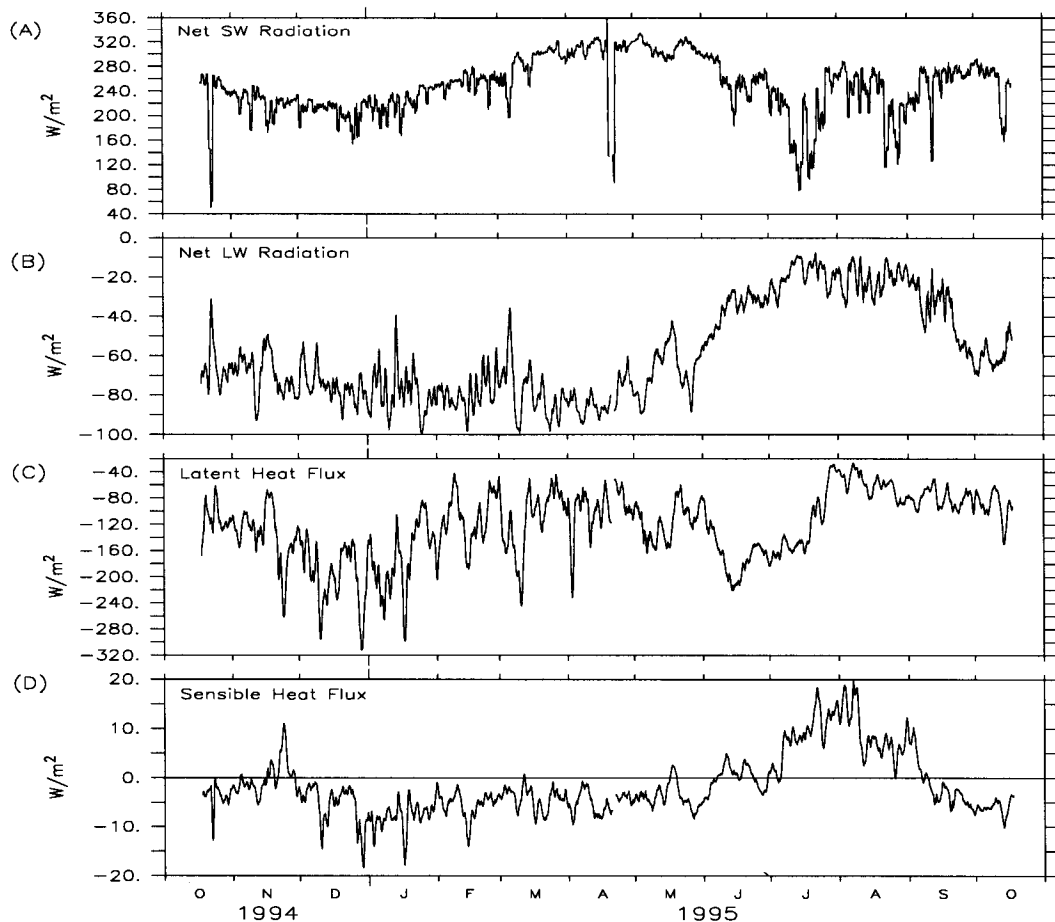
Figure 3.2: (A) Net short-wave, (B) net long-wave, (C) turbulent fluxes of latent heat, and (D) turbulent fluxes of sensible heat. observed at the moored array. The sum of these fluxes is presented in Figure 3.1B. All data are daily averages.

3.1.2 Thermal structure

The time-series of upper ocean (0–250 m) temperature in the central Arabian Sea 61.5°E, 15.5°N) from October 1994 to October 1995 (Weller et al. [3]) is presented in Fig. 3.3a-b. For the purpose of comparison with the model prediction in the next chapter, the main features in the observed temperature are briefly recalled here. The near surface layer (0–50 m) exhibits a biannual cycle associated with the monsoons. During the NE monsoon (November 1994 to January 1995), the SST decreases from 28.3°C to 24.9°C. During the following Spring Inter Monsoon (IM), it increases by 6.4°C up to a maximum of 31°C at the end of May, and then drops by 5.5°C during the SW monsoon to 24.5°C in mid-August. The annual cycle ends with a warming during the Autumn IM. The evolution of the mixed layer depth (MLD), defined here as the depth at which temperature is 0.1°C less than SST; this definition was also used by Weller et al. [3] and Fischer et al. [4]. The

mixed layer (ML) is very shallow (less than 20 m) at the beginning of the study period and reaches 100 m at the end of the NE monsoon. This deepening, however, is not continuous, with a marked meso-scale feature occurring in November and then in late January (with a time-scale of a few days). In February, the ML quickly shoals back to less than 20 m and remains shallow until the beginning of the SW monsoon, when it deepens again to 75 m at the end of July. Apart from a meso-scale variation at the end of August, the ML shoals during the next inter-monsoon. Regarding the sub-surface layer, the thermocline (defined here as the depth of 22°C isotherm) varies like the ML until the end of December 1994, then remains flat and deep (around 120 m) thereafter until mid-July 1995, when it undergoes a steep shoaling to fluctuate around 80 m until the end of the study period. The annual mean temperature of the ML is 27.21°C and it is 21.03°C for the 0–250 m layer.

When looking at the trend in observed temperature (see Fig. 3.3c), it appears that the fastest and strongest cooling and warming events occurred below the mixed layer in November and December (beginning of the NE monsoon) and again in late July (after the peak of the SW monsoon). These events corresponded also to the strongest currents (Fischer et al. [4]) and the largest excursions of the thermocline.

A comparison with the Levitus [29] temperature climatology (see Fig. 3.4a-c) shows that the 1994–1995 time-series is characterized by a strong cooling (3–4°C) in the sub-surface layers during the early NE monsoon and during the late SW monsoon (August). During the rest of the year, the sub-surface temperature does not differ significantly (1–2°C) from the climatology. Regarding the near surface layer, the difference never exceeds 1°C throughout the year. The difference between the MLD during 1994–1995 and the climatological MLD is less than 10 m, except during NE monsoon, when the 1994–1995 MLD is deeper (~50 m) than the climatology (Fig. 3.4b). As regards the temperature trend, the near surface layer (upper 50 m) trends are mostly similar, but the 1994–1995 data exhibit larger and intense variability in the sub-surface layers (Fig. 3.4d). sub-surface warming trends during December and sub-surface cooling trends during July–August of the time-series are more intense (3 times) than in the climatology. The early NE monsoon (November) sub-surface cooling trend of 1994–1995 time-series is not present in the climatological data.
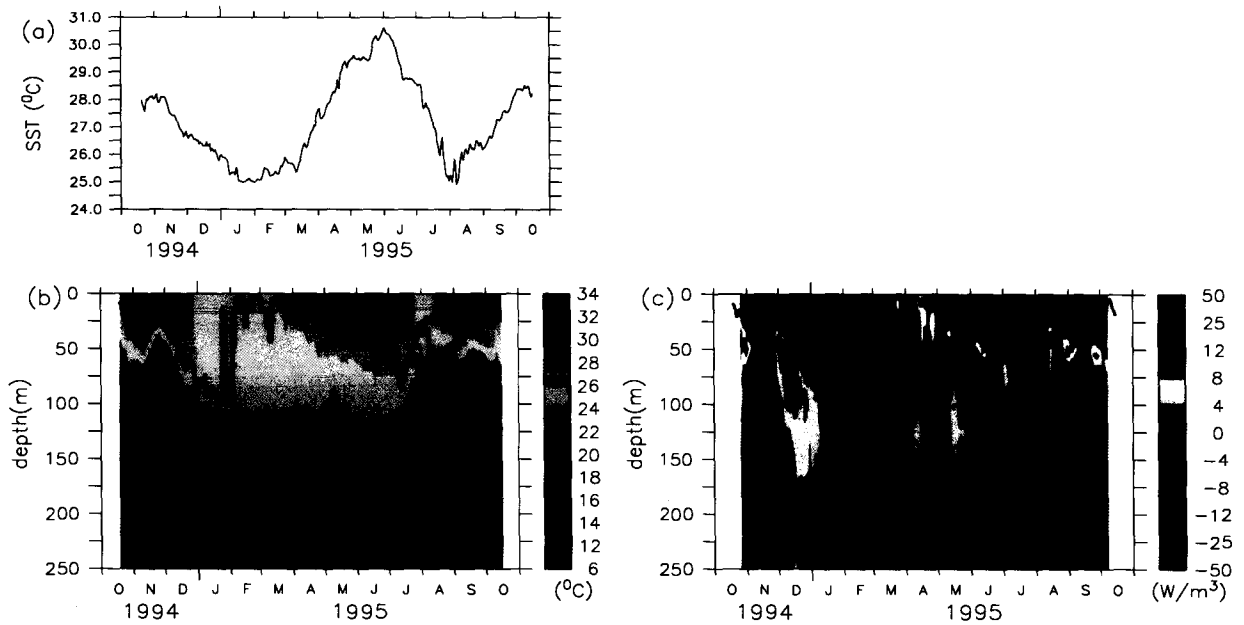
Figure 3.3: A high-frequency, year-long (October 1994 to October 1995) time-series JGOFS moored-array observations of upper ocean thermal structure in the central Arabian sea at (61.5°E, 15.5°N): (a) sea surface temperature (SST) evolution; (b) temperature profile evolution over 0–250 m depths and the daily mean mixed layer depth (MLD) (blue line); (c) evolution of the temperature trend (in heat units, W m^{-3}; low pass filtered with a 10-day running mean) and the daily mean mixed-layer depth (blue line).
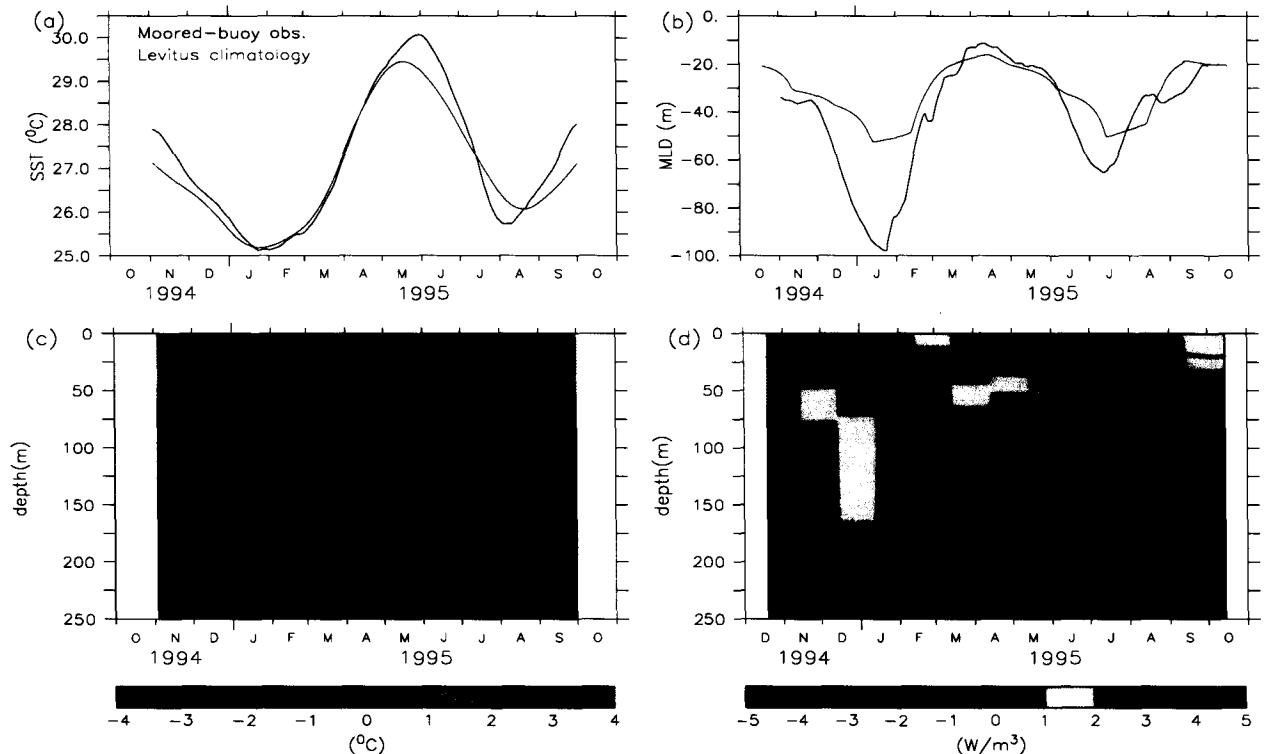
Figure 3.4: JGOFS year-long time series of upper ocean thermal structures compares with the Levitus [29] climatology: (a) comparison between SSTs, (b) comparison between MLDs, (c) Difference between the 1994–1995 temperature profiles and temperature climatology, (d) evolution of the trend of temperature climatology (in heat units, W m^{-3}) and climatological mixed-layer depth (blue line)

3.1.3 Horizontal current

The horizontal currents were measured on the central mooring at following depths: 5, 10, 15, 25, 35, 45, 55, 65, 80, 301.2, 492, and 749.5 m (Weller et al. [3], their Fig. 7). These values linearly interpolated for 5, 50, 100, and 200 m are presented in Fig. 3.5. The currents are very strong (almost ~80 cm s^{-1}) during the first part of the NE monsoon and during the SW monsoon and weak during rest of the year. In October and November 1994 and during the SW monsoon, the currents are southeast-ward; during December and January, the currents are northwest-ward. The currents decrease with increasing depth, but they are still significant at 200 m depth during the monsoons. According to Weller et al. [3] and Fischer et al. [4], the observed currents in 1994–1995 differed considerably from their climatological average in the region during the first part of the NE monsoon (October–December 1994) and during the second part of the SW monsoon

(late July to early September 1995). The strongest velocity signal in the upper ocean during both these periods was the flow associated with a meso-scale geostrophic structure that passed slowly through the observation area (Weller et al. [3], Fischer et al. [4]).
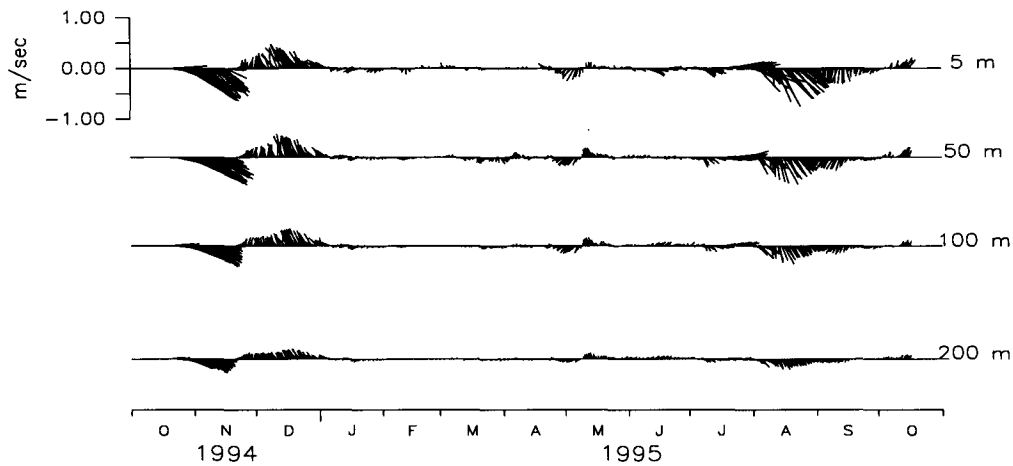
Figure 3.5: Year-long time-series of daily averaged observed horizontal velocity at (61.5°E, 15.5°N) in the central Arabian sea. Flow to the north is upward.

3.1.4 Salinity

The salinity data were measured on the central mooring and published by Weller et al. [3]. The observed salinity structure for the upper 100 m exhibits an annual cycle (see Fig. 3.6). From the beginning of the time-series (mid-October 1994) to the end of Spring IM (end of May 1995) the surface salinity increases from 35.6 psu up to a maximum of 36.7 psu; then it decreases up to 35.5 psu at the end of the studied period (mid-October 1995). As regards the sub-surface layers (below the ML), strong synoptic variability is exhibited between the MLD and the 200 m depth during the NE monsoon (fresh incursions).
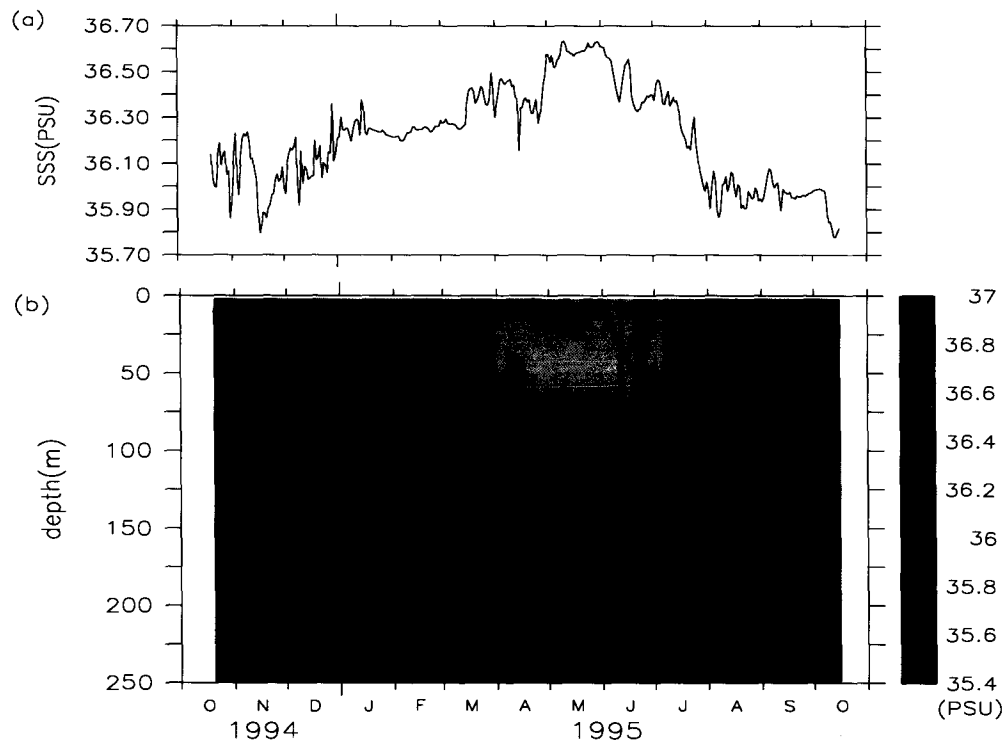
Figure 3.6: Year-long time series of daily averaged sea surface salinity (a), and vertical profiles of salinity (b), measured at the central mooring in the Arabian sea (Weller et al. [3]). The black line corresponds to the MLD.

3.1.5 Chlorophyll

The phytoplankton chlorophyll concentration profile during October 1994 to October 1995 was measured at the moored buoy location in the central Arabian Sea (Sigurdson et al. [86] & [87]) together with physical and meteorological data. The measurement was made at four depths (10, 35, 65, and 80 m) with fluorometers mounted on a mooring line. These measurements were suspected for biofouling, and were corrected using the data obtained from associated cruises under the US JGOFS programme (Dickey et al. [88]). The data are presented in Fig. 3.7. The chlorophyll (concentration) exhibits a very strong monsoonal cycle. Strong chlorophyll concentration (bloom) was observed during December–January (NE monsoon) (2 mg m^{-3}) and July–August (SW monsoon) (1 mg m^{-3}) at the surface. During the rest of the year, the surface chlorophyll concentration is less than 0.3 mg m^{-3}. The concentration decreases with depth. The data were used to examine the biological heating impact on the upper ocean thermal structure in the central Arabian Sea (in the auxiliary experiment in Appendix B.2).

Chlorophyll Concentration (mg/m³)
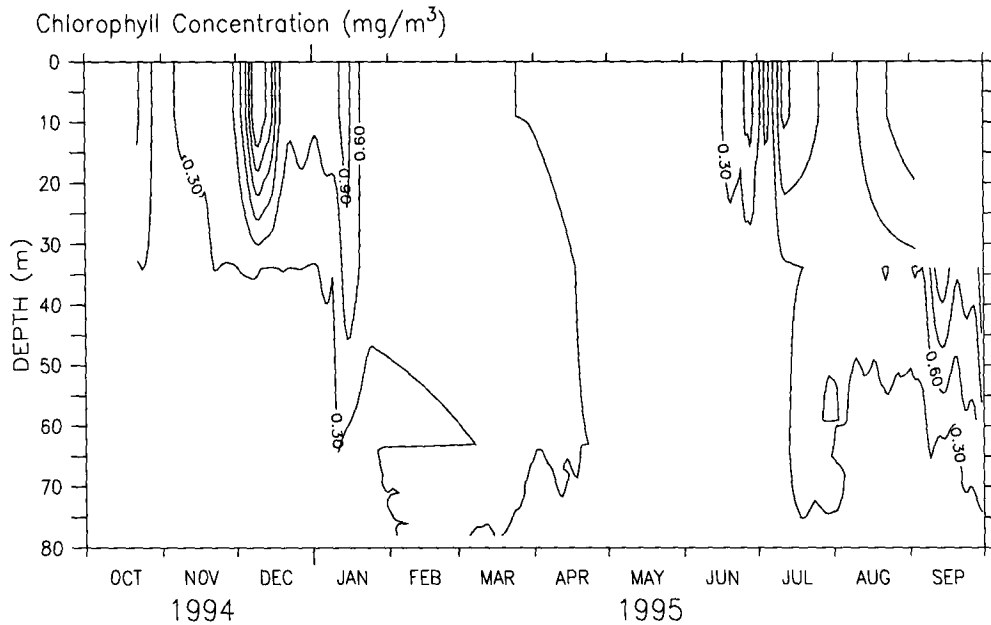
Figure 3.7: Vertical profile of observed Chlorophyll concentration measured at the central mooring location (Dickey et al. [88]).

3.2 Methods

As described in the introduction (chapter 1) the main aim of the thesis is to simulate the upper-ocean thermal structure in the central Arabian Sea in order to analyse the heat budget and to perform process sensitivity experiments. A 1D-vertical mixed layer model is forced with atmospheric fluxes and advection. Atmospheric forcing fluxes available from the *in situ* measurements (Weller et al. [2]). Horizontal advection estimates are available from Fischer et al. [4], but, as we shall show in section 3.2.5 we had to achieve an independent re-estimate. Estimation of vertical velocity requires data of vertical velocity only as the model can predicts the vertical gradient of temperature. The vertical velocity, as in all oceanography problem, poses a challenge. This leads to two possible approaches. First, we can estimate the vertical velocity by some means (for example, by attempting to close the heat budget, as done by Fischer et al. [4]), and use the estimated vertical velocity to predict the temperature profile, which can be compared with the observation. This is illustrated schematically in Fig. 3.8. The technique used to compute advection for this approach are described in sections 3.10, 3.2.5 and 3.2.6. Second, we can use the observed temperature profile to constrain the model and thereby estimate a resultant vertical velocity. This is illustrated schematically in Fig. 3.9. The technique used to compute vertical advection using this approach is described in section 3.2.6.2.
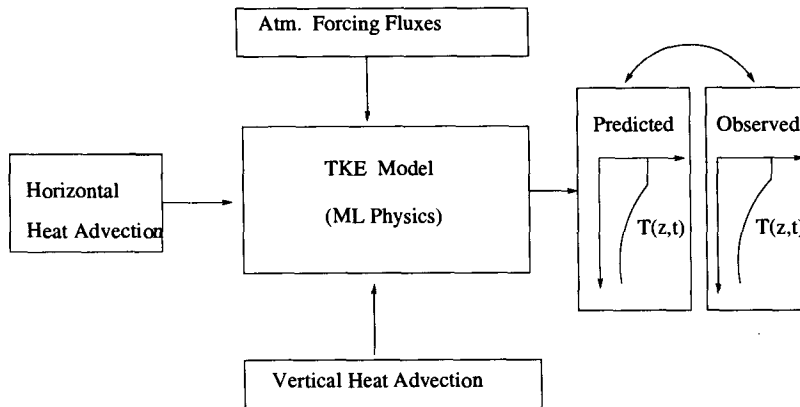
Figure 3.8: Schematic showing an approach of implementing the model to predict the temperature profile.
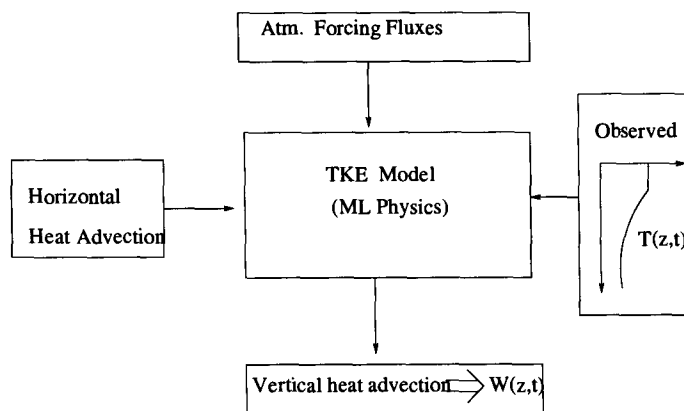
Figure 3.9: Schematic showing an approach of implementing the model to predict the vertical velocity.

3.2.1 Model

A mixed-layer thermo-dynamical model of the upper ocean, the main tool of this study, is described here. The most generally used mixed-layer models are of two classes: Bulk (or integrated) Models and Turbulent Closure (or differential) Models. The bulk models are simple and computationally efficient. They assume the existence of a completely well-mixed layer with negligible vertical gradient (Kraus and Turner [80]; Denman and Miyake [81]; Price et al. [89]). The main drawbacks of these bulk models are: (i) the physical (and biological) properties are usually discontinuous across the base of the mixed layer and a subsequent algorithm has to be used to smooth the gradients, employing either a gradient Richardson number, as in Price et al. [89], or a vertical diffusion coefficient based on property gradients, as in Gaspar [90]; (ii) due to their bulk nature, the vertical structure of turbulence in the mixed layer cannot be known; and (iii) nothing can be known below the mixed layer. In contrast, the turbulent closure models are more realistic, sophis-

ticated, and provide better results for the entire water column at a fine resolution. These models are more difficult to understand in an intuitive way than the bulk models. Insight can be gained by comparing their behavior with that of the bulk models. The great advantage of using such models is that the same turbulent parameterization scheme can be used for the entire water column from the ocean surface to the abyss. Turbulent closure models are further classified into two groups based on closure schemes: (i) the 2.5-level Mellor and Yamada (MY) closure scheme (Mellor and Yamada [91]), and (ii) the one-equation Bougeault and Lacarrère (BL) closure scheme (Bougeault and Lacarrère [92]). The BL closure scheme is much simpler than the MY closure scheme. The specified turbulent length scales used in the BL closure scheme are simple and physically appealing (Gaspar et al. [93]). On the contrary, the prognostic equation for the master length scale requires complicated MY closure assumptions in which one can not assert great confidence (Mellor and Yamada [94]).

Previous work on the simulation of the diurnal temperature cycle within the scope of the Long-Term Upper Ocean Study (LOTUS) in the Sargasso Sea and the seasonal cycle of temperature off the Iberian coast, showed that two different models based on the BL closure scheme (Gaspar et al. [93]) and on the quasi-equilibrium version of the MY closure scheme (Galperin et al. [95]), respectively, produce similar results. Subsequent studies in the NW Mediterranean (Levy et al. [96]), and in the Austral ocean (Pondaven et al. [97]) proved that the turbulent kinetic energy (TKE) model of upper ocean (Gaspar et al. [93]) based on the BL closure scheme is able to simulate properly the upper ocean processes in various situations. It is also worth noting that the implementation of the BL closure scheme in the OPA (Ocean Parallelized) GCM (General Circulation Model) significantly improved the mixed-layer physics and the thermocline structure of the Equatorial Atlantic Ocean (Blanke and Delecluse [98]). Hence, we use the TKE model of Gaspar et al. [93] to simulate the upper ocean mixed-layer processes in the central Arabian Sea.

3.2.1.1 Assumptions

The governing equations (in section 3.2.1.2) of the TKE model (Gaspar et al. [93]) relies on the following assumptions:

1. Incompressibility: This approximation is valid when the time changes of parcel's density (ρ) are very small relative to the density, i.e. $\frac{1}{\rho}\frac{d\rho}{dt} \approx 0 = \vec{\nabla}.\vec{U}$. Hence the continuity equation $\frac{1}{\rho}\frac{d\rho}{dt} + \vec{\nabla}.\vec{U} = 0$ is now reduced to $\vec{\nabla}.\vec{U} = 0$, where $\vec{\nabla}$ is the gradient (vector) operator, and $\vec{U} = (U, V, W)$ is mean velocity (vector).

2. Hydrostatic approximation: Pressure is the force per unit area acting on a fluid parcel. Pressure at a point within a fluid at rest in a gravitational field is given by the weight of fluid above the point per unit horizontal cross sectional area. Hence, the vertical pressure gradient is equivalent to buoyancy. This situation constitutes the hydrostatic balance. Mathematically, the condition for hydrostatic balance can be written as $\frac{dP}{dz} = -\rho g$, where P is the pressure at any level, ρ the density, and g the accelation due to gravity. When the fluid is in motion, vertical pressure gradients are also affected by vertical acceleration and friction. However, for many geophysically relevant fluid motions, the dominant balance in the vertical momentum equation remains the hydrostatic balance. The level to which the hydrostatic balance remains dominant is directly proportional to the ratio of vertical (H) to horizontal (L) length scales of motion.

3. Boussinesq approximation: The variations of fluid density are neglected insofar as they influence the inertia; variation in the weight (or buoyancy) of the fluid may not be neglected.

4. The ocean is assumed to be horizontally homogeneous: Turbulent transfer of matter and energy is effected almost entirely by fluctuating vertical velocity.

5. Turbulent closure hypothesis (also known as K-theory): It is assumed that small-scale horizontal and vertical transports can be evaluated in terms of diffusion coefficients and derivatives of the large-scale flow. As for example turbulent variation of heat flux along vertical direction can be expressed as, $-\overline{W'T'} = K_h \frac{\partial T}{\partial z}$, where W' and T' are turbulent fluctuations of vertical velocity and temperature respectively, T is the mean temperature of the water parcel, and K_h is a constant known as eddy diffusivity of heat. The overbar on the left hand side represents the ensemble average of the turbulent fluctuation of that quantity.

6. Stable stratified layers: The water column is adjusted at each time step to satisfy both static and dynamic stability criteria.

   (a) Convective adjustment (static stability): Convective adjustment occurs when density profile becomes gravitationally unstable, i.e. heavy water overlying lighter water. If the density profile is found to be unstable, then heat is assumed to be mixed vigorously between levels so that total heat is conserved and the local vertical gradient is at heat neutrally buoyant, i.e. $\frac{\partial \rho}{\partial z} \geq 0$,

   (b) Shear flow adjustment (dynamic stability): Vertical mixing in the ocean is dominated by the influence of the density gradients that limit vertical motions. The dynamic effect

of density gradient is contained in the parameter $N = \left(-\dfrac{g}{\rho_0}\dfrac{\partial\rho}{\partial z}\right)^{1/2}$, the Brunt-Väisäla (buoyancy) frequency, which is the frequency with which a displaced element of fluid will oscillate. The corresponding periods $2\pi/N$ are typically a few minutes in the thermocline, and up to many hours in the weakly stratified deep ocean.

In a shear flow, the kinetic energy associated with the vertical gradient of horizontal velocity $\partial U/\partial z$ has a destabilizing effect, and the dimensionless ratio $R_g = N^2/\left(\dfrac{\partial U}{\partial z}\right)^2 = \dfrac{-g\partial\rho/\partial z}{\rho_0\left(\partial U/\partial z\right)^2}$ called the *gradient Richardson number,* gives a measure of the relative importance of the stabilizing buoyancy and destabilizing shear.

Of more direct physical significance is the *Flux Richardson number,* R_f, defined as the ratio of the rate of removal of energy by buoyancy forces to its production by shear. It can expressed as $R_f = \dfrac{g\overline{\rho'w'}}{\rho_0\overline{U'W'}(\partial U/\partial z)} = \dfrac{K_\rho}{K_m}R_g$, where K_ρ and K_m are eddy diffusivities of buoyancy and momentum respectively.

Dynamic stability is imposed in the present model by ensuring that the value of the flux Richardson number R_f is always greater than or equal to 0. 23.

7. Wave-like dynamical effects such as gravitational, inertial, and Rossby waves are ignored.

3.2.1.2 Governing equations

Under the above approximations, the unidimensional forms of the balance equations for temperature, salt, and momentum (after the Reynolds decomposition for turbulent fluid flow) are:

$$\frac{\partial T}{\partial t} = \frac{F_{sol}}{\rho_0 C_p}\frac{\partial I}{\partial z} + \frac{\partial \overline{T'W'}}{\partial z}, \tag{3.1}$$

$$\frac{\partial S}{\partial t} = \frac{\partial \overline{S'W'}}{\partial z}, \tag{3.2}$$

$$\frac{\partial U_H}{\partial t} = -fk \times \overline{U}_H - \frac{\partial \overline{U_H'W'}}{\partial z}, \tag{3.3}$$

where T, S, U_H, and W are the mean temperature, salinity, horizontal velocity, and vertical velocity of the water column respectively. Mean quantities are denoted as $\overline{X}$ and X' denotes fluctuations around the mean. ρ_0 and C_p are the reference density and specific heat of seawater,

respectively. F_{sol} is the solar irradiance absorbed at the sea surface and $I(z)$ is the fraction of F_{sol} that penetrates to depth z; f is the coriolis parameter and k the vertical unit vector; z is positive upward.

3.2.1.3 Surface boundary conditions

The turbulent fluxes of heat must balance the sum of latent, sensible, and long-wave radiative heat fluxes. Similarly, the turbulent salt fluxes at the surface must balance the fresh-water fluxes (evaporation and precipitation), and the turbulent momentum fluxes must balance the momentum fluxes provided by the wind stress term.

$$-\rho_0 C_p \overline{T'w'}(0) = F_{nsol} = H + LE + F_{ir}, \tag{3.4}$$

$$-\rho_0 \overline{S'w'}(0) = E - P, \tag{3.5}$$

$$-\rho_0 \overline{U'_H w'}(0) = \tau, \tag{3.6}$$

where F_{nsol} stands for the sum of surface latent heat (LE), sensible heat fluxes (H), and long-wave radiation (F_{ir}). E and P are the evaporation and the precipitation rates, respectively, and τ is the surface wind stress. Heat fluxes are positive downwards (opposite to z and W).

3.2.1.4 Turbulent closure model

The vertical turbulent fluxes are parameterized using the classical concept of eddy diffusivity:

$$-\overline{T'W'} = K_h \frac{\partial \overline{T}}{\partial z}, \tag{3.7}$$

$$-\overline{S'W'} = K_s \frac{\partial \overline{S}}{\partial z}, \tag{3.8}$$

$$-\overline{U'_H W'} = K_m \frac{\partial \overline{U}_H}{\partial z}. \tag{3.9}$$

Viscosity and diffusivities are related with length and velocity scales according to:

$$K_m = c_k l_k \overline{e}^{1/2}, \qquad K_s = K_h = K_m/P_{rt}, \tag{3.10}$$

where c_k is a constant, l_k is the mixing length, and e is the turbulent kinetic energy (TKE) defined by $e = 0.5(U'^2_H + W'^2)$. P_{rt} is the turbulent Prandtl number, assumed to be 1 (this choice

is supported by some laboratory experiments and oceanic observations (Mellor and Yamada [94]; Gregg et al. [99]))

To close the system, TKE is determined from the balance equation

$$\frac{\partial e}{\partial t} = -\underbrace{\frac{\partial}{\partial z}\left(\overline{e'W'} + \frac{\overline{p'W'}}{\rho_0}\right)}_{transport\,along\,z} - \underbrace{\overline{U'_H W'}\frac{\partial \overline{U}_H}{\partial z}}_{production\,due\,to\,wind\,shear} + \underbrace{\overline{b'W'}}_{production\,due\,to\,buoyancy} - \underbrace{\varepsilon}_{viscous\,dissipation}$$

$$(3.11)$$

where p is the pressure, ε the dissipation rate of TKE, and b the buoyancy defined as $b = g[(\rho_0 - \rho)/\rho_0]$; g is the acceleration due to gravity, and ρ is the density of sea water (computed from the UNESCO formulation; see Appendix A).

The concept of eddy diffusivity is used again to parameterize the vertical flux of buoyancy and of TKE:

$$-\overline{b'W'} = K_\rho\frac{\partial \overline{b}}{\partial z}, \tag{3.12}$$

$$-(\overline{e'W'} + \frac{\overline{p'W'}}{\rho_0}) = K_e\frac{\partial \overline{e}}{\partial z}. \tag{3.13}$$

For the diffusivity of density we have $K = K_m/P_{rt}$, and with the usual assumption $K_e = K_m$. The dissipation rate is parameterized as $\varepsilon = c_\varepsilon \overline{e}^{3/2}/l_\varepsilon$, c_ε is a constant and l_ε the length scale for dissipation.

3.2.1.5 Length scales

The major difficulties of the model are in parameterizing the turbulent viscosity based on velocity and length scales and the determination of such scales, especially the length scale. In this model, very simple definition of the length scales are used, avoiding a large number of coefficients. This choice has proved to be reasonable (Bougeault and Lacarrére [92]; Gaspar et al. [93]). The mixing length definitions are

$$l_\varepsilon = (l_u l_d)^{1/2}, \tag{3.14}$$

$$l_k = \min\left(l_u l_d\right), \tag{3.15}$$

where l_k and l_ε being the length scales for mixing and dissipation, respectively, and l_u (mixing

length upward) and l_d (mixing length downward) are computed according to Bougeault and André [100].

$$\frac{g}{\rho_0} \int_z^{z+l_u} [\rho(z) - \rho(z')]dz' = e(z);$$ (3.16)

$$\frac{g}{\rho_0} \int_z^{z-l_d} [\rho(z) - \rho(z')]dz' = e(z).$$ (3.17)

The values of $z + l_u$ and $z - l_d$ are naturally limited by the ocean surface and bottom. This formula for primary scales allow for a stratified ocean. For a stratified fluid with constant density gradient, the primary scales are

$$l_u = l_d = 2^{1/2} l_b,$$ (3.18)

where l_b is the usual buoyancy length scale; $l_b = e^{1/2}/N$, where N is the Brunt-Väisälä frequency (defined earlier in section 3.2.1.1). For the simple case of a homogeneous ML with a strong density jump at its base, l_u and l_d are the distances from the particle to the surface and to the base of the ML, respectively.

3.2.1.6 Parameterization of solar irradiance

In reality the solar irradiance within the ocean is a complex function of phytoplankton (chlorophyll) concentration, wavelength, and depth (see Appendix C). For general applications, the absorption-law of solar irradiance $I(z)$ can be parameterized according to the following double exponential function (Paulson and Simpson [101]):

$$I(z) = R \exp\left(\frac{z}{\xi_1}\right) + (1 - R) \exp\left(\frac{z}{\xi_2}\right)$$ (3.19)

Here, subscripts 1 and 2 refer to the red and blue penetrating solar light and z is depth (positive upward). In the above equation, R is dimensionless parameter, and ξ_1, and ξ_2 are attenuation coefficients. ξ_2 is dependent on phytoplankton concentration (biomass). In the absence of biomass profile, sensitivity experiments can be carried out against various water types as proposed by Jerlov [102] to select the constant parameters. The values of constant parameters used in above equation for the various water types of Jerlov are presented in a Table 3.1. The classification of water type of the world oceans is based on optical characteristics (turbidity).

Table 3.1: Different water type based on Jerlov [102]. Water type ranges from clear to increasing turbid water.

Type	R	ξ_1 (m) (red)	ξ_2(m) (blue)
I	0.58	0.35	23
IA	0.62	0.60	20
IB	0.67	1.0	17
II	0.77	1.5	14
III	0.78	1.4	7.9

3.2.1.7 Condition of diffusion below the mixed layer

To avoid unrealistically small diffusion and dissipation rates within the pycnocline, Gaspar et al. [93] assumed a minimal value for TKE (e_{min}). Empirically e_{min} is set to 10^{-6}m^2 s^{-2}. Gaspar et al. [93] suggested that better results could probably be obtained by a e_{min} parameterization that accounts for internal wave activity and surface forcing. In the present study e_{min} is assumed to be constant and equal to 10^{-6}m^2 s^{-2}.

3.2.2 Application of the model

3.2.2.1 Inclusion of advective terms

The governing equations of the model do not include the effect of vertical advection and horizontal advection. As it is known that horizontal and vertical advections play an important role in the upper ocean thermal structure of the Arabian Sea, their influences have to be incorporated in the temperature equation. This is done by adding temperature advective terms in Eq. 3.1 (heat balance).

$$\frac{\partial T}{\partial t} = \frac{F_{sol}}{\rho_0 C_p}\frac{\partial I}{\partial z} + \frac{\partial \overline{T'W'}}{\partial z} - \underbrace{U_H \cdot \nabla_H T}_{hor\ advection} - \underbrace{W\frac{\partial T}{\partial z}}_{ver\ advection} \tag{3.20}$$

3.2.2.2 Numerical implementation

The model equations are discretized with a second-order finite difference scheme on a staggered grid i.e., T, S, and U_H are computed at the center of each grid cell and the turbulent fluxes and TKE are estimated at the cell boundaries. The temporal scheme is a leapfrog scheme. Vertical diffusion and vertical advection terms at the bottom-most layer of the ocean model (at 250 m)

are estimated using an implicit backward scheme. The model is initialized with observed vertical profiles of T, S, and U_H. The TKE (e) profile is initialized as follows: $e = 10^{-4} \text{m}^2 \text{ s}^{-2}$ within the mixed layer (ML) and $e = e_{min}$ below. The simulation is performed using a uniform vertical resolution of 1 m from surface down to 250 m. The time step is 90 s; a year-long numerical integration is carried out at the moored-buoy time-series observations starting from 20 October 1994.

The forcing fluxes at the surface are solar radiation, long-wave radiation, and turbulent fluxes of heat, momentum, and freshwater. All these fluxes were estimated by Weller et al. [2] from the surface meteorological measurements on the buoy moored at the study location (see section 3.1.1 for a description). As these estimates are not available for the break period of 2 days (i.e., 20–21 April 1995), the values for these two days were obtained from the nearest neighbour points. The temporal resolution of the surface forcing fluxes is 7.5 minutes; the fluxes are linearly interpolated on the model grid. The contribution of the horizontal advection and vertical advection to the temperature structure has to be determined from external data source and will be prescribed in the model at every time step. Two kinds of advective heat fluxes have been considered here: one is based on Fischer et al. [4] and another is based on the present study estimates (see sections 3.2.3 and 3.2.6.2). The reason to considering two kinds of estimates has already been described in the beginning of this section (Figs. 3.8 & 3.9). The temporal and spatial resolution of the advective heat fluxes are larger than the model resolution, so the fluxes are interpolated to the model resolution and prescribed into the model.

3.2.2.3   Choices of the model parameters

A number of parameters are involved in the model. The values assigned are presented in Table 3.2. The values of all the parameters are based on the published literature except for the three parameters R, ξ_1, and ξ_2 used in the computation of solar irradiance $I(z)$ at depth z. Model sensitivity experiments are carried out against the various water types proposed by Jerlov [102] in the present study to fix these parameters. It is found that type I (open ocean) water is the most appropriate for the region (central Arabian Sea).

3.2.3   Fischer-based estimates of horizontal heat advection

Fischer et al. [4] estimated horizontal advective heat fluxes at the study location for the upper 125 m using the observed horizontal currents and the horizontal temperature gradient estimated from 1994–1995 moored-buoy time-series observations (see Fig. 1.3). The temporal resolution of the

Table 3.2: The constant parameters and the assigned values used in the model are listed here.

Parameters	Values	Units		Parameters	Values	units
ρ_0	1025	kg m^{-3}		ξ_2	23	m
S_0	35.5	psu		C_k	0.1	
T_0	26	^{0}C		C_ε	0.7	
C_p	4000	J kg^{-1} /^{0}C		e_{min}	1.0×10^{-4}	m^2 s^{-2}
R	0.58			P_{rt}	1	
ξ_1	0.38	m				

estimate is four hours and the spatial resolution is 5 m. An advective forcing field $A(z)$ for the entire domain of simulation 250 m depth is derived from the Fischer et al. [4] estimates (A_F) as follows:

$$A(z) = \begin{cases} A_F & \text{for} \quad z \leq 125\,\text{m} \\ A_{F,z=125} \times \frac{U_z}{U_{z=125}} & \text{for} \quad z > 125\,\text{m} \end{cases} \tag{3.21}$$

The above construction $A(z)$ is exactly the same as the Fischer et al. [4] estimates for the upper 125 m and the lower levels of the model domain are assigned values relative to 125 m based on the following assumptions: (i) the advective transport of heat is proportional to the strength of the current, and (ii) horizontal temperature gradient remains constant below 125 m. Justification of assumption (i) is obvious and assumption (ii) is based on sensitivity experiments that will be described in the next chapter. The estimated heat fluxes are presented in Fig. 3.10. As shown, strong episodic warming and cooling events, with strength upto 80 W m^{-3}, occurred during both the monsoons in sub-surface layers (mostly within upper 80 m depths). These events are much stronger than the warming and cooling trends present in the observed temperature field (upto 20 W m^{-3}) (see Fig. 3.3c), which is biased towards very small-scale (synoptic) variability. Furthermore, this estimate is associated with large uncertainty (Fischer et al. [4]), and hence its role in the simulated temperature may be suspected.
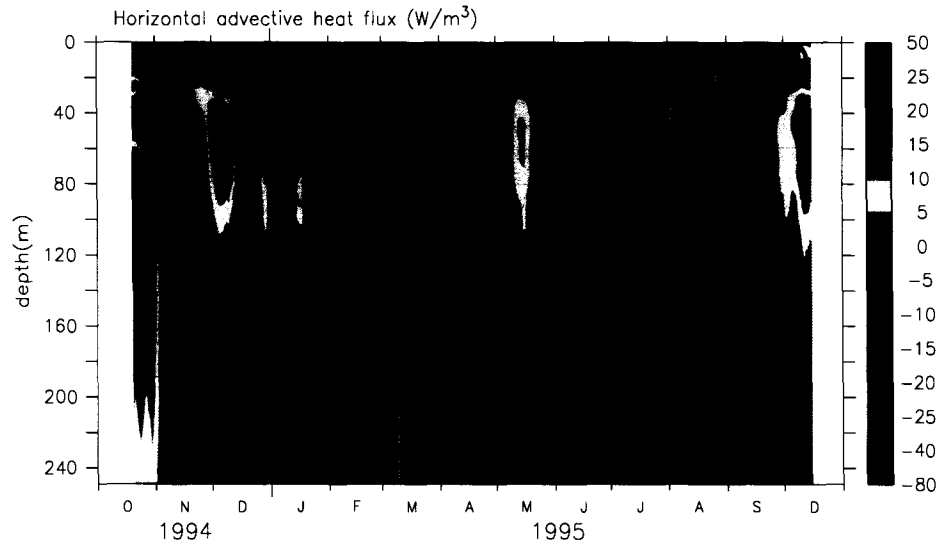
Figure 3.10: Estimates of horizontal advective heat fluxes of heat at the mooring location (see text). The data are smoothed with a 7-day running mean.

3.2.4 Fischer-based estimates of vertical heat advection

As seen from equation 3.20, estimates of vertical velocity (W) and vertical temperature gradient $(\partial T/\partial z)$ are required to determine heat fluxes due to vertical advection. As the model itself predicts the vertical temperature gradient, only the vertical velocity is required.

Fischer et al. [4] estimated vertical velocity at 125 m depth based on the heat budget equation using the following two assumptions: (i) the vertical velocity varies linearly from 0 at the surface to its predicted value at 125 m, and (ii) vertical diffusion does not play any role in the budget. The equation they used to estimate the vertical velocity is:

$$\rho_0 C_p \left[\int_{-h}^{0} \frac{\partial T}{\partial t} dz + \int_{-h}^{0} \underbrace{(U_H \cdot \nabla_H T)}_{hor\, advection} dz + \int_{-h}^{0} \underbrace{W \frac{\partial T}{\partial z}}_{ver\, advection} dz \right] = Q_0, \qquad (3.22)$$

$$W = -W_{-h} \left(\frac{-z}{h} \right). \qquad (3.23)$$

By simplifying above two equations, one can get

$$W_{-h} = \frac{h}{\rho_0 C_p} \frac{\rho_0 C_p \left[\int_{-h}^{0} \frac{\partial T}{\partial t} dz + \int_{-h}^{0} (U_H \cdot \nabla_H T) dz \right] - Q_0}{\int_{-h}^{0} z \frac{\partial T}{\partial z} dz}, \qquad (3.24)$$

where Q_0 is the net surface heat fluxes.

Using the above equation, they estimated the vertical velocity (Fig. 3.11). The estimated vertical velocity is large and mostly negative and episodic (upto 18 m day^{-1}). This method of computation of the vertical velocity is suspected. In the presence of strong variation of horizontal advective heat fluxes along the vertical, the linear assumption to estimating vertical velocity may lead to unrealistic magnitude of the vertical velocity at any depth to compensate residual heat originated from the previous (vertical) levels. Therefore, these estimates need to be examined. For the use of these estimates in the model simulation, vertical profiles of the velocity are constructed for 250 m using the same assumption as made by Fischer et al. [4] for the upper 125 m and using the assumption that the vertical velocity linearly reduces to zero at 250 m.
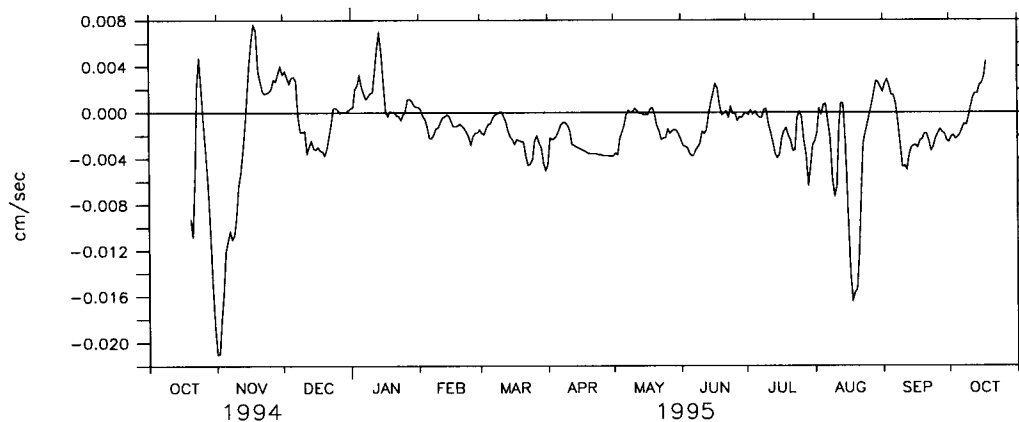
Figure 3.11: Vertical velocity estimated by Fischer et al. [4] at the mooring by balancing the heat budget of upper 125 m layer.

3.2.5 Present study estimates of horizontal advective heat advection: Reynolds–based estimates

In order to asses the robustness of the role of horizontal advection, an alternative estimates of horizontal advective heat fluxes is computed using the time-series of horizontal velocity measured on the mooring from 0 to 250 m (Weller et al. [3]) and the horizontal temperature gradient estimated from Reynolds SST data (spatial resolution $1° \times 1°$; Reynolds and Smith [103]). The gradient is computed only at the surface and is assumed constant with depth. Among the various available optimally interpolated satellite data sets, the Reynolds product compares well with in situ observations (see Fig. 3.12A) and proved reliable in determining the signals associated with low frequency variability (Saji et al. [104]; Sreejith and Shenoi [105]). Although this estimate is based on the same in situ current as used in the first estimates, it is mostly biased towards large variabil-

ity because the temperature gradient is a 1° resolution. As shown in Fig. 3.12B, the SST gradient is strong from January to March and from July to September 1995, and weak during the rest of the year. The horizontal advection estimated is shown in Fig. 3.12. The strongest impacts on the model temperature may be expected from cooling in October–November and in July–August and from warming in December and September. During the inter-monsoon, from mid-January to the end of May, the estimated horizontal advection of heat is weak. This estimate is associated with almost relatively weaker signals of warming and cooling in the sub-surface layer and biased towards large-scale variability.
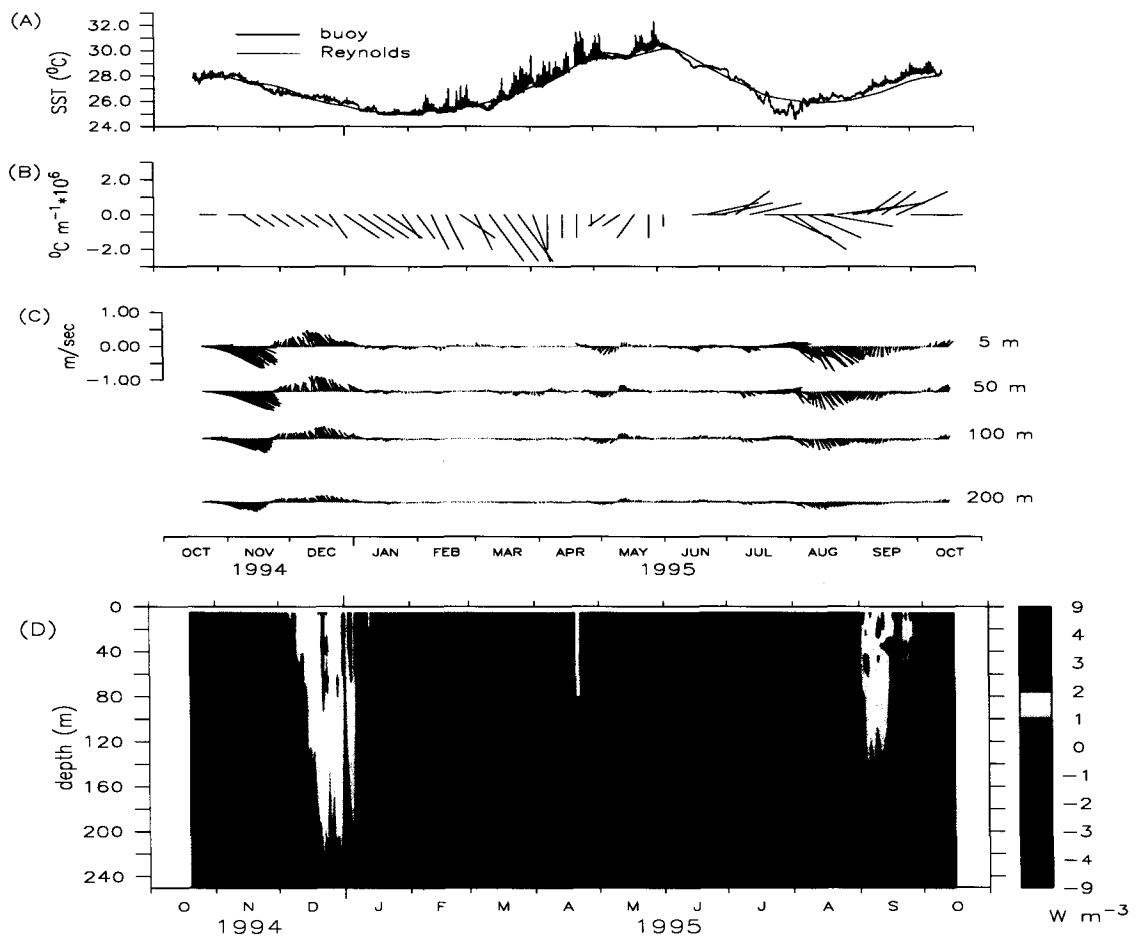
Figure 3.12: (A) Optimally interpolated satellite SST (Reynolds and Smith [103]) and observed SST (Weller et al. [2]) at the mooring location. (B) SST gradient (°C/m) from the data of Reynolds and Smith (1994). (C) Horizontal velocities measured at 5 m, 50 m, 100 m, and 200 m on the mooring line. (D) Estimate of horizontal heat advection (W/m^3).

3.2.6 Present study estimates of vertical advective heat fluxes

As the model itself predict the vertical temperature gradient, only vertical velocity estimate (W) is required to determine heat flux due to vertical advection. It is a major task in oceanography to determine in situ vertical velocity in the ocean owing to its small magnitude (at most a few meters per day). We present below several W estimates.

3.2.6.1 SODA-based estimate

Vertical velocity estimates exist for the global ocean from the output of Simple Ocean Data Assimilation (SODA) Ocean General Circulation Model (OGCM) (with spatial resolution $1° \times 1°$ in the mid latitude and $1° \times 0.45°$ (longitude-latitude) in the tropics, and with one month temporal resolution (Carton et al., [106] and [107])). The data are interpolated to the JGOFS mooring location for the study period. As shown in Fig. 3.13, the vertical velocity exhibits a bimodal annual pattern, with downwelling prevailing from October to December, upwelling prevailing from May to July, and weak values in between. This pattern of vertical velocity matches the Ekman pumping velocity at the location (see Fig. 3.14).
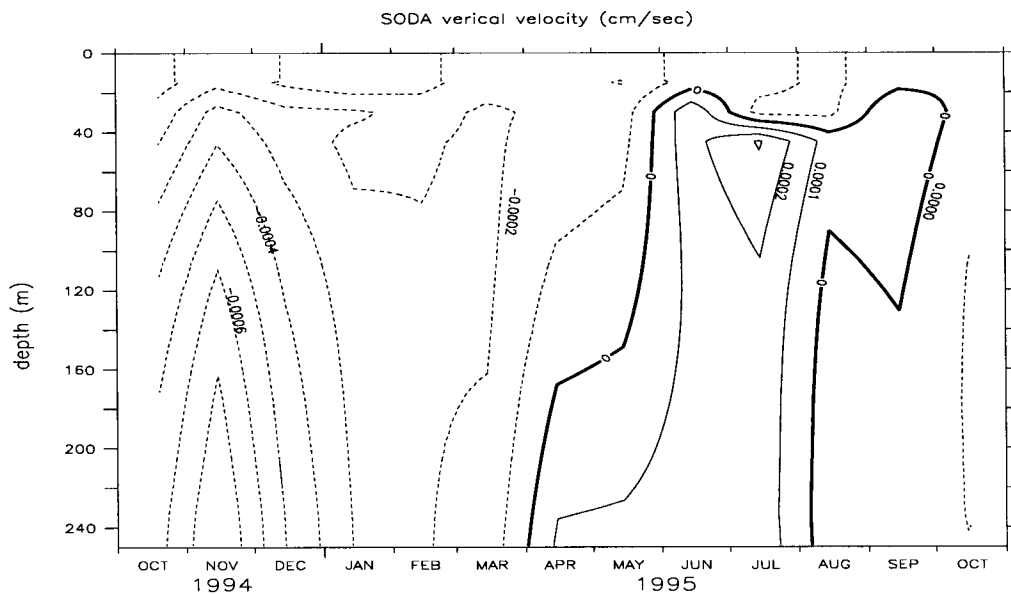
Figure 3.13: Contours of vertical velocity (cm/s) based on SODA OGCM.
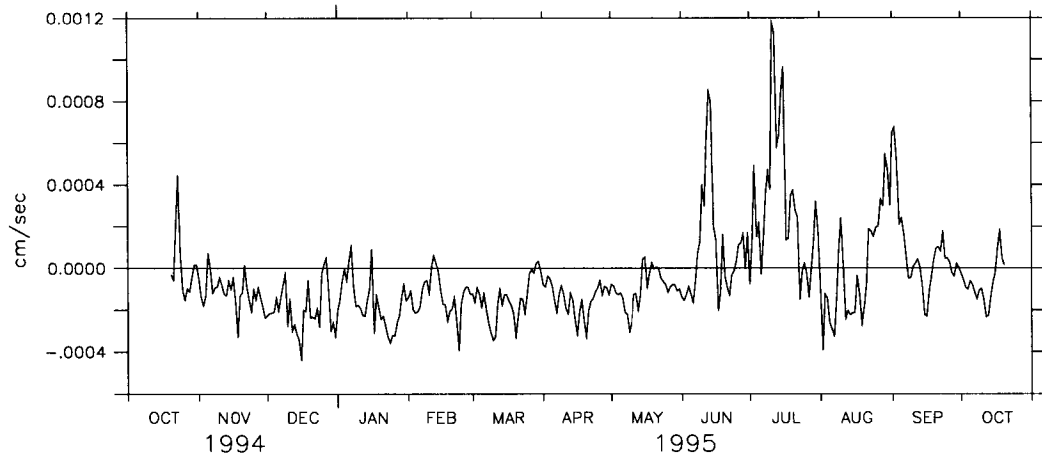
Figure 3.14: Ekman pumping vertical velocity at the moored-array location based on ECMWF [108] winds.

3.2.6.2 Predicting vertical velocity from observed temperature profile

In situ measurements of vertical velocity are not available. All studies use indirect methods to quantify the vertical velocity. Helber and Weisberg [109] estimated the vertical velocity for the equatorial Pacific using the horizontal currents fields (measured by several moorings) through the continuity equation. This method cannot be applied in the present study because of data constraints: though (horizontal) currents were measured on four mooring, these data are not accessible to us. Friedrichs and Hofmann [110] measured the vertical velocity in the equatorial Pacific from the vertical movement of isotherms based on the assumption of geostrophy (see Appendix B). The method of estimating the local vertical velocity from the thermocline excursion is possible under the constraint that horizontal advection does not play any role in excursion of thermocline. Hence, it may not be correct.

Apart from the above estimates of local vertical velocity, the TKE model is used in this study to estimate the vertical velocity (W) at the study location. In principle, an ad-hoc W has to be estimated to close the model heat budget everywhere below the mixed layer. For this, the model is forced with local surface fluxes and estimates of horizontal advective heat fluxes at every time step to simulate the temperature field of the water column (0–250 m). Estimation of vertical velocity between ML and 250 m is carried out at every two hours interval (δt) as follows:

$$W(z) = \left(\frac{T_{ob}(z) - T_p(z)}{\delta t} \right) / \left(\frac{\partial T_{ob}(z)}{\partial z} \right), \tag{3.25}$$

where T_p is the predicted temperature and T_{ob} is the observed temperature profile specified in the model after every δt time interval. After every two hours, the model is reinitialized with the observed temperature profile T_{ob}.

It is not possible to estimate vertical velocity within the ML because of very small vertical temperature gradients. The vertical velocity for the whole domain (0–250 m) is constructed by assuming 0 vertical velocity at the surface and by interpolating (linearly) the values between the surface and one level below the ML. As this estimate is dependent on model simulation, it will be described in the next chapter.

Chapter 4

Numerical experiments

As described in section 3.2, two sets of numerical experiments will be carried out. In the first set the temperature structure will be simulated using estimation of vertical velocity (section 4.1), and in the second set vertical velocity will be simulated using observed temperature profile (section 4.2).

4.1 Temperature structure simulations

Several simulations are carried out to examine the role of the various processes controlling the upper-ocean thermal structure during October 1994 to October 1995 in the central Arabian Sea. Several estimates of the advective heat fluxes will be used. The plan for the experiments is as follows:

Experiment-1: Role of local atmospheric forcing fluxes from Weller et al. [2] (simulation S1).

Experiment-2: Advective heat fluxes based on Fischer et al. [4] is added to S1. This experiment is further divided into two parts.

- (i) Addition of Fischer-based horizontal advection (S2a).

  (Forcing: Atmospheric fluxes + Horizontal advection)

- (ii) Addition of Fischer-based vertical advection (S2b).

  (Forcing: Atmospheric fluxes + Horizontal advection + Vertical advection)

Experiment-3: Advective heat fluxes based on optimally interpolated data (Reynolds [103]) and on the SODA OGCM added to experiment S1. This experiment is further divided into two parts.

- (i) Addition of horizontal advection (S3a)

  (Forcing: Atmospheric fluxes + Horizontal advection).

- (ii) Addition of vertical advections (S3b)

(Forcing: Atmospheric fluxes + Horizontal advection + Vertical advection).

4.1.1 Role of local surface fluxes (simulation S1)

In the first simulation (S1), only the local atmospheric (surface) forcing fluxes are taken into account. These fluxes (Weller et al. [2]) were described in section 3.1.1. These fluxes are dominated by the monsoonal cycle. During the NE monsoon, the ocean surface is subjected to a moderate wind forcing. During the SW monsoon, the ocean surface is subjected to a strong wind forcing and gains heat. During the IMs, the ocean surface is subjected to a weak wind forcing and is continuously heated up by the increasing solar radiation. It is thus expected that SST will decrease and ML will deepen during the NE monsoon owing to convective entrainment driven by net heat loss at the surface, whereas deepening of ML and decrease of SST are expected during the SW monsoon owing to mixing driven by strong winds. Continuous increase of SST and a shallow ML are expected during the IMs owing to strong insolation and reduced nonsolar heat fluxes and wind forcing.

Figure 4.1: Results of the numerical simulation S1 (forcing by atmospheric fluxes): (a) predicted (red) and observed (black) SST; (b) predicted (red) and observed (black) MLD; (c) vertical structure of temperature (color) and MLD (blue line); (d) predicted minus observed temperature; (e) vertical structure of predicted temperature trend (color) and MLD (blue line); (f) predicted minus observed temperature trend. The data in the figure are smoothed with low pass filters: two hours for SST (a); one day for MLD (b), and for temperature profiles (c) and (d); 10 days for the trends of temperature profile (e) and (f).

The results of the (S1) simulation are compared to the observations in Fig. 4.1. As expected, the predicted SST follows an annual cycle similar to that observed (Fig. 4.1a). There are, however, significant differences between them. The predicted SST diverges from the observations during December. The model remains too cool (by 1 °C) until the beginning of the SW monsoon. Then it becomes increasingly too warm (by up to 5-6 °C at the end of the run). The general trends in the predicted MLD are similar to those in the observed MLD throughout the year (see Fig. 4.12). However, significant differences occur, as in the case of SST. In particular, the transient change (meso-scale feature) in November 1994 is not reproduced and the deepening during the NE monsoon is strongly underestimated (50 m predicted in January vs 100 m in the observations). From the end of the NE monsoon the model MLD almost parallels the observations, except for the meso-scale feature in August. Evolution of the predicted vertical temperature profile (Fig. 4.1) shows

that the impact of the surface forcing fluxes does not penetrate deeper than the predicted MLD. The difference between the predicted and the observed temperature is shown in Fig. 4.1d. As expected from the SST behaviour, the temperature predicted for the near surface layer remains close to the observation from the beginning of the study period to the middle of the SW monsoon. After that, the model warms up too much. In contrast, the sub-surface layer is poorly simulated until the middle of the SW monsoon (with a maximum underestimate of 6 °C). As regards the temperature trend (see Fig. 4.1e), none of the sub-surface warming and cooling events are reproduced. As a consequence, the differences between the predicted and observed temperature trends (see Fig. 4.1f) during the monsoonal period are large (more than 4 W m^{-3}), and mostly equal and opposite to the observed trends (see Fig. 3.3c). The difference is not so significant (less than 4 W m^{-3}) during January–June (Spring IM), which suggests that the sub-surface temperature underestimates during the IM (Fig. 4.1d) mostly resulted from the earlier (December) underestimate.

In summary, this simulation shows that the atmospheric forcing explains only the general trend of near-surface layer thermal structure (evolution of SST and MLD). It alone is unable to explain the annual evolution of the whole upper layer. This implies that the role of other (oceanic) processes must be taken into account.

4.1.2 Forcing with Fischer-based estimates of heat advection

4.1.2.1 Forcing: atmospheric flux + Fischer-based horizontal advection (S2a)

In this experiment, in addition to local atmospheric surface forcing (same as in S1), the influence of horizontal advection is also taken into account. These fluxes were, due to Fischer et al. [4] described in section 3.2.3. These fluxes are associated with strong episodic warming and cooling events (strength up to 80 W m^{-3}) during both the monsoons in the sub-surface layers, which are much stronger than the warming and cooling trends present in the observed temperature field (see Fig. 3.3c).

The results (S2a) are compared with the observations in Fig 4.2. The predicted SST rapidly diverges from the observed values from the beginning of the study period (Fig.4.2a). The bias increases up to -6 °C at the end of December as a consequence of strong cooling (15 W m^{-3}, near the surface) by advection. The difference remains more or less constant until the end of the study period. As regards the MLD evolution (see Fig. 4.2b), its deepening is too slow from the beginning of the study period until early December as compared to the observations. After that, the MLD almost coincides with the observations for the rest of the year. The agreement between the predicted MLD of this simulation and the observed MLD is better than for S1.

The predicted evolution of the vertical temperature profile (Fig. 4.2c) shows that the horizontal advection of heat strongly affects the temperature evolution. The sub-surface temperature cools down to 16 °C at 40 m depth during the NE monsoon, and down to 12 °C below 60 m during the SW monsoon. As shown in Fig. 4.2d, the difference between predicted and observed temperature is very large (upto -7 °C) for the whole domain. The excess cooling that occurred during early November within the upper 80 m gradually penetrates the whole vertical domain during the rest of the period, and by the end of July it covers the entire vertical domain (0–250 m). In contrast, the excess warming that occurred in the lower part of the model domain below 80 m during the same period gradually decays and by mid-July, it almost disappears. The predicted temperature trend and the difference between the trends in predicted and observed temperatures are presented in Fig. 4.2. As seen in Fig. 4.2e, unlike in the previous simulation S1, the warming and cooling trends are reproduced in the sub-surface layers, but with significant bias. The predicted trend has huge amplitudes (up to 30 W m^{-3}) from 20 October to mid-November and August to early September. The predicted trend is overestimated significantly during late November to early December (up to 12 W m^{-3}) and then during the end of the simulation (early October 1995; up to 20 W m^{-3}). Outside of these two periods, the difference is not so significant (less than 8 W m^{-3}).

In summary, this simulation S2a (Fig. 4.2) shows that the period from 20 October to mid-November 1994 is the most critical. The excess cooling caused by the horizontal advective heat fluxes during this period in the upper 80 m affects the whole simulation. The horizontal advective heat estimates used during this period are probably responsible for this bias.
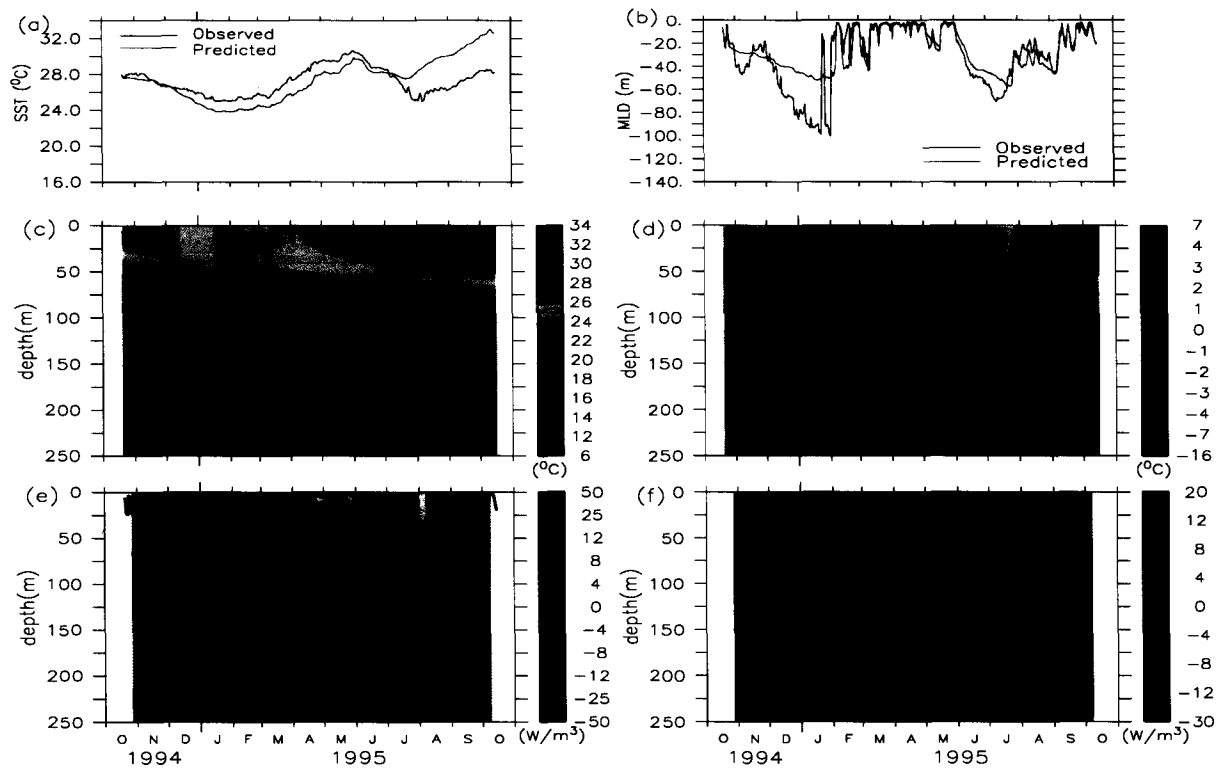
Figure 4.2: Results of the numerical simulation S2a : (a) predicted (red) and observed (black) SST; (b) predicted (red) and observed (black) MLD; (c) vertical structure of temperature (color) and MLD (blue line); (d) predicted minus observed temperature; (e) vertical structure of predicted temperature trend (color) and MLD (blue line); (f) predicted minus observed temperature trend. The data are smoothed as in Fig. 4.1.

4.1.2.2 Forcing: atmospheric fluxes + Fischer-based horizontal advection + Fischer-based vertical advection (S2b)

As described in section 3.2.6.2 Fischer et al. [4] estimated the heat conserving vertical velocity at the study location at 125 m. The same estimate is used to construct the vertical velocity profile for 0-250 m layer using the method described in section 3.2.6.2. These estimates are used to force the model in addition to atmospheric fluxes and horizontal advective heat fluxes. The simulated (S2b) temperature structure is presented in the Fig. 4.3. The results are mostly similar to S2a and clearly show that these vertical velocity estimates are unable to improve the vertical temperature structure obtained with S2a simulation.
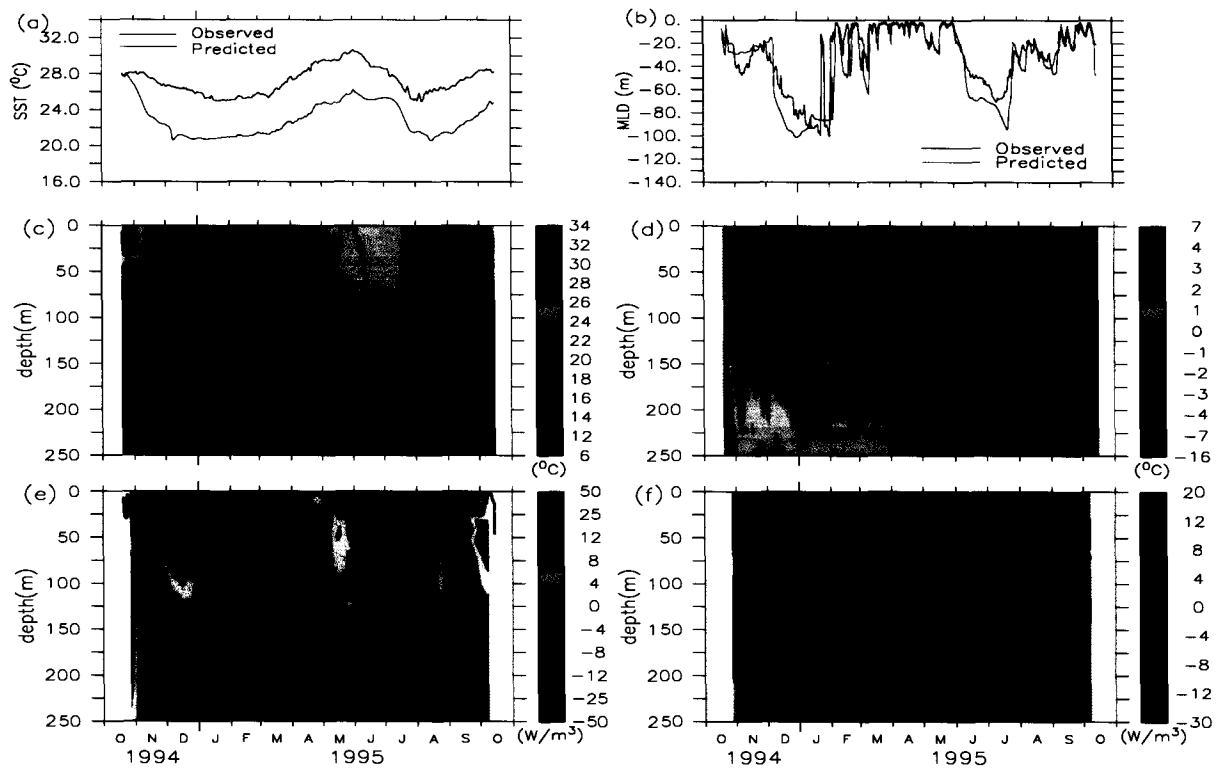
Figure 4.3: Results of the numerical simulation S2b : (a) predicted (red) and observed (black) SST; (b) predicted (red) and observed (black) MLD; (c) vertical structure of temperature (color) and MLD (blue line); (d) predicted minus observed temperature; (e) vertical structure of predicted temperature trend (color) and MLD (blue line); (f) predicted minus observed temperature trend. The data are smoothed as in Fig. 4.1.

4.1.3 Experiments with present study estimates of advective heat fluxes

In the above, the *in-situ* estimates of the horizontal advective heat fluxes based on Fischer et al. [4] were used to examine their role in predicting the temperature structure. These advective heat fluxes are associated with large uncertainties (Fischer et al. [4]) and they did not allow a proper simulation of the temperature evolution. Alternative and independent estimates of the horizontal advective heat fluxes and vertical velocity are therefore required (see section 3.2.5 and 3.2.6), and such estimates are now used to force the model.

4.1.3.1 Forcing: atmospheric flux + Reynolds-based horizontal advection (S3a)

The model is forced with the measured advective heat fluxes based on Reynolds temperature gradient (see section 3.2.5) together with atmospheric fluxes. The results of the simulated temperature structure are presented in Fig. 4.4. As seen in Fig 4.4a, the predicted SST is lower than observed through most of the year, but the agreement is much better than S2a throughout the year and bet-

ter than S1 after the onset of the SW monsoon. From mid-October to mid-November, the cooler waters advected from the northwest (Figs. 3.12c-d) lead to a 1°C underestimate, which is partially compensated by the arrival of warmer waters from the southeast in December. The strongest advection impact occurs during the SW monsoon, due to cooler waters advected first from the west and then from the northwest. This allows the model to remain relatively close to the observations. As regards the MLD evolution (Fig. 4.4b), the main difference with S1 is the increase in the NE monsoon deepening by (up to 60 m in January vs 50 m in S1). Evolution of the vertical profile (Fig. 4.4c) shows that horizontal advection of heat (see Figs. 3.12d) also has an impact on sub-surface variability. As shown in Fig. 4.4d, the difference between model and data is similar to that for S1, except for a slight decrease in the mid-November to mid-December overestimate and for the significant improvement in the surface layer after early July. It is nevertheless worth noting that at sub-surface levels, the model diverges more than does S1 in early November and from August to October. The predicted temperature trend (Fig. 4.4e) and the difference between the predicted and observed temperature trend (Fig. 4.4f) are almost similar to S1.
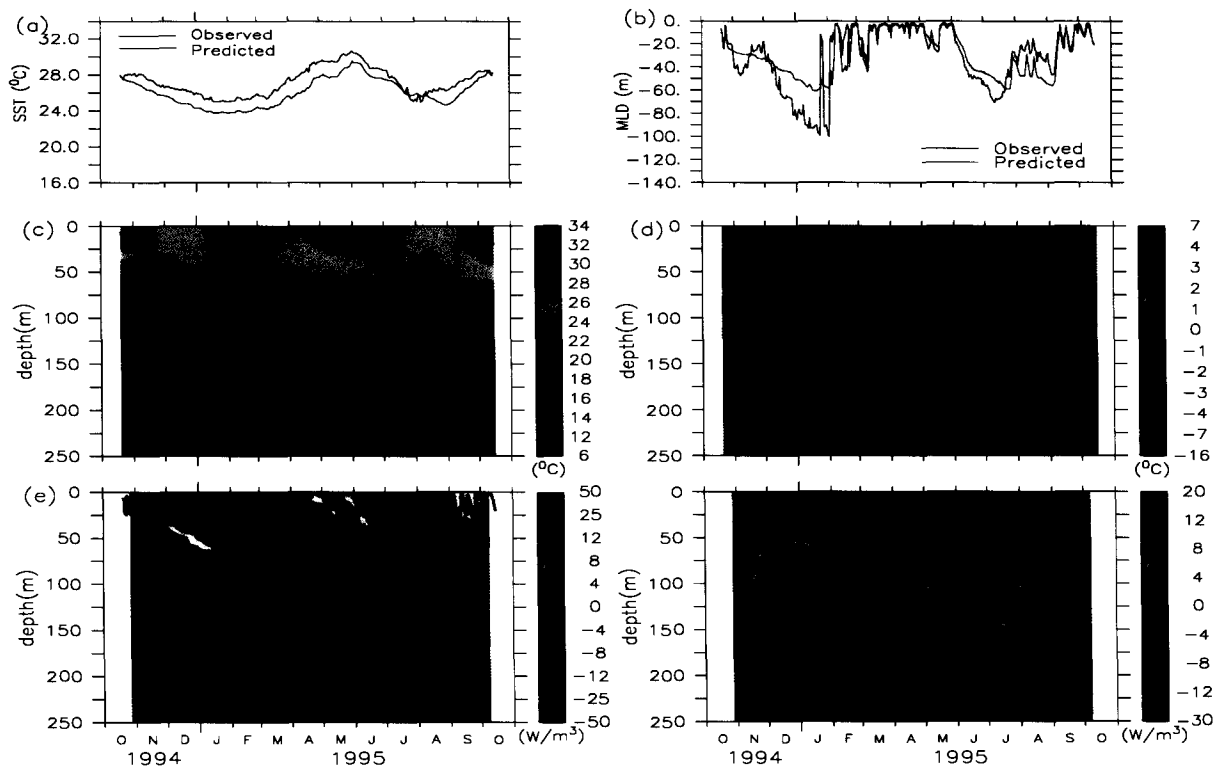
Figure 4.4: Results of the numerical simulation S3a: (a) predicted (red) and observed (black) SST; (b) predicted (red) and observed (black) MLD; (c) vertical structure of predicted temperature (color) and MLD (blue line); (d) modeled minus observed temperature; (e) vertical structure of predicted temperature trend (color) and MLD (blue line); (f) predicted minus observed temperature trend. The data are smoothed as in Fig. 4.1.

4.1.3.2   Forcing: atmospheric fluxes + Reynolds-based horizontal advection + SODA-OGCM-based vertical advection (S3b)
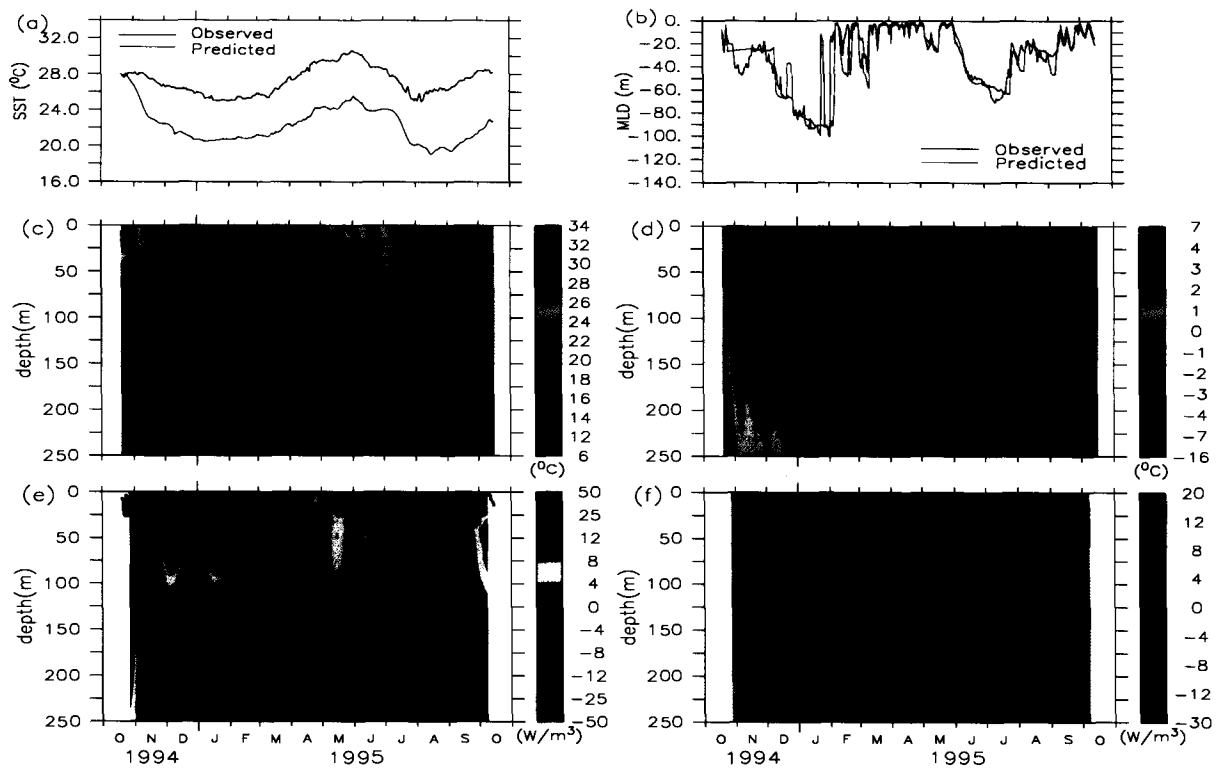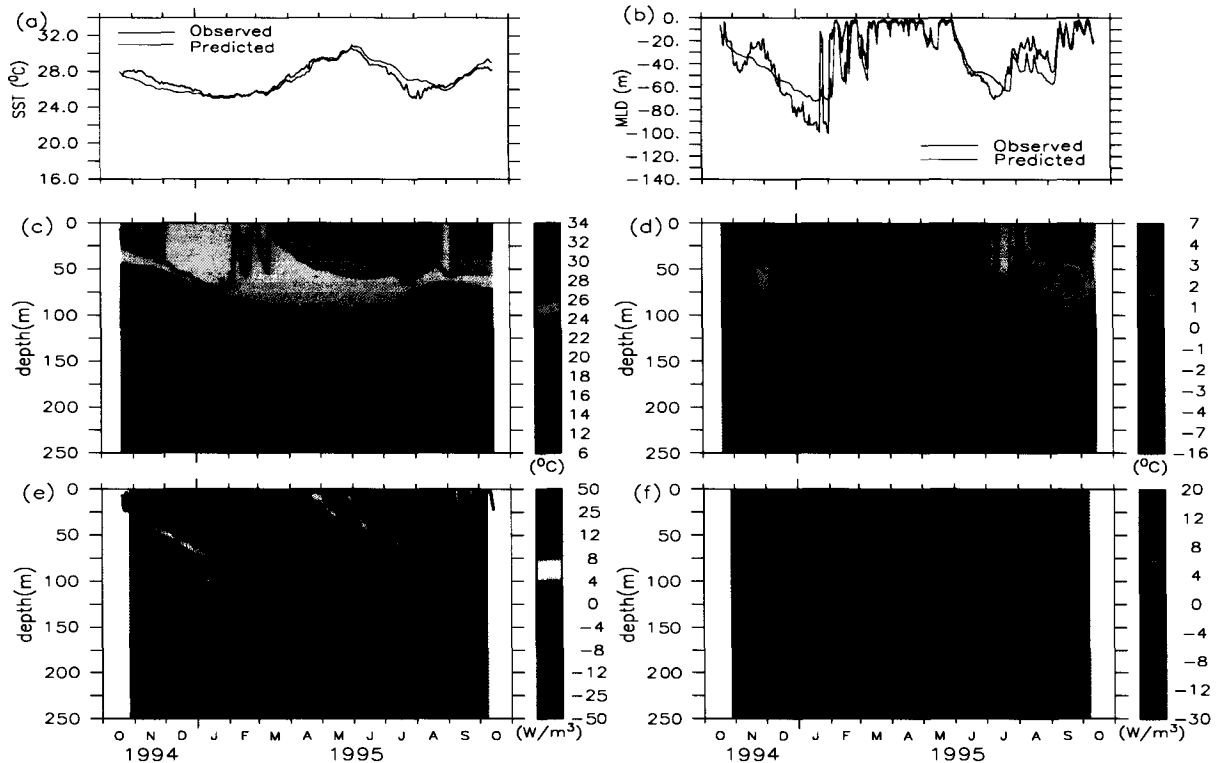

Figure 4.5: Results of the numerical simulation S3b: (a) predicted (red) and observed (black) SST; (b) predicted (red) and observed (black) MLD; (c) vertical structure of predicted temperature (color) and MLD (blue line); (d) modeled minus observed temperature; (e) vertical structure of predicted temperature trend (color) and MLD (blue line); (f) predicted minus observed temperature trend. The data are smoothed as in Fig. 4.1.

To include the impact of vertical advection, only the data of vertical velocity are required as the model uses its own predicted temperature gradient. The data of vertical velocity for this simulation are based on SODA OGCM (see section 3.2.6). In this experiment (S3b), when the combined effect from horizontal and vertical advection are considered, the temperature structure is reproduced well (see Fig 4.13), and is significantly better than earlier simulations (S3a, S2b, and S1). The predicted SST (Fig. 4.13a) remains close to the observations all through the year, except for an underestimate from mid-October to the end of November (1 °C at the most) and for an overestimate between late July and late August (2 °C at the most). As regards the MLD evolution (Fig. 4.13b), the main improvement is the increase in the NE monsoon deepening (now up to 75 m in January). The observed intra-seasonal variations in temperature vertical structure are better reproduced by the model (see Fig. 4.13c); there is considerable improvement in particular at sub-surface

levels. This is a consequence of warm surface water down-welled to the sub-surface during the NE monsoon and weak upwelling of cool water from the deeper ocean to the sub-surface (see Fig. 3.13). The differences between the simulated and the observed temperatures remain small in the near-surface layer all along the year, except for a departure of ~2 °C from late July to mid-August (Fig. 4.13d). At sub-surface levels, significant departures from the observations are still present in a rather narrow depth interval at the base of the ML. Over the year the mean temperature in the mixed layer differs from the observed mean by +0.02 °C and the temperature profiles are simulated with an accuracy of 1.86 ± 1.57 % (mean ± standard deviation) in terms of absolute relative error, while the mean temperature difference is -0.41 °C and the accuracy is (-2.0 ± .05 %) for the 0 – 250 m layer.
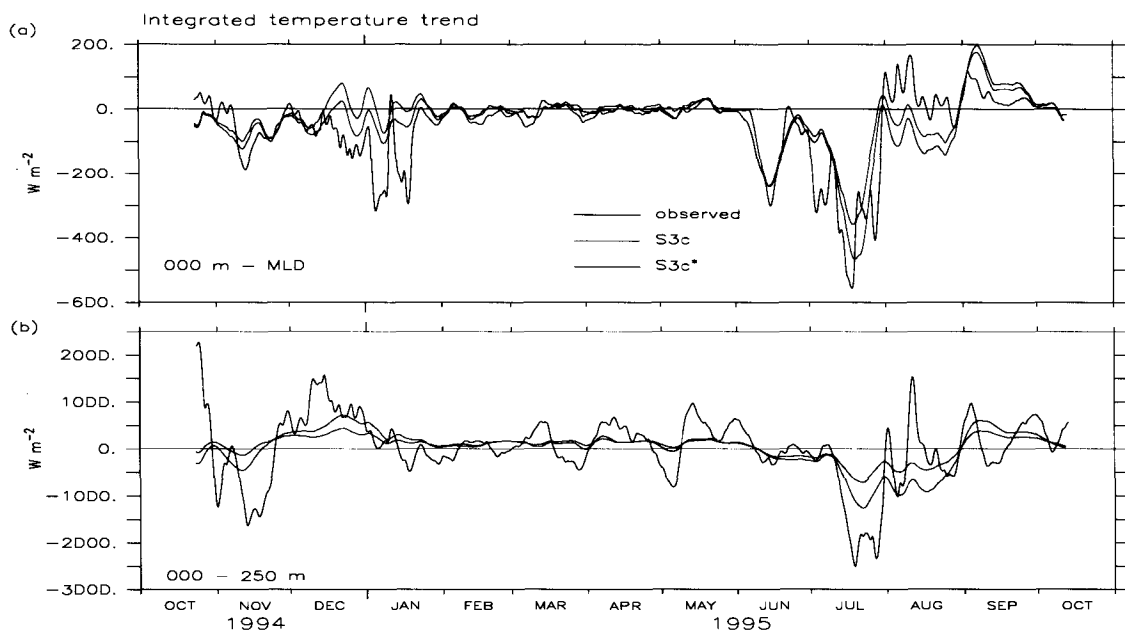
Figure 4.6: (a) Evolution of the observed (black) and the predicted temperature trend integrated over the ML and (b) over the 0–250 m layer (lower panel) for simulations S3b (red) and for S3b* (green) (see text in section4.1.4.4 for simulation S3b*).

The trend in the predicted temperature is integrated over the ML and over the 0–250 m layer and is compared to the observed trend in Figs. 4.6 (in units of heat flux). As shown (upper panel), this simulation could reproduce most of the observed features in terms of magnitude as well as variability for the ML. For the whole simulated layer (lower panel), the variability of main seasonal features are reproduced, but with significantly underestimated amplitude. The short term events (several days to several weeks) are missing.

This result shows the simulation S3b improved considerably from the S2b estimate, but this improvement is, however, not enough as most of small scale events are missing in S3b in the sub-surface (see Figs. 4.6). There are two causes for this: (i) the estimates of horizontal advective fluxes used in the simulation is not proper in the sub-surface, and (ii) the SODA vertical velocity does not contain such variability.

4.1.4 Discussion

4.1.4.1 Sensitivity to atmospheric forcing fluxes

The surface forcing fluxes used in all the above simulations were computed from measurements at the mooring (Weller et al. [2]) at high resolution. It is important to know how sensitive are the model results to possible inaccuracies of atmospheric forcing fluxes. Therefore, a number of sensitivity experiments have been carried out with respect to various atmospheric fluxes in Appendix B.3. Results of the experiments suggest that the predicted SST and MLD do not change significantly for a 10% change in the strength of wind stress: MLD changes by upto 4 m and SST changes by upto $0.2^{\circ}C$ month^{-1} during the SW monsoon only. However, they are highly sensitive to 10% change in either surface-heat gain through solar radiation or loss through long-wave radiation and through turbulent fluxes of latent heat and sensible heat (change is upto 1 $^{\circ}C$ month^{-1} in SST and change in MLD is upto 10 m). The experiment also shows that the predicted temperature structure is the best when the model is forced with the estimated values published by Weller et al. [3].

4.1.4.2 What causes the most general trends in SST and MLD evolution ?

According to Weller et al. [3] and Fischer et al. [4], the general trend of the SST and MLD during the NE monsoon (cooling of SST and deepening of MLD) is due to convective entrainment-mixing driven by buoyancy (heat) loss at the surface, whereas the trend of the MLD and SST during the SW monsoon (deepening of ML and cooling of SST) is due to turbulent mixing driven by wind stress. The earlier study by McCreary et al. [83] suggests that there is significant role of buoyancy-driven mixing in deepening of MLD and in cooling of SST in northern Arabian Sea during the SW monsoon. Sensitivity experiments are carried out with respect to various surface fluxes in Appendix B.3.3. The results of the simulations agree with the conclusion made by Weller et al. [3] and Fischer et al. [4] for the NE monsoon, but not for the SW monsoon. The experiments show that the deepening of MLD during the SW monsoon cannot be explained by wind stress

alone. A significant contribution comes from the buoyancy-driven convective entrainment mixing (in particular during June–July).

4.1.4.3 Fischer-based horizontal advection

The estimates of horizontal advective heat fluxes from Fischer et al. [4] were available only for 0–125 m. These estimates have been used to construct the advective heat fluxes for upper 250 m (see section 3.2.3) ($A(z)$) assuming that the horizontal temperature gradient remains uniform below 125 m. The constructed horizontal advective heat fluxes $A(z)$ are used in S2a (S2b) simulation to predict the temperature evolution. In order to examine the validity of the assumption, the above construction $A(z)$ can be replaced by alternative data constructions by relaxing our assumptions of uniform temperature gradient below 125 m. Two other constructions were considered. Heat flux $A(z)$ was changed according to a 50% decrease and increase in the temperature gradient between 125 m and 250 m depths. Sensitivity experiments show model simulation S2a and S2b remain unchanged. The results of simulations S2a and S2b suggest that Fischer-based horizontal advective heat fluxes are highly biased in the upper 80 m during the early NE monsoon (from 20 October to mid-November 1994) and are responsible for large misestimates of the predicted thermal structure during subsequent periods. Another simulation is carried out by initialising the model on 15 November (instead of 20 October) (see S2a* simulation in Appendix D.1). The simulation confirmed that the enormous cooling driven by horizontal advection of the near-surface layer during the early NE monsoon dominates the model prediction during the rest of the year. Thus this cooling signal in the horizontal advective heat estimates is suspect. During the rest of the year, the estimates of horizontal heat fluxes may be considered good.

The Fischer-based horizontal advective heat fluxes were estimated by using the observed horizontal currents at the central mooring and the horizontal temperature gradient estimated from the three (out of four) associated corner moorings (see Fig. 1.3). These advective heat fluxes are associated with strong signals of warming and cooling events and over most of the year these estimates are under the uncertainly level (Fischer et al. [4]). Temperature structure obtained from the four moorings, north-west mooring (NWM), south-west mooring (SWM), south-east mooring (SEM), and central mooring (CM) (see Fig. F.1 in Appendix F), suggest that the temperature structure from the south-west mooring differs significantly from the temperature structure obtained from the rest of the moorings during November (difference in mean temperature of 50–100 m layer is upto 4°C) and during August (upto 3°C). According to Weller et al. [3], and Fischer et al. [4], satellite altimeter data imagery shows that meso-scale eddies passed through the mooring array during the

early NE monsoon (November) and late SW monsoon (August). The temperature structures from these mooring shows that the south-east mooring reflects strongly this signature, whereas other moorings are less (negligibly) affected by the meso-scale system. Hence Fischer-based horizontal advective heat fluxes might be not representative for the central mooring.

4.1.4.4 Reynolds-based horizontal advection

The second set of horizontal advective heat fluxes (Reynolds-based) used in simulation S3b (S3a) does a significantly better job than the Fischer-based estimates. However, as these estimates are derived from interpolated satellite temperature (see section 3.2.5) combined with in situ current measurements, they suffer from scale inconsistency. Another drawback of these estimates is the assumption that the temperature gradient remains constant over the entire depth range (0–250 m). This assumption is not likely to be perfect. How sensitive is the temperature simulation to horizontal temperature gradient variations with depth ?

To address the issue, another simulation S3b* similar to S3b, is carried out by varying the horizontal advection in the sub-surface layers. The gradient increases to twice its surface value at 80 m and reduces to the surface value at 200 m and remains constant (as the surface value) below. This choice is based on the variability of sub-surface temperature from SODA and from Levitus [29]. The results of the new simulation (S3b*) are expressed in the form of integrated temperature trend over the ML and over the 0–250 m layer, and compared to the earlier results of S3b in Figure 4.6. The results show that the integrated trend over the ML (for the S3b* simulation) is slightly improved during July, but still deviate from the observations during December and August. This implies that the correction in the horizontal advective heat fluxes for the ML is not necessary. Regarding the whole layer, the integrated trend improved significantly during the NE monsoon and during July of the SW monsoon, but the amplitudes of the variations were still significantly weaker than the observations during most of the year.

4.1.5 Concluding remarks

The S1 simulation shows that the local atmospheric forcing fluxes mostly control the near-surface layer thermal structure during the year, but not during the SW monsoon. The near-surface layer thermal structure during the SW monsoon, and the sub-surface layer during most period of the year can not be explained through atmospheric forcing fluxes alone. Comparing S2b to S2a and S1, and S3b to S3a and S1 shows that horizontal advection is mainly responsible for the cooling of the near-surface layer during the SW monsoon.

Two sets of advective heat fluxes have been used to correct the temperature prediction. The prediction based on the first set show high-frequency signals associated with local scales. The prediction based on the second set is more representative of large scales. The vertical velocity estimates involved in the first set of advective correction is not independent of horizontal advection estimates as it is determined as a residual of the heat budget (see Section 3.2.3). The vertical velocity based on SODA-OGCM involved in the second set of advective correction is independent of horizontal advection but it has no high-frequency variability.

Among all the simulations carried out in this section, the SODA-based simulation (S3b) is the best, however, that is still far from the observed temperature structure: most of small-scale signals are underestimated. As there is no any better and independent estimates of vertical velocity available than the SODA-based estimate, we attempt the inverse approach: the model is used to predict the vertical velocity in the following section.

4.2 Prediction of the vertical velocity

The model is now used to predict the vertical velocity instead of predicting the temperature structure. For this, the model is forced with atmospheric fluxes and horizontal advective heat fluxes, together with observed temperature (see Fig. 3.9). The first estimate of vertical velocity will be derived in the case of Fischer-based horizontal advective heat fluxes and the second will be derived in the case of Reynolds-based horizontal advective heat fluxes. The computation technique (for both estimates) was described in section 3.2.6.2.

4.2.1 Estimates of vertical velocity: case of Fischer-based horizontal advection

The estimated vertical velocity is shown in Fig. 4.7 (contour). The associated estimates of vertical advection of heat (colour) is also shown. The estimated vertical velocity is large and structured during the monsoonal periods. In most of the cases the large values of vertical velocity coincides with the large horizontal advective heat fluxes used in the model simulation (see Fig. 3.10). Significant upwelling occurs during early October 1994 (8 m day^{-1}, in the lower domain, below 80 m), late November 1994 (3 m day^{-1}), and late August 1995 (3 m day^{-1}). Significant downwelling occurs (30 m day^{-1}) during October to mid-November 1994 in the upper domain (between surface to 120 m), December (3 m day^{-1}), and during late July to mid-August (10 m day^{-1} just below the ML and is around 3 m day^{-1} below 80 m). From early January to early July, weak vertical movements (mostly episodic, less than 1 m day^{-1}) prevail.

The part of the figure (domain) marked with a red circle (upper 80 m, during 20 October to mid-November 1994) is the most critical period: the corresponding estimated vertical velocity is unrealistically large (more than 30 m day^{-1}). It is worth noting that this huge (negative) amplitude of vertical velocity corresponds to the very large magnitude (strength 80 W m^{-3}) of the horizontal advective heat fluxes (see Fig. 3.10).
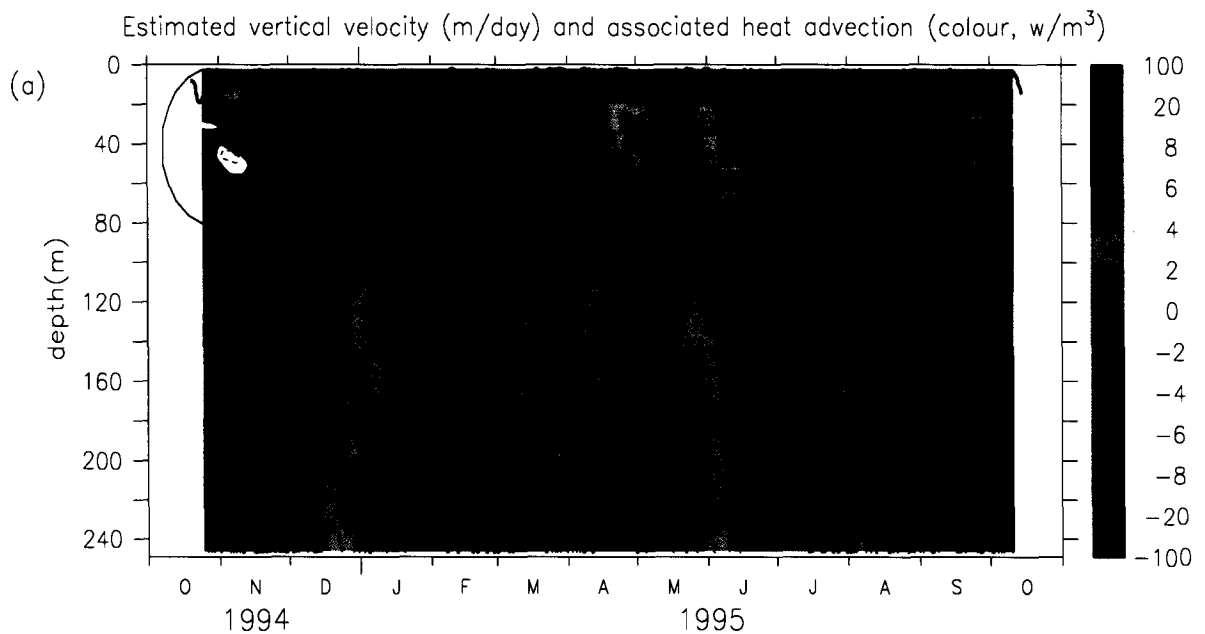
Figure 4.7: (a) Contours of vertical velocity (WFR, m day^{-1}) estimated in the present study. Thin solid lines represent positive velocities; dashed lines represent negative velocities; thick solid lines represent zero velocities. Contour interval: 1 m day^{-1}. Advective heat fluxes: colour, W m^{-3}. MLD: blue line. The red circle corresponds to very high values of WFR (see the text).

These estimated vertical velocities (WFR) at 125 m are compared with the heat-conserving vertical velocities (W_H) as estimated by Fischer et al. [4] in Fig. 4.8. During most of the year, strength of the model velocity WFR is weaker than the heat conserving velocity W_H. During late October 1994, WFR is large and positive (upto 8 m day^{-1}), in contrast to the huge and negative value of WFR (18 m day^{-1}). From early November to late December, both estimates show almost similar variation, with differences in amplitude of the variation. During the first half of January, WFR is negative with strength upto 2 m day^{-1} in contrast to the large positive values of W_H (-6 m day^{-1}). During the Spring IM, variation of WFR is mostly oscillating around zero with amplitude 1.5 m day^{-1} in contrast to mostly negative values of W_H strength upto 2 m day^{-1}. During early SW monsoon (June) both are negligible, and during the rest of the SW monsoon, WFR differs significantly from W_H except for a short duration in early August. The model velocity WFR is

positive during July and August (with strength upto 3 m day^{-1}), in contrast to negative values of W_H during the same periods (with strength upto 5m day^{-1} in July and 14 m day^{-1} in August). During the Autumn IM, WFR is negligible, in contrast to significant negative values of W_H (3 m day^{-1}).
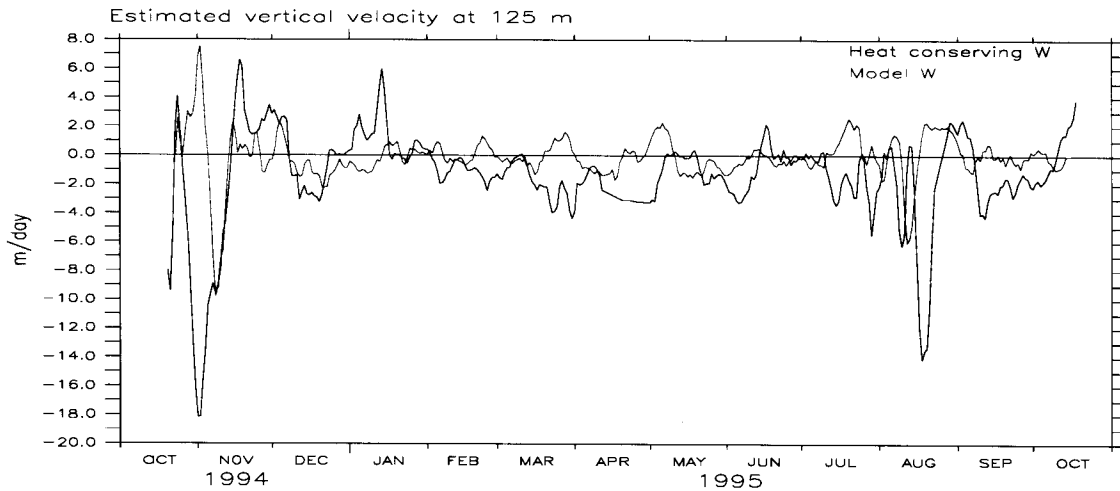
Figure 4.8: Comparison between the heat conserving vertical velocity as estimated by Fischer et al. [4] at 125 m and the model vertical velocity at 125 m.

4.2.1.1 Testing WFR: Temperature simulation with atmospheric fluxes, Fischer-based horizontal advection, and WFR (S2c)

Since we have estimated vertical velocity, these estimates need to be examined for their consistency. Therefore, simulation of temperature field is carried out by forcing the TKE model with the estimated vertical velocity (see Fig. 4.7a) to include the effect of vertical advection together with the corresponding estimates of horizontal advective heat fluxes and local air-sea fluxes (as used in S2a). The prediction is expected to match the observations. The results of the simulation (S2c) are presented in Fig. 4.9. The predicted temperature evolution, as inferred from the structure of predicted SST (Fig. 4.9a), MLD (Fig. 4.9b), temperature profile (Fig. 4.9c), and the difference between the predicted and the observed temperature structure (Fig. 4.9) is unsatisfactory. In contrast, the temperature trend (see Figs. 4.9d and 4.9e) is reproduced well except in the upper 80 m domain during the early NE monsoon (20 October - 15 November 1994). It is clear from Fig. (4.9e) that the actual problem lies within the ML in early NE monsoon. It is worth noting that even strong (strength upto 40 m day^{-1}) downwelling estimated in the ML and just below the ML during

this period is unable to produce sufficient warming to compensate the enormous cooling of about 20 W m^{-3} caused by horizontal advection. Our calculations suggest that the required estimates of vertical velocity should be larger than 250 m day^{-1} in order to compensate the same amount of cooling in the ML driven by horizontal advction.

Figure 4.9: Results of the numerical simulation S2c: (a) predicted (red) and observed (black) SST; (b) predicted (red) and observed (black) MLD; (c) vertical structure of predicted temperature (color) and MLD (blue line); (d) modeled minus observed temperature; (e) vertical structure of predicted temperature trend (color) and MLD (blue line); (f) predicted minus observed temperature trend. The data are smoothed as in Fig. 4.1.
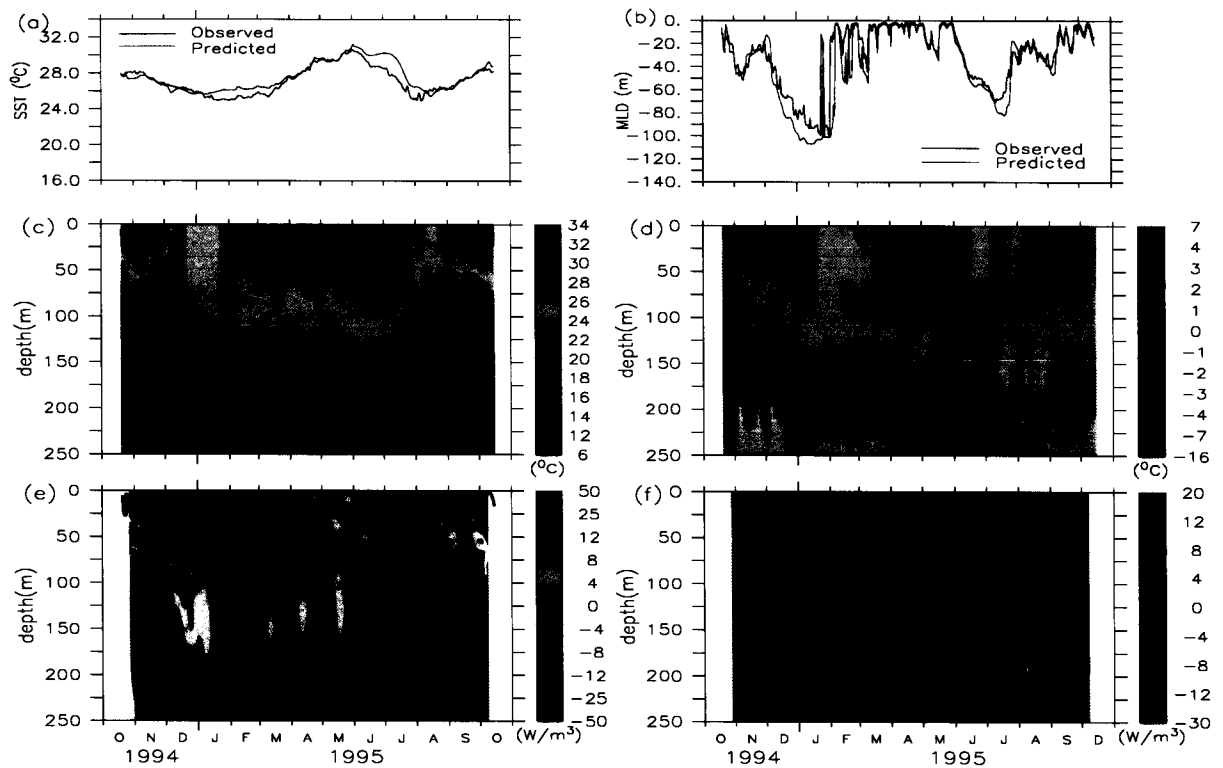
Figure 4.10: Results of the numerical simulation S2c*: (a) predicted (red) and observed (black) SST; (b) predicted (red) and observed (black) MLD; (c) vertical structure of predicted temperature (color) and MLD (blue line); (d) modeled minus observed temperature; (e) vertical structure of predicted temperature trend (color) and MLD (blue line); (f) predicted minus observed temperature trend. The data are smoothed as in Fig. 4.1.

An additional (S2c*) simulation is carried out by assuming a zero value for the horizontal advective heat flux within the ML during early NE monsoon. The predicted temperature structure matches the observation throughout the year at all depths. The predicted SST (Fig. 4.10a), MLD (Fig. 4.10b), vertical predicted temperature structure (Fig. 4.10c) and the predicted temperature trend (Fig. 4.10e) are reproduced well. This result is also seen clearly from the figures of the difference between the predicted and observed temperature (Fig. 4.10d), and in the difference between their trends (Fig. 4.10f). This implies that the vertical velocity as estimated above is consistent with the thermal structure and horizontal advective heat fluxes for all depths except within the MLD during early NE monsoon. This result ensures that horizontal advective heat flux within the ML during the early NE monsoon is not correct.

4.2.2 Estimating the vertical velocity: case of Reynolds-based horizontal advection

The model is used to estimate the vertical velocity using the same method as used above, but now using Reynolds-based horizontal advection (section 3.2.5). The predicted vertical velocity for the case is presented in Fig. 4.11 (contour). The associated estimate of vertical advection of heat (colour) is also shown. The estimates of vertical velocity are large and structured during both NE monsoon and SW monsoon. Weak and episodic vertical movements are present during the inter-monsoons. Strong upwelling occurs during November (4 m day^{-1}), July (4 m day^{-1}), and second half of August (2 m day^{-1}). Strong downwelling occurs during December (4 m day^{-1}) and mid-August (4 m day^{-1}).
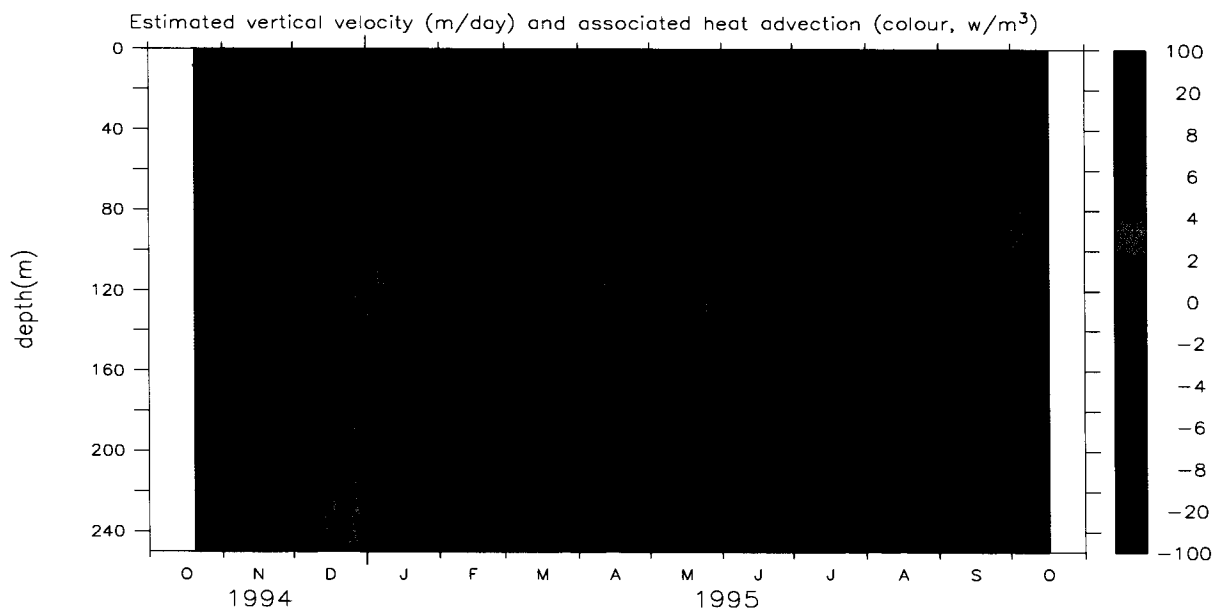
Figure 4.11: (a) Contours of vertical velocity (m/day) estimated in the present study: solid lines - negative velocities; dashed lines - negative velocities; thick solid lines - zero velocities. The contour intervals are 1 m day^{-1}. Associated estimates of advective heat fluxes (colour, W m^{-3}) are also shown together with MLD (blue line).

The estimated vertical velocity (WRR) at 100 m is averaged over two months and compared with SODA-based vertical velocity (WS) and Ekman pumping (WEk) velocity in Fig. 4.12 (as resolution of SODA vertical velocity is one month). All the estimates are comparable to each other and are of same phase during most of the year. They show downwelling during the NE monsoon and upwelling during the SW monsoon. The predicted estimates are relatively stronger (two times) than WS and WEk.
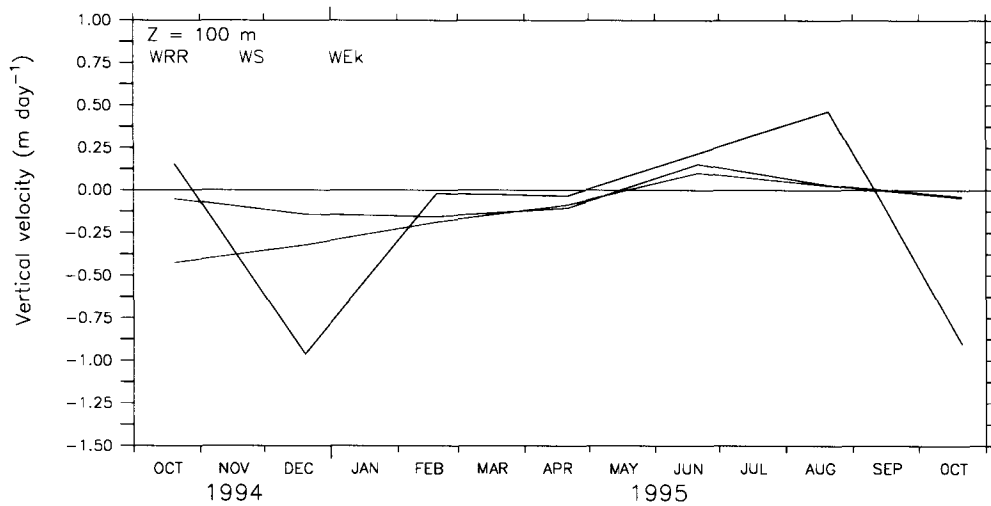
Figure 4.12: Predicted vertical velocity (WRR) at 100 m compares with the SODA-based vertical velocity (WS) and Ekman pumping velocity (WEk) based on ECMWF wind stress. The data are averaged over two months.

4.2.2.1 Testing WRR: Temperature simulation with atmospheric fluxes, Fischer-based horizontal advection, and WRR (S3c)

As we estimated vertical velocity, these estimates need to examined for their consistency. Therefore, simulation of temperature field is carried out by forcing the TKE model with the estimated vertical velocity (see Fig. 4.11) to include the effect of vertical advection together with the corresponding estimates of horizontal advective heat fluxes and local air-sea fluxes (as used in S3a). The prediction is expected to match the observations. The results of the simulation (S3c) are presented in Fig. 4.13. As shown, the thermal structure is reproduced well. The predicted SST (Fig. 4.13a) and MLD (4.13a) remains close to the observations all through the year. The observed intraseasonal variations in temperature vertical structure are reproduced well (see Fig. 4.13c). The differences between the simulated and the observed temperatures remain small (within $\pm 1°C$) at all depths (Fig. 4.13d). As regards temperature trend, all the cooling and warming trends in the sub-surface layers are reproduced well (Fig. 4.13e-f).
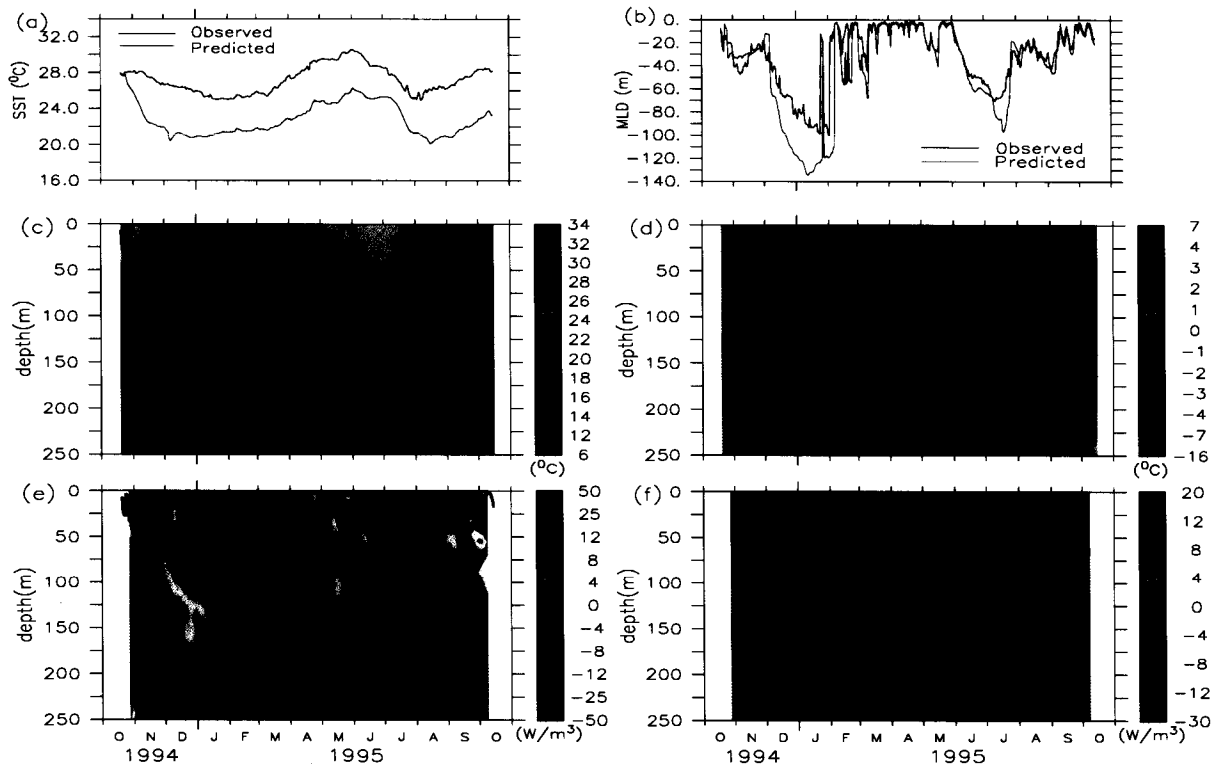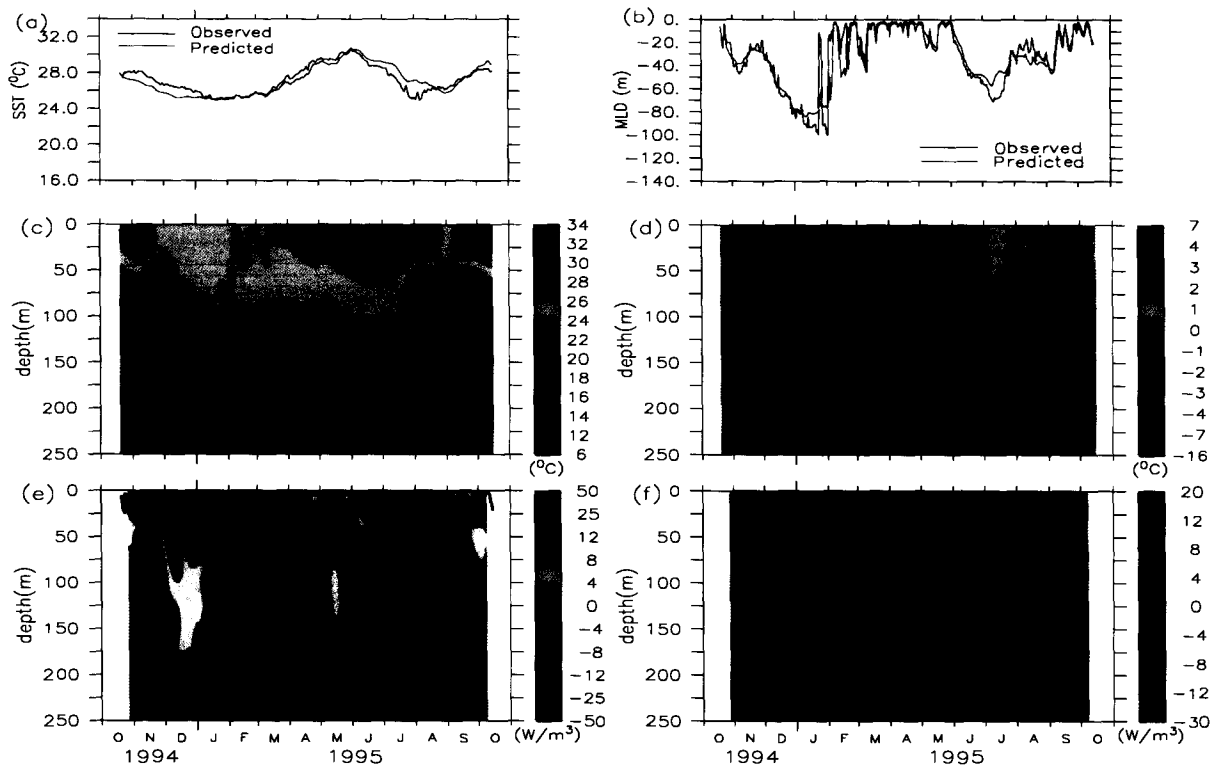
Figure 4.13: Results of the numerical simulation S3c: (a) predicted (red) and observed (black) SST; (b) predicted (red) and observed (black) MLD; (c) vertical structure of predicted temperature (color) and MLD (blue line); (d) modeled minus observed temperature; (e) vertical structure of predicted temperature trend (color) and MLD (blue line); (f) predicted minus observed temperature trend. The data are smoothed as in Fig. 4.1.

4.2.3 Comparison between the two predicted vertical velocities

A comparison between the two estimates of vertical velocity (WFR, corresponding to Fischer et al. [4] estimates of horizontal advection, and WRR, corresponding to horizontal advection based on Reynolds temperature gradient) is presented in Fig. 4.14. The velocities at 5 m below the ML and at 100 m are presented in Fig. 4.14a and Fig. 4.14b respectively. The average vertical velocity between the MLD and 125 m is presented in Fig. 4.14c. It can be seen that WFR differs significantly from WRR during the period when the first estimates of horizontal advective heat fluxes are associated with strong signals of warming and cooling events; else, both estimates are similar. The features common to both estimates are downwelling during mid-December to early January (3 m day^{-1}) and during mid-August (2 m day^{-1}), and upwelling during early May and late August (2 m day^{-1}). The downwelling is more pronounced in the deeper layers (at 100 m) and upwellings is more pronounced near the ML. Both estimates show weak vertical movement

during most of the inter-monsoons.
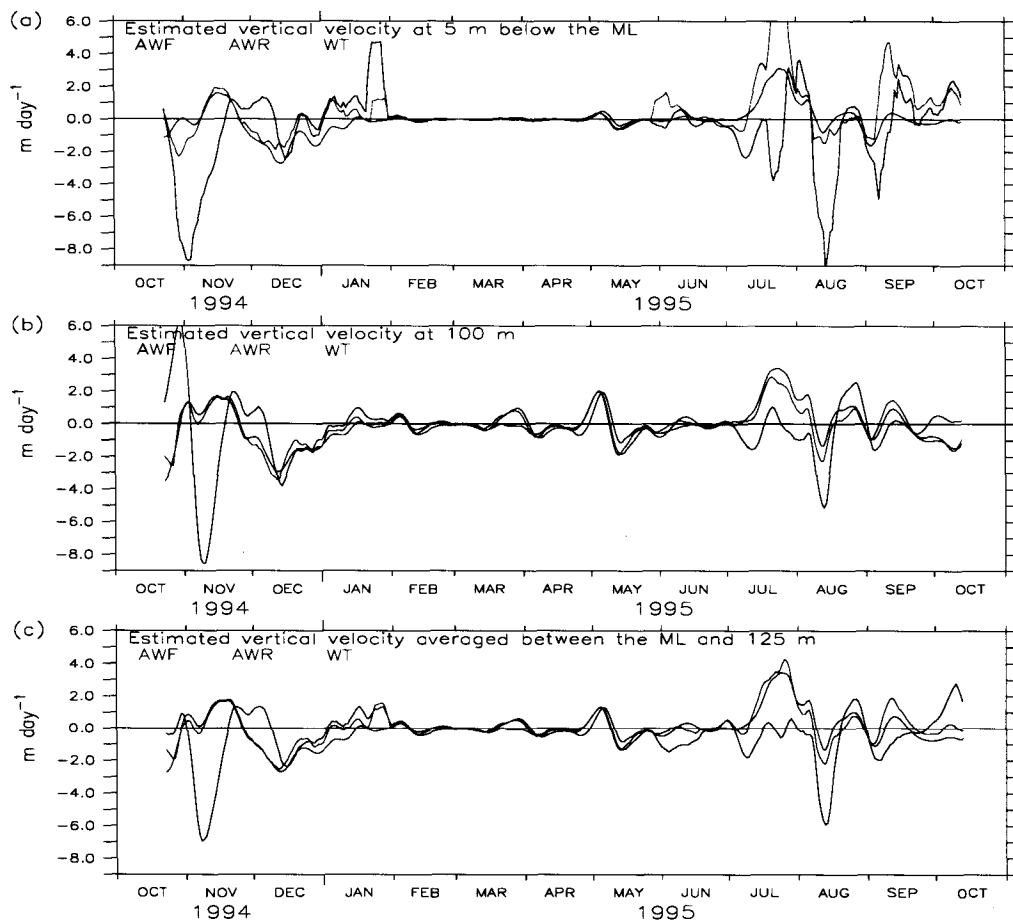
Figure 4.14: Comparison between the predicted estimates of vertical velocities (WFR: closure to the horizontal advective heat fluxes based on Fischer et al. [4] estimates; AWR: closure to the horizontal advective heat fluxes based on Reynold's T gradient) and vertical velocity estimated based on Isotherm excursion (WT). (a) Vertical velocity at 10 m below the ML (b) vertical velocity at 100 m, (c) velocity averaged between the ML and 125m.

It is worth analysing what process generates the estimated vertical velocity. For this, the vertical velocity due to Ekman pumping was computed using ECMWF winds and compared with the predicted vertical velocities WFR and WRR in Fig. 4.15. The comparison suggests that the strong vertical velocity during the NE monsoon does not depend on local wind stresses, implying that the velocities during this period are mostly driven by geostrophy. The vertical velocity during the SW monsoon is driven partly by local wind stresses and partly by geostrophy.
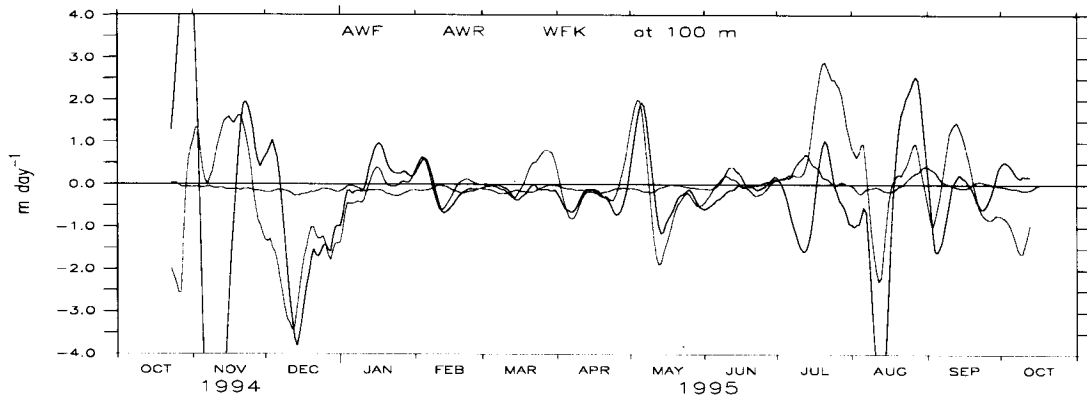
Figure 4.15: Comparison between the predicted vertical velocities at 100 m and Ekman pumping vertical velocity estimated using ECMWF winds at the study location.

4.2.4 Discussion

The method used to predict the vertical velocity helps in reproducing the vertical structure. The main limitation of the method is that it cannot predict the vertical velocity within the ML. The linear interpolation of the vertical velocity (between zero at surface and model predicted value at one level below the MLD) may not be appropriate. Imperfect temperature prediction in simulation S2c (section 4.2.1.1) is due to this interpolation.

The analysis (section 4.2.1.1) of simulation S2c leads us to question the enormous cooling present in Fischer et al.'s [4] estimate of horizontal advective heat fluxes within the ML during early NE monsoon (mid-October to mid-November). The simulation S2c* was carried out, similar to S2c, by assuming a zero value for the horizontal advective heat flux within the ML during early NE monsoon. The predicted temperature structure matches the observation throughout the year at all depths. This is an additional clue that Fischer et al. [4] estimates are wrong for this period. The excess cooling during the early NE in their estimate is an artifact.

Both the predicted vertical velocities WFR and WRR are dependent on the horizontal advective heat fluxes and atmospheric forcing fluxes and thus reflect the possible errors in these forcing fluxes. The atmospheric fluxes used in the model are accurate (hardly 2–3% error) (as implied in the sensitivity experiment carried out in section B.3). Fischer-based advective heat fluxes are associated with large uncertainties (Fischer et al. [4]). Reynolds-based horizontal advective heat fluxes may also contain large errors in the sub-surface (due to the assumption used to extrapolate the surface SST gradient). It is thus important to examine the sensitivity of the estimated WFR and

WRR to the horizontal advective heat fluxes. The results of simulations corresponding to a 50% increase and decrease in Fischer-based horizontal advective heat flux (see Fig. F.2a in Appendix F) show that the upwelling during late-November, during early May, and during late-August, and downwelling during December are not influenced by the change, whereas the downwelling during early November and during July–August are affected significantly by the changes (strength of downwelling during early November reduce from 7 m day^{-1} to 2 m day^{-1}, and downwelling during July–August becomes an upwelling if the Fischer-based flux is decreased by 50%). Similar experiments with the Reynolds-based flux suggest that the features in predicted vertical velocity (WRR) are not influenced by a 50% change (see Fig. F.2b in Appendix F).

Though the predicted vertical velocities WFR and WRR are derived using two different sources of horizontal advective heat fluxes, they agree in predicting significant downwelling during December (upto 3 m day^{-1}), relatively weak downwelling during May and August (upto 1.5 m day^{-1}), significant upwelling during late-November, early-May, and August (upto 2 m day^{-1}). These sensitivity analyses also suggest that upwelling could prevail during July to early August.

The WFR (corresponding to Fischer-based horizontal advection) is much weaker than the heat conserving vertical velocity W_H of Fischer et al. [4]. This leads us to question the method of their estimation. The WRR is stronger than the estimates of SODA-based vertical velocity, however, their seasonal evolution is in phase.

By assuming that the contributions of horizontal advection to the vertical movement of thermocline in the sub-surface layer is negligible, vertical velocity (WT) has been estimated from the observed temperature profiles using the technique presented in appendix E. These estimates of WT are mostly the same as the predicted vertical velocity corresponding to the Reynolds-based horizontal advective heat fluxes (see Fig. 4.14). The strength of WT is upto 4 m day^{-1} and the seasonal variability associated with this estimate is quite similar to SODA-based vertical velocity.

4.2.5 Concluding remarks

The analysis of predicted vertical velocity (WFR and WRR) suggests that during the NE monsoon and SW monsoon, vertical velocity is strong. There is downwelling during December and August and upwelling during July and late August. Vertical movement is weak during the inter-monsoons. This implies vertical advection is an important process in controlling the thermal structure during the monsoons.

Chapter 5

Heat Budget Analysis

The simulations achieved (chapter 4) allow us to compute the contribution of processes (atmospheric fluxes, horizontal advection, vertical advection, and vertical diffusion) to the heat budget of the upper central Arabian Sea. The simulations S2c (based on Fischer-based advective heat fluxes) and S3c (based on Reynolds-based advective heat fluxes) were selected for the analysis. Comparison between the two budgets allows a discussion of their robustness.

5.1 Fischer-based budget (S2c)

The contributions of the different processes to the total trend over the near-surface layer (0–50 m) and over the 0–250 m layer throughout the year are presented in Fig. 5.1 (a & b). In the near-surface layer, all processes (horizontal advection, vertical advection, vertical diffusion, and local air-sea fluxes) are important. In contrast, when the entire (0–250 m) layer is considered, the instantaneous balance is essentially between horizontal and vertical advection. Surface forcing plays a smaller role and vertical diffusion makes the smallest contribution. The trends of horizontal and vertical advective heat fluxes vary significantly at the scale of a few days to a few weeks. During most of the year, these two processes compete with each other to produce the resultant trend. The net contributions of the four processes to the heat content variations of the 0–50 m layer and of the 0–250 m layer were averaged (and integrated) over the 4 characteristic periods and for the whole year. The results are presented in Table 5.1 and Table 5.2.
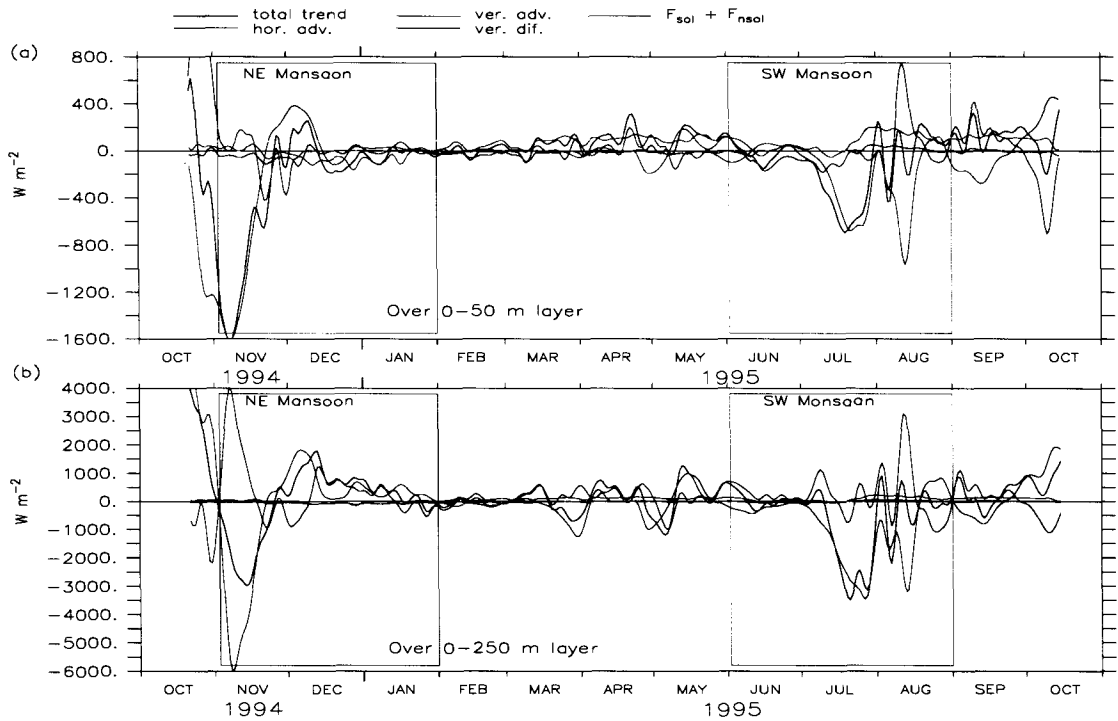
Figure 5.1: The contribution of different processes to the total temperature trend of the near-surface (0–50 m) layer (in units of heat fluxes) for simulation S2c: horizontal advection (red line); vertical advection (green line); vertical diffusion (blue line); combined non solar and solar local surface (heat) fluxes (cyan line). (b) same as (a), but for the 0–250 m layer. The monsoonal periods (NE Monsoon and SW Monsoon) in the figures are highlighted with pink rectangles. Note: the variables in the figure are smoothed by 7-day running mean.

5.1.1 Budget analysis for the 0–50 m layer

During the NE monsoon, the near-surface layer undergoes a net cooling of 1.68×10^9 J m^{-2} at the rate of (-220 W m^{-2}) (Table 5.1). This cooling results from the excess of heat loss through horizontal advection at the rate of 196 W m^{-2}, air-sea fluxes at the rate of 42 W m^{-2}, and vertical advection at the rate of 18 W m^{-2} over heating effects from vertical diffusion at the rate of 36 W m^{-2}. As shown in Fig. 5.1a, these four contributions vary significantly during this period. During early NE monsoon (November to mid-December), horizontal advection goes a large variation and provides large variability in the total trend. During rest of the NE monsoon, the total trend essentially results from comparable contributions from local surface fluxes, horizontal advection, and vertical diffusion.

Over the Spring IM, the near-surface layer gains 8.24×10^8 J m^{-2} heat at the rate of 79 W m^{-2}. This positive heating rate results mainly from the dominating heating effects of local air-sea fluxes (78 W m^{-2}) and from negligible contributions of other processes. As seen in Fig. 5.1a, most of the variability of the near-surface layer is dominated by local air-sea fluxes, whereas the remaining processes compensate each other.

The SW monsoon net cooling (8.53×10^8 J m^{-2}) of the near surface layer is achieved at the rate of 107 W m^{-2}. This cooling results from dominating cooling effects of horizontal advection at the rate of 183 W m^{-2} and from relatively smaller contribution of vertical diffusion at the rate of 26 W m^{-2} over opposing surface heating at the rate of 73 W m^{-2} and heating due to vertical advection at the rate of 29 W m^{-2}. The variability is at its highest for the four processes during this period (Fig 5.1).

The Autumn IM net warming (4.47×10^8 J m^{-2}) results at the rate of 110 W m^{-2}, with positive contributions from surface fluxes at the rate of 98 W m^{-2} and from horizontal advection at the rate of 25 W m^{-2}. Contributions of vertical advection and vertical diffusion are very small. During this period (similar to the Spring IM), the local air-sea fluxes mostly control the variability, with the remaining processes compensating each other (Fig. 5.1a).

The net cooling over the studied year (1.21×10^9 J m^{-2}) is achieved at the rate of 39 W m^{-2}. This cooling results from the excess heat removed by horizontal advection at the rate of 119 W m^{-2} over the positive heat input by surface forcing at the rate of 48 W m^{-2} and by vertical advection at the rate of 32 W m^{-2}. Contribution of vertical diffusion is negligible.

Table 5.1: Average and integrated heat content variation of the 0–50 m layer for simulation S2c (in W m^2 and J m^{-2}) during four characteristic periods of the year during 20 October 1994 to 17 October 1995 are presented. Negative values indicates heat loss from the ocean.

Rate of heat content variation Period	Resultant W m^{-2} (J m^{-2})	Local surface fluxes W m^{-2} (J m^{-2})	Horizontal advection W m^2 (J m^{-2})	Vertical advection W m^{-2} (J m^{-2})	Vertical diffusion W m^{-2} (J m^{-2})
NE Monsoon 1-Nov.-94 :31-Jan.-95	-220.2 (-1.68×10^9)	-41.62 (-3.31×10^8)	-196.4 -1.56×10^9	-18.38 (-3.42×10^8)	$+36.22$ $(+3.56 \times 10^8)$
Spring IM 1-Feb.-95:31-May-95	$+78.79$ $(+8.24 \times 10^8)$	$+77.72$ $(+8.19 \times 10^8)$	-7.49 (-7.83×10^7)	$+12.32$ $(+1.29 \times 10^8)$	-4.40 (-4.60×10^7)
SW Monsoon 1-Jun-95:31-Aug.-95	-107.40 (-8.53×10^8)	$+73.19$ $(+5.82 \times 10^8)$	-183.40 (-1.46×10^9)	$+29.35$ $(+2.33 \times 10^8)$	-26.52 (-2.10×10^8)
Autumn IM 1-Sep.-95:16-Oct-95	$+110.10$ $(+4.47 \times 10^8)$	$+100.5$ $(+4.00 \times 10^8)$	$+25.44$ $(+1.033 \times 10^8)$	-6.89 (-2.78×10^7)	-7.02 (-2.85×10^7)
Whole Year 20-Oct-94:16-Oct-95	-38.68 (-1.210×10^9)	$+48.3$ (1.52×10^9)	-119.2 (-3.74×10^9)	$+32.42$ $(+1.02 \times 10^8)$	-0.22 (-0.043×10^8)

Table 5.2: Average and integrated heat content variation of the 0–250 m layer for simulation S2c (in $W\,m^{-2}$ and $J\,m^{-2}$) during four characteristic periods of the year during 20 October 1994 to 17 October 1995 are presented.

Rate of heat content variation Period	Resultant $W\,m^{-2}$ $(J\,m^{-2})$	Local surface fluxes $W\,m^{-2}$ $(J\,m^{-2})$	Horizontal advection $W\,m^{-2}$ $(J\,m^{-2})$	Vertical advection $W\,m^{-2}$ $(J\,m^{-2})$	Vertical diffusion $W\,m^{-2}$ $(J\,m^{-2})$
NE Monsoon 1-Nov.-94 :31-Jan.-95	-5.30 (-4.21×10^7)	-41.62 (-3.31×10^8)	-334.5 (-2.66×10^9)	$+370.9$ $(+2.95 \times 10^9)$	-0.04 (-0.003×10^8)
Spring IM 1-Feb.-95:31-May-95	$+127.7$ $(+1.33 \times 10^9)$	$+100.0$ $(+1.05 \times 10^9)$	-93.3 (-9.75×10^8)	$+120.7$ $(+1.26 \times 10^9)$	$+0.07$ $(+0.006 \times 10^8)$
SW Monsoon 1-Jun-95:31-Aug.-95	-400.7 (-3.18×10^9)	$+89.9$ $(+7.15 \times 10^8)$	-720.7 (-5.73×10^9)	$+230.1$ $(+1.83 \times 10^9)$	-0.01 (-0.0006×10^8)
Autumn IM 1-Sep.-95:16-Oct-95	$+402.1$ $(+1.60 \times 10^9)$	$+119.0$ $(+4.72 \times 10^8)$	$+273.50$ $(+1.08 \times 10^9)$	$+5.69$ $(+3.85 \times 10^7)$	$+0.04$ $(+0.002 \times 10^8)$
Whole Year 20-Oct-94:16-Oct-95	$+44.61$ $(+1.40 \times 10^9)$	$+67.49$ $(+2.11 \times 10^9)$	-81.62 (-2.56×10^9)	$+162.6$ $(+5.085 \times 10^9)$	$+0.02$ (-0.006×10^8)

5.1.2 Budget analysis for the 0–250 m layer

As regards the whole simulated layer (Table 5.2), the NE monsoon net cooling (4.21×10^7 J m^{-2}) occurs at the rate of 5 W m^{-2}. This small rate of cooling is due to dominating effect of large heat losses through horizontal advection (335 W m^{-2}) and through the atmospheric fluxes (22 W m^{-2}) over large heating by vertical advection (370 W m^{-2}). As shown in Fig. 5.1, the competition between the horizontal and vertical advection during this period is significant. During early November to mid-December, vertical advection essentially opposes the large change in the trend caused by horizontal advection. During the rest of the NE monsoon, the total trend is mostly controlled by vertical advection; at this time, contribution of horizontal advection is much weaker.

The spring IM net warming (1.33×10^9 J m^{-2}) is achieved at the rate of 127 W m^{-2}. This warming rate is largely due to heating through the interface (100 W m^{-2}) and mutual competition between the heating due to vertical advection (120 W m^{-2}) and cooling due to horizontal advection

(93 W m^{-2}). Figure 5.1b shows that competition between the horizontal and vertical advection is mostly responsible for the variability in the total trend during this period.

The SW monsoon net cooling (3.18 × 10^9 J m^{-2}) is achieved at the rate of 400 W m^{-2}. This cooling results mainly from high heat removal by horizontal advection at the rate of 721 W m^{-2}, which is partially compensated by significant heating by vertical advection at the rate of 230 W m^{-2}; at this time, there is a relatively small positive influx through the interface (90 W m^{-2}). During this period, horizontal and vertical advection undergo high and similar variations (Fig. 5.1b).

The Autumn IM net warming (1.60 × 10^9 J m^{-2}) is achieved at the rate of 402 W m^{-2}. This warming results mainly from heating by horizontal advection at the average rate of 273 W m^{-2} and surface forcing at the average rate of 119 W m^{-2}. As seen in Fig. 5.1b, the large variability of the heating/cooling in total trends in heating is again largely due to the competition between horizontal and vertical advection.

The net warming over the studied year (1.40 × 10^{9}J m^{-2}) occurs at the rate of 45 W m^{-2}. This warming rate can be linked to heating by surface forcing (67 W m^{-2}) and vertical advection (163 W m^{-2}), which add up to offset the heat removed by horizontal advection (82 W m^{-2}). Contribution of vertical diffusion over the 0–250 m layer is small compared with the other terms: its value is two order of magnitude less than that of the other process. This process redistributes heat and its integrated contribution corresponds to small losses through the bottom.

In summary, horizontal advection is responsible for net cooling of the simulated surface layer, whereas vertical advection and surface forcing fluxes are both responsible for net warming. Local forcing is always important, but is dominant only during the Spring inter-monsoon. The SW monsoon is the period of highest heat content variation, and most of the heat gained through the air-sea interface over the year is evacuated at that time.

5.2 Reynolds-based budget (S3c)

The contributions of different processes to total (integrated) trend over the ML and over the whole simulated (0–250 m) layer throughout the year are presented in Fig. 5.2(a&b). In the ML, the important processes are horizontal advection, vertical diffusion, and local surface fluxes. Vertical advection plays a minor role. In contrast, when the entire 0–250 m layer is considered, vertical advection is important and often more important than horizontal advection; surface forcing plays a smaller role and contribution of vertical diffusion is smallest. It is also worth noting that all terms

vary with significant amplitudes at the scale of a few days to a few weeks. The net contribution of the four processes to the heat budget variations of the 0–250 m layer and of the 0–50 m layer were integrated over the four characteristic periods and for the whole year. The results are presented in Table 5.3 and Table 5.4.
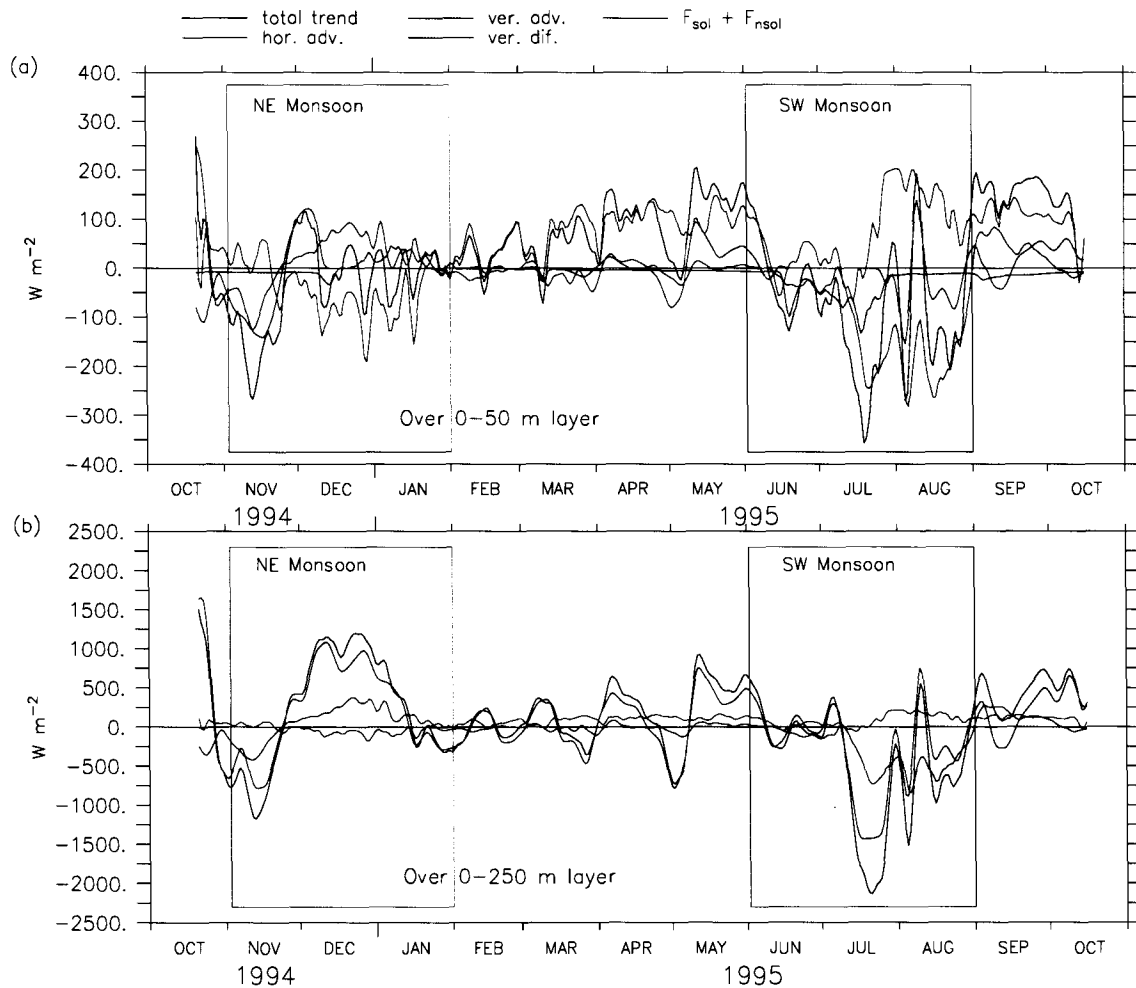
Figure 5.2: (a) The contribution of different processes to the total temperature trend for the 0–50 m layer (in units of heat flux) of the S3 simulation: horizontal advection (red line); vertical advection (green line); vertical diffusion (blue line); combined local surface fluxes and fluxes due to penetrating solar radiation (cyan line) in . (b) same as (a), but for the 0–250 m layer.

5.2.1 Budget analysis for the 0–50 m layer

During the NE monsoon, the near-surface layer undergoes a net cooling of 3.28×10^8 J m^{-2} at the rate of 41 W m^{-2} (Table 5.3). This cooling results from the excess of heat loss through air-sea fluxes at the rate of 42 W m^{-2} and vertical advection at the rate of 13 W m^{-2} over the heating effect of horizontal advection at the rate of 11 W m^{-2} and of vertical diffusion at the rate of 3 W m^{-2}. As shown in Fig. 5.2a, these four contributions vary significantly during this period. Vertical advection contributes significantly to the total trend only during early NE monsoon (mid-November to mid-December). During the rest of the NE monsoon, the total trend essentially results from comparable contributions from local surface fluxes, horizontal advection, and vertical diffusion.

Over the Spring IM, the near-surface layer gains 7.45×10^8 J m^{-2} at the rate of 71 W m^{-2}. This positive heating rate results mainly from the dominating heating effects of local air-sea fluxes (78 W m^{-2}) and from relatively very small contributions of other processes. As seen in Fig. 5.2a, most of the variability of the near-surface layer is dominated by local air-sea fluxes, whereas the remaining processes compensate each other.

The SW monsoon net cooling (7.1×10^8 J m^{-2}) of the near surface layer is achieved at the rate of 89 W m^{-2}. This cooling results from dominating cooling effects of horizontal advection at the rate of 107 W m^{-2}, and from the relatively smaller contribution of vertical diffusion at the rate of 34 W m^{-2}, and of vertical advection at the rate of 22 W m^{-2} over opposing surface heating at the rate of 73 W m^{-2}. The variability is at its highest for the four processes during this period (Fig 5.2a).

The Autumn IM net warming (2.72×10^8 J m^{-2}) results at the rate of 68 W m^{-2}, with positive contributions from surface fluxes at the rate of 101 W m^{-2} and from horizontal advection at the rate of 32 W m^{-2}; these processes which dominated over cooling effects from vertical advection at the rate of 51 W m^{-2} and vertical diffusion at the rate of 13 W m^{-2}. During this period (similar to the Spring IM), local air-sea fluxes mostly control the variability (Fig. 5.2a).

The net warming over the studied year (1.27×10^8 J m^{-2}) is achieved at the rate of 15 W m^{-2}. This warming results from the positive input by surface forcing at the rate of 48 W m^{-2}, which offsets the heat removed by horizontal advection at the rate of 24 W m^{-2}, by vertical diffusion at the rate of 11 W m^{-2}, and by vertical advection at the rate of 9 W m^{-2}.

Table 5.3: Average and integrated heat content variation of the 0–50 m layer for simulation S3c (in W m^{-2} and J m^{-2}) during four characteristic periods of the year during 20 October 1994 to 17 October 1995 are presented.

Rate of heat content variation Period	Resultant W m^{-2} (J m^{-2})	Local surface fluxes W m^{-2} (J m^{-2})	Horizontal advection W m^{-2} (J m^{-2})	Vertical advection W m^{-2} (J m^{-2})	Vertical diffusion W m^{-2} (J m^{-2})
NE Monsoon 1-Nov.-94 :31-Jan.-95	-41.26 (-3.28×10^8)	-41.62 (-3.31×10^8)	$+10.82$ $(+0.86 \times 10^8)$	-13.20 (-1.05×10^8)	$+2.73$ (0.22×10^8)
Spring IM 1-Feb.-95:31-May-95	$+70.73$ $(+7.45 \times 10^8)$	$+77.72$ $(+8.19 \times 10^8)$	-5.69 (-0.63×10^8)	$+3.16$ $(+0.33 \times 10^8)$	-4.14 (-0.44×10^8)
SW Monsoon 1-Jun-95:31-Aug.-95	-89.00 (-7.1×10^8)	$+73.19$ $(+5.82 \times 10^8)$	-106.6 (-8.47×10^8)	-21.55 (-1.71×10^8)	-34.06 (-2.71×10^8)
Autumn IM 1-Sep.-95:16-Oct-95	$+68.5$ $(+2.72 \times 10^8)$	$+100.6$ $(+4.00 \times 10^8)$	$+31.6$ $(+1.26 \times 10^8)$	-50.77 (-2.02×10^8)	-12.99 (-0.52×10^8)
Whole Year 20-Oct-94:16-Oct-95	$+4.04$ $(+1.268 \times 10^8)$	$+48.31$ $(+1.52 \times 10^9)$	-24.36 (-7.64×10^8)	-8.66 (-2.72×10^8)	-11.24 (-3.53×10^8)

Table 5.4: Average and integrated heat content variation of the 0–250 m layer for simulation S3c (in W m^{-2} and J m^{-2}) during four characteristic periods of the year during 20 October 1994 to 17 October 1995 are presented.

Rate of heat content variation Period	Resultant W m^{-2} (J m^{-2})	Local surface fluxes W m^{-2} (J m^{-2})	Horizontal advection W m^{-2} (J m^{-2})	Vertical advection W m^{-2} (J m^{-2})	Vertical diffusion W m^{-2} (J m^{-2})
NE Monsoon 1-Nov.-94:31-Jan.-95	+127.7 ($+1.01 \times 10^9$)	−41.62 (-3.31×10^8)	+55.9 ($+4.44 \times 10^8$)	+114.8 ($+9.12 \times 10^8$)	−1.3 (-1.06×10^7)
Spring IM 1-Feb.-95:31-May-95	+124.9 ($+1.32 \times 10^9$)	+100.0 ($+1.05 \times 10^9$)	−9.07 (-9.56×10^7)	+36.35 ($+3.83 \times 10^8$)	−1.75 (-1.84×10^7)
SW Monsoon 1-Jun-95:31-Aug.-95	−388.4 (-3.09×10^9)	+89.9 ($+7.15 \times 10^8$)	−292.1 (-2.32×10^9)	−185.1 (-1.47×10^9)	−1.2 (-0.9×10^7)
Autumn IM 1-Sep.-95:16-Oct-95	+311.5 ($+1.24 \times 10^9$)	+119.0 ($+4.72 \times 10^8$)	+108.9 ($+4.33 \times 10^8$)	+84.39 ($+3.35 \times 10^8$)	−0.72 (-0.2×10^7)
Whole Year 20-Oct-94:16-Oct-95	+57.3 ($+1.80 \times 10^9$)	+67.31 ($+2.11 \times 10^9$)	−56.1 (-1.76×10^9)	+47.35 ($+1.48 \times 10^9$)	−1.36 (-4.27×10^7)

5.2.2 Budget analysis for 0–250 m layer

As regards the whole simulated layer (Table 5.4), the NE monsoon net warming (1.01×10^9 J m^{-2}) occurs at the rate of 128 W m^{-2}. This rate of warming is largely due to vertical advection (115 W m^{-2}) and to horizontal advection (56 W m^{-2}), with relatively small losses through the air-sea interface (42 W m^{-2}). As shown in Fig. 5.2b, the variation of horizontal and vertical advection during this period is significant.

The spring IM net warming (1.32×10^9 J m^{-2}) is achieved at the rate of 125 W m^{-2}. This warming rate is largely due to heating through the surface (100 W m^{-2}) and to vertical advection (37 W m^{-2}), with negligible cooling effects from horizontal advection and vertical diffusion. Figure 5.2b shows that vertical advection is mostly responsible for the variability in the total trend during this period.

The SW monsoon net cooling (3.1×10^9 J m^{-2}) is achieved at the rate of (388 W m^{-2}). This cooling results mainly from high heat removal by horizontal advection at the rate of (292 W m^{-2}) and by vertical advection at the rate of (185 W m^{-2}). At this time, there is a relatively small positive influx through the surface (90 W m^{-2}). During this period, horizontal and vertical advection undergo high and similar variations (Fig. 5.2b).

The Autumn IM net warming (1.24×10^9 J m^{-2}) is achieved at the rate of 311 W m^{-2}. This warming results mainly from heating by surface forcing at the average rate of 119 W m^{-2}, horizontal advection at the average rate of 108 W m^{-2}, and vertical advection at the average rate of 84 W m^{-2}. As seen in Fig. 5.2b, the large variability of the heating/cooling in total trends in heating is again largely due to vertical advection.

The net warming over the studied year (2.92×10^9 J m^{-2}) occurs at the rate of 93 W m^{-2}. This warming rate can be linked to heating by vertical advection (162 W m^{-2}), and surface forcing (67 W m^{-2}), which add up to offset the heat removed by horizontal advection (136 W m^{-2}). Contribution of vertical diffusion over the 0–250 m layer is small compared with the other terms: its value is one order of magnitude less than that of the other process. This process redistributes heat and its integrated contribution corresponds to small losses through the bottom.

In summary, horizontal advection is responsible for net cooling of the simulated surface layer, whereas vertical advection and surface forcing fluxes are both responsible for net warming. Local forcing is always important, but is dominant only during the Spring inter-monsoon. The SW monsoon is the period of highest heat content variation, and most of the heat gained through the air-sea interface over the year is evacuated at that time.

5.3 Comparison between Fischer-based and Reynolds-based budgets

Figures 5.3 and 5.4 present the heat budget based on S2c and S3c together with 2 other concurrent simulations: S2c* and S3b. S2c* was carried out in place of S2c simulation to improve on the S2c simulation in section 4.2.1.1 by assigning zero fluxes to the Fischer-based horizontal advective heat fluxes within the ML during the early NE monsoon (20 October to mid–November). S3b is similar to S3c, excepted that the SODA vertical velocity was used instead of the predicted (from Reynolds-based horizontal advective heat fluxes) vertical velocity.

5.3.1 0–50 m layer

The predicted net cooling over 0–50 m layer in S2c is 3 times larger than the cooling present in observations, whereas the predicted cooling in S3c is 20% smaller than the observations. In S2c simulation, horizontal advection drives a large cooling and vertical diffusion drives a large heating in the surface layer. In contrast, horizontal advection drives heating and vertical diffusion drives negligible heating in the S3c surface layer budget. The contribution of horizontal advection is relatively small in S2c* simulation as compared with S2c simulation, and contribution due to vertical diffusion in S2c* is almost the same as in S2c. The contributions of various processes in S3b and S3c are similar.

During the SW monsoon, the dominating role of horizontal advection in cooling the surface layer over the heating effects from the atmospheric fluxes is shown by all the simulations.

The dominating role of atmospheric fluxes in heating the surface layer is depicted from all the four simulations during the Spring and Autumn IM. The total heat content variation in both S2c and S3c during the SW monsoon and during the IMs are almost the same as in the observations.

Regarding the whole year, S3c and S3b suggest that the net heating of the surface layer is dominated by atmospheric fluxes over cooling caused by horizontal advection and vertical diffusion with small contribution from vertical advection. The predicted heating in S3c is almost equal to the heating present in the observations. In contrast, the S2c simulation suggests that the near-surface layer undergoes large cooling (instead of the warming present in observation) owing to excess cooling due to horizontal advection, which dominates the comparable warming caused by vertical advection and atmospheric fluxes. The large biasing during the NE monsoon in S2c simulation affects the whole year.

5.3.2 0–250 m layer

In all four simulations S2c, S2c*, S3c, and S3b, the total budget for (0–250 m) layer during the NE monsoon is positive (warming) mainly due to the dominating effect of vertical advection; however, the amplitude of variation of vertical advection differs in different simulations due to the different contributions from horizontal advection (see Fig. 5.4). In S2c (S2c*) simulation vertical advection causes large warming, which dominates the large cooling caused by horizontal advection. In contrast, vertical advection and horizontal advection both cause warming in S3c (S3b) simulation, and their amplitudes are relatively much smaller than the corresponding contributions in S2c.

During the Spring IM, all the four simulations suggest that atmospheric fluxes and vertical advection together play a role in heating the 0–250 m layer. In S3c (S3b), the contribution of vertical

advection is relatively smaller than atmospheric fluxes. The contribution of vertical advection is larger than atmospheric fluxes in S2c (S2c*).

The SW monsoon cooling of the layer comes from both horizontal and vertical advection in S2c simulation. In contrast, the cooling effect of horizontal advection dominates the heating effect of vertical advection in S3c simulation.

During the Autumn IM, all the four simulations suggest that atmospheric fluxes and horizontal advection together play a role in heating the layer. The role of vertical advection is negligible in S2c, in contrast to the comparable horizontal advection contribution of vertical advection in S3c.

Regarding the whole year, both simulations suggest that the net heating of the layer comes from comparable contributions from horizontal advection, vertical advection, and atmospheric fluxes. In S2c, contributions of vertical advection and horizontal advection are larger than the corresponding contributions in S3c simulation.
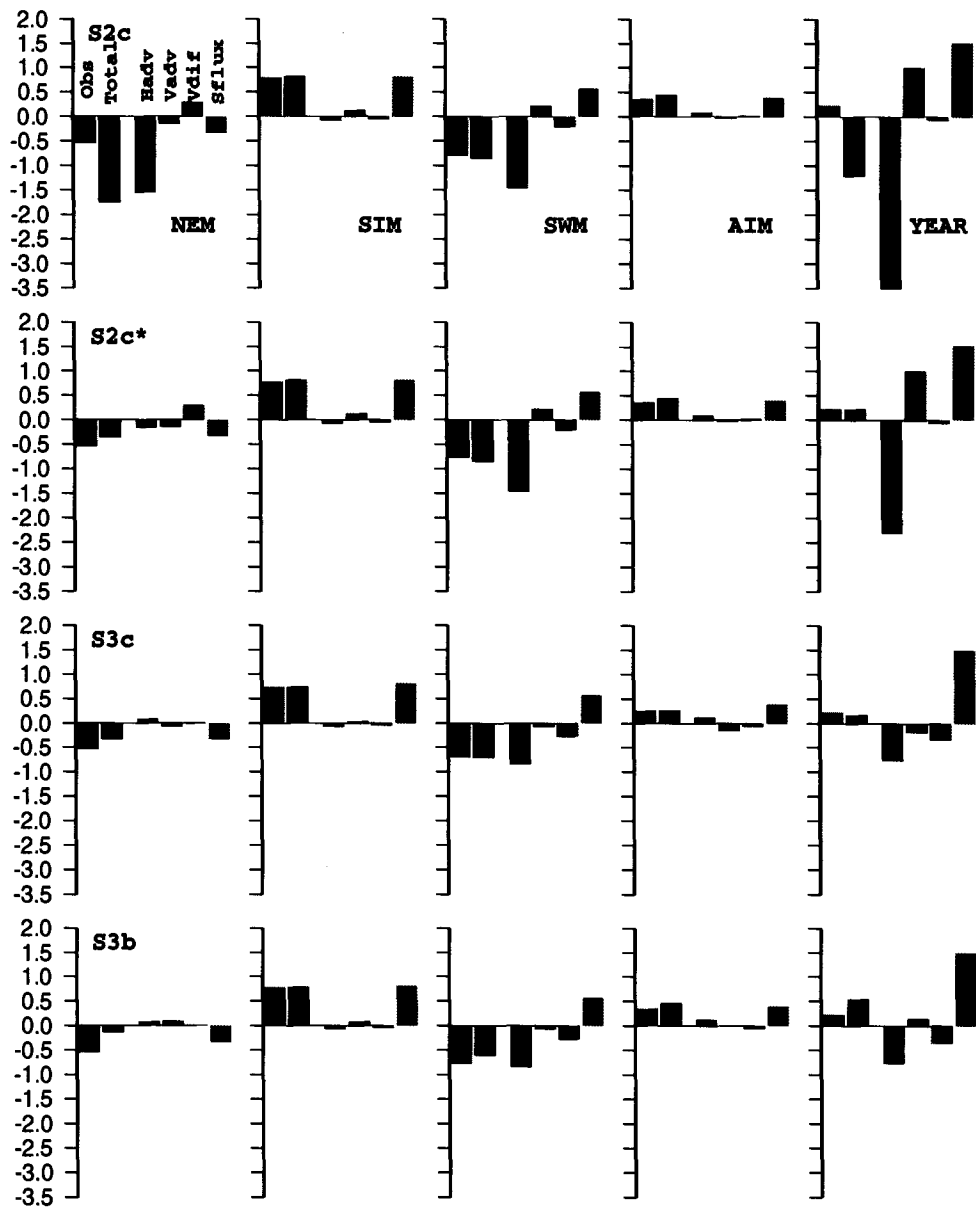
Figure 5.3: Barplots showing the contribution of various heat budget terms for the near–surface (0–50 m) layer: horizontal advection (magenta), vertical advection (blue), vertical diffusion (cyan), and surface heat flux (green) in the net heat content (black).The total predicted (black) and observed (grey) heat content variations of different monsoon periods also presented. Along the vertical the values are: $X \times 10^9 \, \mathrm{J \, m^{-2}}$. The upper panel: S2c simulation, 2nd panel: S2c* simulation, 3rd panel: S3c simulation, and lower panel: S3b simulation.
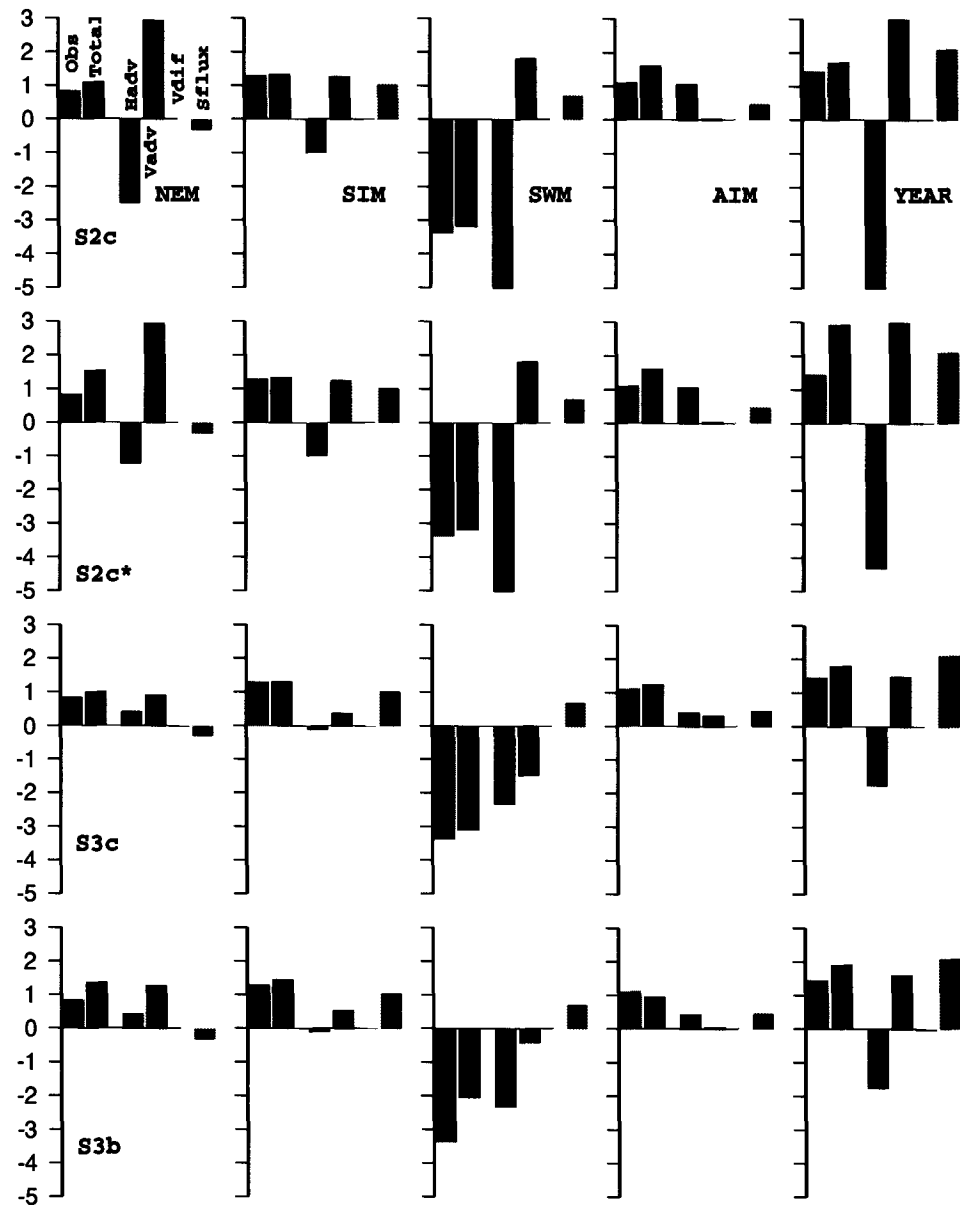
Figure 5.4: Barplots showing the contribution of various heat budget terms for the whole (0–250 m) layer: horizontal advection (magenta), vertical advection (blue), vertical diffusion (cyan), and surface heat flux (green) in the net heat content (black).The total predicted (black) and observed (grey) heat content variations of different monsoon periods also presented. Along the vertical the values are: $X \times 10^9$J m^{-2}. The upper panel: S2c simulation, 2nd panel: S2c* simulation, 3rd panel: S3c simulation, and lower panel: S3b simulation.

5.4 Concluding remarks

The contribution of vertical diffusion during the NE monsoon in S2c simulation is large and positive in 0–50m layer budget and almost equal to that of the atmospheric fluxes. This large and positive contribution of vertical diffusion seems to be suspicious. The analysis of the predicted profiles of diffusive heat fluxes suggest that the large values of the flux result from the strong cooling induced by Fischer-based horizontal advection within the mixed layer during November–December.

The results of heat budget analysis based on S3b (SODA-based) simulation are almost similar to the results of the analysis based on S3c simulations.

In most of the cases, the above heat budget analyses for S2c and S3c simulations lead to different inferences. This is because of the fact that the heat fluxes due to vertical advection used for the heat budget analysis are dependent on magnitudes of horizontal advective heat fluxes (as they were calculated as the residual terms of the model heat budget). Although it is difficult to arrive any independent conclusion about the relative contributions of horizontal and vertical advection, it can be believed that both the processes are important throughout the year.

For the near surface (0–50 m) layer, some important conclusions can be derived. During IMs, atmospheric fluxes are the dominating processes and during the NE and SW monsoons, all processes are important. The horizontal advection is the most dominating process during the SW monsoon.

The contributions of various heat budget terms in simulation S2c (S2c*) exhibited large amplitudes during both the monsoon periods and it is difficult to believe that they are realistic. As already described in section 4.2.4, the resultant predicted vertical velocity (and hence vertical advection) that is used in S2c simulation is largely sensitive to a 50% change in the Fischer-based horizontal advection during the SW and NE monsoons. In contrast, the predicted vertical velocity that is used in S3c simulation remains unchanged with respect to a 50 % change in Reynolds-based advective heat flux estimates. Hence, we infer that, owing to the uncertainty associated with Fischer-based estimates, the actual heat fluxes due to horizontal advection must be much weaker than in Fischer-based estimates. If this is so, the heat budget based on S3c simulation is the most representative of the location of the mooring array.

Chapter 6

Summary

To examine the role of various intervening processes in controlling the upper ocean thermal structure in the central Arabian Sea, a 1-D mixed-layer model based on turbulent closure scheme is forced by atmospheric fluxes and advective heat fluxes over the one-year period of the JGOFS time-series starting from mid-October 1994 in the central Arabian Sea at (61.5°E & 15.5°N). Atmospheric forcing data are available from the moored array observations (Weller et al. [2]). The horizontal advective contributions at the study location are available from two different sources. The first estimate is based on local *in situ* measurements (as earlier estimated by Fischer et al. [4]). The second estimate is based on optimally interpolated satellite SST field and *in situ* currents. The vertical velocity, as in all oceanography problem, poses a challenge. Two possible approaches have been considered for the diagnostic analysis. In the first approach, the model was used to predict the temperature profile (using atmospheric fluxes and estimates of horizontal and vertical advection). In the second approach, the observed temperature profiles (and atmospheric fluxes and estimates of horizontal advection) were used to force the model in order to predict the vertical velocity.

Besides the main experiments carried out using the above two approaches, additional experiments were also performed mainly for two purposes: (i) to support the analysis of the results obtained from the main experiments, and (ii) to examine the role of auxiliary parameters (salinity and biomass) in the seasonal evolution of upper-ocean temperature. Finally, model-based heat-budget analysis for the four monsoon seasons: winter, spring, summer, and autumn has been carried out. The following are the three important conclusions of the thesis.

(1) Vertical advection is an important process, as important as atmospheric fluxes and horizontal advection, throughout the year in controlling the upper ocean thermal structure and the heat budget of the central Arabian Sea.

(2) The general trends of ML deepening and SST cooling in the central Arabian Sea during the NE monsoon are due to buoyancy driven convective entrainment mixing, whereas the trends of ML deepening and SST cooling during the SW monsoon are due to both wind driven mixing and buoyancy driven convective mixing. However, the observed trends of ML and SST during the whole year can only be reproduced when all the intervening process are accounted for: advection together with atmospheric fluxes.

(3) Ocean dynamics plays a primary role in controlling the thermodynamics of the upper ocean in the central Arabian Sea, whereas salinity and phytoplankton biomass concentration evolution do not have a significant local control over the thermal structure.

(4) Some results of the present study have their validity limited by the uncertainties in Fischer-based horizontal advective heat fluxes. The deployment of a four/five mooring system to quantify the contributions of horizontal variability is believed not to be satisfactory as far as quantitative estimation is concerned. The information obtained from the central mooring in combination with satellite altimeter imagery proves to be at least as good, and may be better.

At the end of this thesis, we do not know whether the conclusions obtained for the central Arabian Sea are still valid in other parts of the Arabian Sea. This issue still remains an open question. This can be answered by achieving similar model-based diagnostic studies or by carrying out a basin scale study using a 3D model.

This model can be used for studies similar to those presented in this thesis to understand the eastern and southeastern Arabian Sea, where time-series observation were carried out during the Arabian Sea Monsoon Experiment (ARMEX) during 2002–2003.

Thermodynamics of the ocean influences the biogeochemical system of the ocean environment. Another perspective is to couple a biogeochemical model to an upper ocean thermodynamical model to perform a simulation of carbon and nitrogen fluxes along an annual cycle in the central Arabian Sea.

Appendix A

Equation of state for sea water

UNESCO formula (Millero and Poisson [121]) for density of sea water:

$$\rho = \rho_0 + A \cdot S + B \cdot S^{3/2} + C \cdot S^2 \qquad \text{(A.1)}$$

$$A = 8.24493 \times 10^{-1} - 4.0899 \times 10^{-3}T + 7.6438 \times 10^{-5}T^2$$
$$- 8.2467 \times 10^{-7}T^3 + 5.3875 \times 10^{-9}T^4 \quad \text{(A.2)}$$

$$B = -5.72466 \times 10^{-3} + 1.0227 \times 10^{-4}T - 1.6546 \times 10^{-6}T^2 \qquad \text{(A.3)}$$

$$C = 4.8314 \times 10^{-4} \qquad \text{(A.4)}$$

$$\rho_0 = 999.842594 + 6.793952 \times 10^{-2}T - 9.095290 \times 10^{-3}T^2 + 1.001685 \times 10^{-4}T^3$$
$$- 1.120083 \times 10^{-6}T^4 + 6.536332 \times 10^{-9}T^5 \quad \text{(A.5)}$$

Where T is in Deg C, S is in psu, and ρ_0 and ρ are in Kg/m^3.

Appendix B

Results of the auxiliary experiments

The experiments carried out in Chapter 4 to predict the upper ocean thermal structure in the central Arabian Sea, did not consider salinity variations. The inaccuracy in the predicted salinity may affect the results. The effect of salinity will be examined below in section B.1 by forcing the model with *in situ* salinity measurements.

Similarly, the attenuation of solar light in the main experiments corresponds to a constant clear oceanic water type-I (Jerlov [102]). The effect of a varying chlorophyll profile will be examined in section B.2, by forcing the model with *in situ* measurements using a spectral light attenuation scheme.

In all the experiments achieved (Chapter 4), the atmospheric forcing fluxes from the JGOFS mooring were used. How does the mixed layer respond to the individual forcing fluxes? These response will be examined in section B.3.

B.1 Impact of salinity

Salinity plays potential role in controlling the temperature structure by affecting the density field. The numerical experiments carried out in Chapter 4 did not account for the impact of salinity. The governing equation of the salt balance did not include the impact of advective processes (due to lack of data). As a consequence the predicted salinity structure differs significantly from the observed value (see Fig. B.1). At the surface, the differences between the observed and predicted salinity are large during the SW monsoon (upto 0.8 psu). In sub-surface the differences are large during January to mid-July (upto -0.8 psu).

To examine the role of salinity on the temperature structure, two simulations similar to S3c are carried out. The first simulation (S3Sa) is carried out by prescribing to the model a constant

93
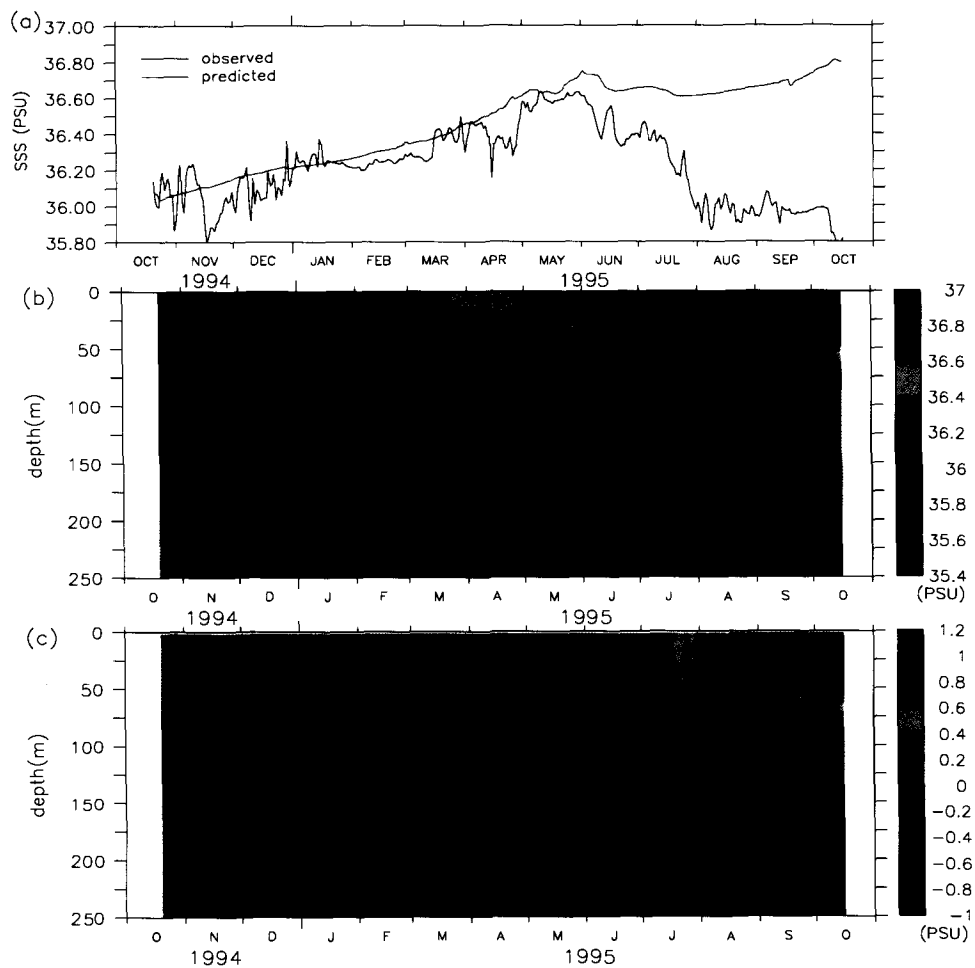
Figure B.1: Results of the simulation S1: (a) Sea Surface Salinity (SSS) (red) is compared with the observed SSS (black), (b) vertical structure of predicted salinity, (c) modeled minus observed salinity.

salinity (37 psu) and the second simulation (S3Sb) is carried out by prescribing to the model the observed salinity field. The results of both simulations are presented in the Fig. B.2. The figures show that the simulations are mostly identical, which implies that the salinity variation has a secondary role in controlling the upper ocean thermal structure in the central Arabian Sea.
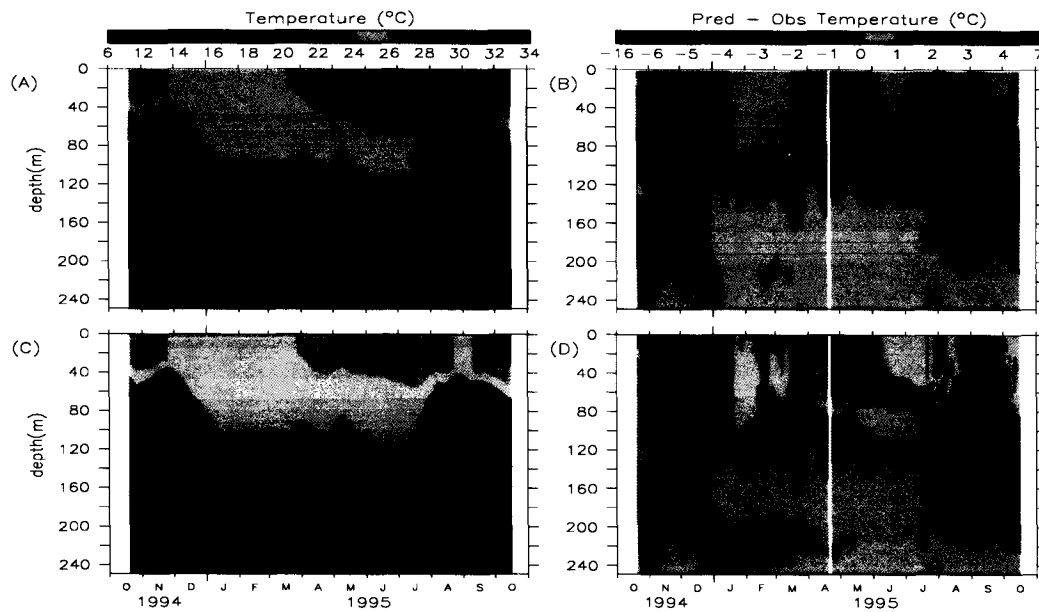
Figure B.2: Result of sensitivity experiments examining the effect of salinity on the upper ocean thermal structure in the central Arabian sea: (A) simulated temperature field when the TKE model is forced with constant salinity (39 psu); (B) same as (A), but for difference between predicted and observed temperature filed; (C) simulated temperature field when the TKE model is forced with observed salinity filed; (D) same as (C), but for difference between predicted and observed temperature field.

B.2   Impact of biomass

Biomass (chlorophyll concentration) influences the thermal structure. The process responsible is the vertical attenuation of solar irradiance. To examine the impact of chlorophyll, a spectrally resolved bio-optical model of solar irradiance $I(z)$ (Appendix-C.3) was selected and embedded in the mixed-layer model in place of the default double exponential function of $I(z)$ (see Eqn. 3.21). Simulations similar to simulation S1 (section 4.1.1) are carried out as follows. In the first simulation (S1a) the bio-optical model is forced with observed chlorophyll profiles (presented in the Fig. 3.7). In the second simulation (S1b) the model is forced with a low and constant uniform chlorophyll concentration of 0.1 mg m^{-3}. In the third simulation (S1c), the model is forced with a relatively high constant uniform chlorophyll concentration of 0.5 mg m^{-3}. The fourth simulation (S1w) is carried out for the case of pure oceanic water with zero chlorophyll concentration. The results of these simulations are compared with the results from the simulation S1 (achieved in the chapter 4.1.1 for the case of Jerlov's water type-I) in the Fig. B.3.

(a)

Rate of change of SST ($^\circ$C month^{-1})

4.0
2.0
0.0
-2.0
-4.0

S1
S1a
S1b
S1c

OCT   NOV   DEC   JAN   FEB   MAR   APR   MAY   JUN   JUL   AUG   SEP   OCT
      1994   1995

(b)

MLD (m)

0.
-10.
-20.
-30.
-40.
-50.

OCT   NOV   DEC   JAN   FEB   MAR   APR   MAY   JUN   JUL   AUG   SEP   OCT
      1994   1995
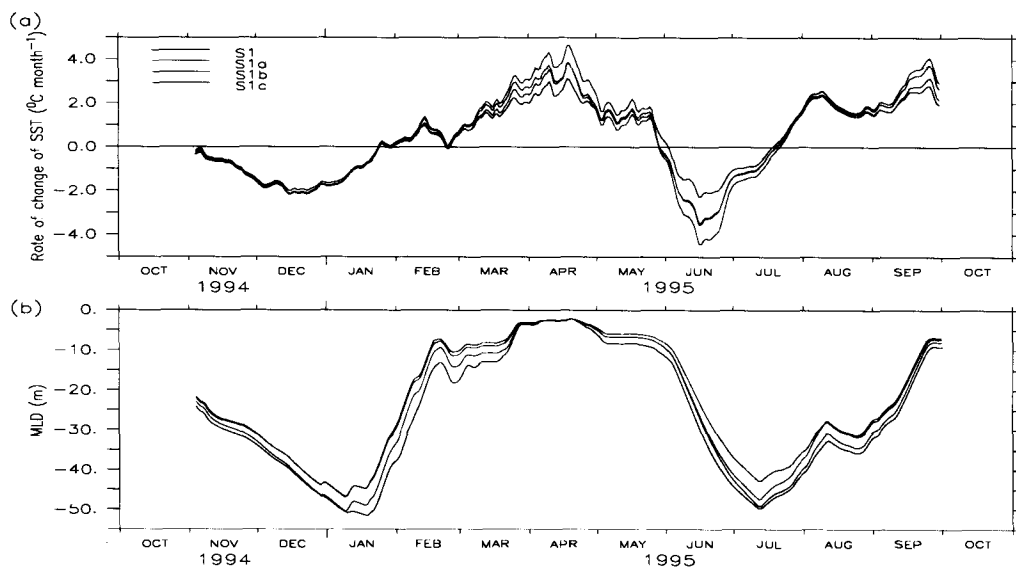
Figure B.3: Comparing between the results from simulations S1, S1a, S2b, and S2c to see the impact of biomass variation on the upper ocean thermal structure in the central Arabian sea. (a) The rate of change of predicted SST and (b) the predicted MLD. Data are smoothed in the figure with one month low pass filter.

The rate of change of predicted SST (Fig. B.3a) and predicted MLD (Fig. B.3b) of the simulations S1a, S1b, and S1c parallel the simulation S1. The difference between the rate of change of predicted SST among various simulations are upto 1°C month^{-1} during April, upto 2 $^\circ$C month^{-1}during June, and upto 1 $^\circ$C month^{-1} during September to early October and the difference is small (0.5°C month^{-1}) during remaining period of the year. The difference between the predicted MLD among the various simulations are upto 8 m during the year except April when the differences are negligible.

Among all the simulations: S1a, S1b, and S1c, S1b (based on 0.1 mg m^{-3}) is the nearest to the simulation S1 (based on Jerlov water type-I). Differences between the rate of change of SST of the two simulations (S1 and S1b) are upto 1°C month^{-1} only during June and relatively small during remaining period of the year. Differences between the MLD of the two simulations are upto 4 m only. Similarly, the simulation S1a (corresponding to observed chlorophyll concentration) is nearest to the simulation S1c (corresponding to large chlorophyll concentration: 0.5 mg m^{-3}) during most of the period of the year except during June when S1a almost coincides with S1b (corresponding to low chlorophyll concentration: 0.1 mg m^{-3}). It is worth noting that observed chlorophyll concentration is less than 0.3 mg m^{-3} during the early half of June.

The difference of the simulations S1b (case of low chlorophyll concentration: 0.1 mg m^{-3})
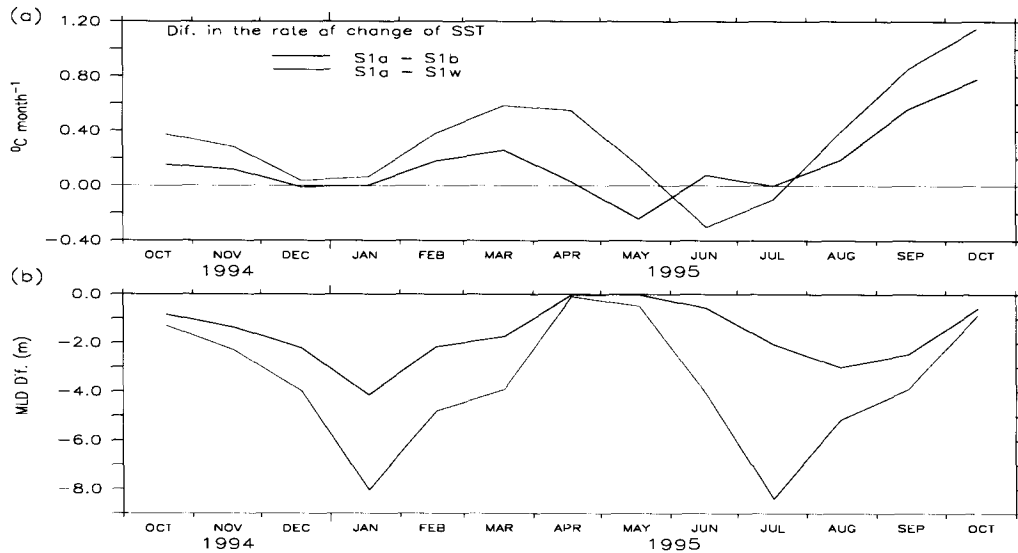
Figure B.4: The difference of the simulations S1b and S1w from the simulation S2b: (a) difference between the rate of change of the predicted SSTs and (b) difference between the predicted MLDs.

and S1w (for pure oceanic water i.e., zero chlorophyll concentration) from the simulation S1a (the case of observed chlorophyll concentration) are presented in Fig. B.4.

The difference of the simulation S1b from the simulations S1a (see Fig. B.4) indicates that the mixed layer depth (MLD) lowers by 4 m during the NE monsoon, and 3 m during the SW monsoon when the role of chlorophyll is accounted for, compared to the situation of a constant low chlorophyll (0.1 mg m^{-3}) water. During both these periods the impact on the sea surface temperature (SST) is less than 0.2 ^{0}C month^{-1}. During the spring inter-monsoon the mixed layer is shallow (MLD $\leq$ 20 m), and the impact of chlorophyll on SST is also less than 0.2 ^{0}C month^{-1}. In contrast, during the Autumn inter-monsoon the mixed layer is also shallow, but the impact of chlorophyll concentration in SST is relatively large: 0.5 ^{0}C month^{-1}. Although it seems that local impact of chlorophyll variation in the mixed layer thermodynamics is relatively large during the Autumn inter-monsoon compared to the rest of the period of the year, the impact is not significant unlike the earlier studies by Sathyendranath et al. [36] who reported biological (chlorophyll variation) heating is almost 4 ^{0}C month^{-1} during the month of August in the Arabian Sea, however, their study location was different than our study location. This result can be compared to the study carried out by Babu et al. [112] at the same study location. Unlike their study, our study shows only 2 m deepening of the ML during the month of August (which is only 3 % of the observed MLD) and its impact in SST change is less only .4 ^{0}C month^{-1} in contrast to their conclusion that biological heating impact is significantly strong during this period. The results of our study differ

from their study due to following reasons. (1) The air-sea fluxes (in particular Solar Radiation) we used are based on *in situ* measurements versus their climatological data, (2) the chlorophyll data used to force the model in our study is based on *in situ* measurements versus their climatological counter part, (3) the bio-optical model used in the present study is spectrally resolved versus their non-spectral model.

The difference of the simulation S1w from the simulations S1a (see Fig. B.4) indicates that the mixed layer depth (MLD) lowers by 8 m during the NE monsoon, and during the SW monsoon when the role of chlorophyll is accounted for, compared to a constant clear water situation. During both these periods the impact on the sea surface temperature (SST) is insignificant: less than 0.3 ^0C month^{-1}. In contrast, during the spring inter-monsoon, the mixed layer is shallow (MLD $\leq$ 20 m), and the impact of chlorophyll on SST is relatively large: 0.5 ^0C month^{-1}. The biological heating impact with respect to the clear-water condition is relatively larger than the impact with respect to constant low background chlorophyll concentration, however, our interest is to asses the impact of seasonal variation of chlorophyll concentration in controlling the upper ocean thermal structure at work.

When the impact of chlorophyll variation on SST is compared to the impact of advective processes[1] (see Fig. B.5), it turns out that the impact of chlorophyll variation is negligible during both the monsoons, whereas these two impacts have similar amplitude during the spring and Autumn inter-monsoons. Similarly the impact of chlorophyll variation on the MLD is negligible (is only 5%) as compared with the impact of advective processes. On the whole, in spite of a 20 fold variation in chlorophyll concentration (0.1 - 2.0 mg m^{-3}, see the Fig. 3.7), its local impact on the 1D physical structure can be neglected.

---

[1]Note: The heating impact due to advective processes are calculated using S2d, and S1 simulations following the same procedure as done for the impact of chlorophyll in S1a and S1b simulations.
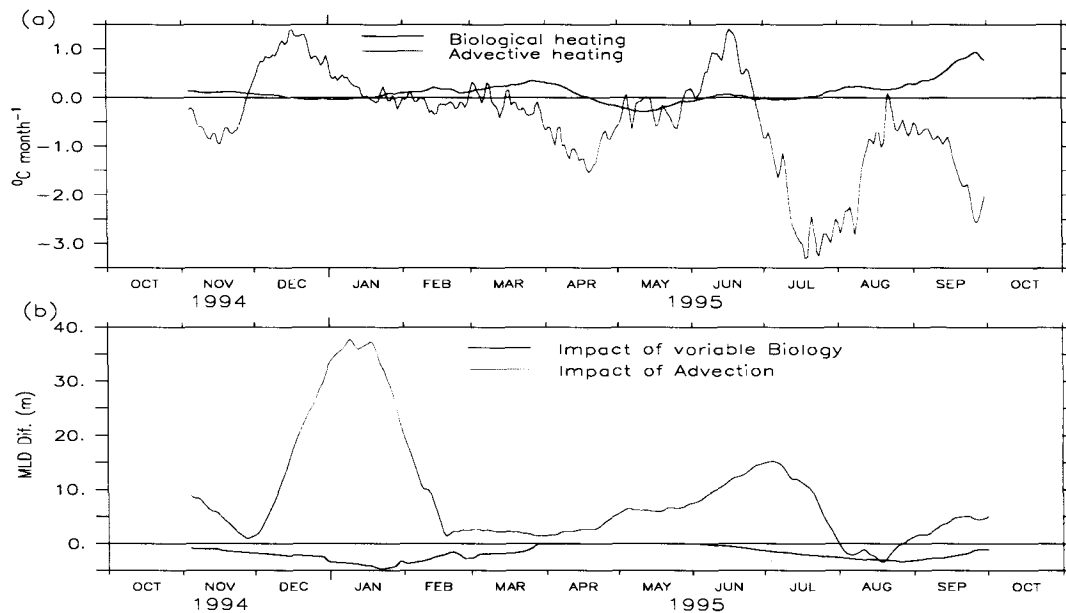
Figure B.5: A comparison between the biological heating effect and advective heating effect contributed to the observed temperature structure at the study location.

B.3 Model sensitivity to the air-sea fluxes

The surface forcing fluxes used in the model were computed from the measurements at the mooring (Weller et al. [2]) at high resolution. It is interesting to know, how sensitive are the model results to the surface forcing fluxes. This issue is now examined by varying arbitrarily the surface forcing fluxes.

B.3.1 ML sensitivity to wind-stress

Two simulations are carried out by forcing the model with modified surface fluxes. The first considers a 10% increase in the wind stress (S1Wa) and the second a 10% decrease in the wind stress (S1Wb). The results of this simulations are compared with the results of the simulation S1 in Fig. B.6. As shown, the deepening of the ML and cooling of the SST enhances with the increase in wind stress. The ML deepening and the SST cooling are different in different periods of the year depending on the strength of the wind stress. Thus, the ML deepening and the SST cooling responding to a 10% increase in the wind stress is not significant (change in SST is less than 0.1 ^{0}C and change in MLD is 1m) during the NE monsoon (period of weak wind) and during the Spring IM (period of moderate wind) excepted for a few occasions of higher deepening of the ML
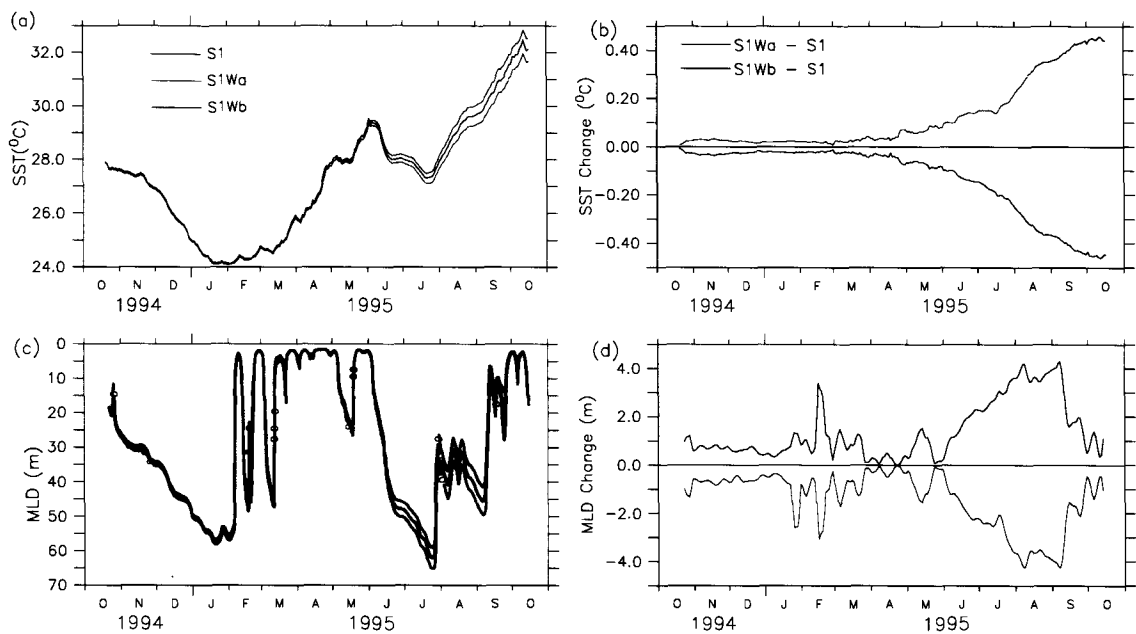
Figure B.6: Results of the sensitivity experiments corresponding to change in the strength of wind stress: S1, the case of exact wind stress; S1Wa, the case of increase in the wind stress by 10%; S1Wb, the case of decrease in wind-stress by 10%.

(3m). The impact of 10% change of wind stress in ML is significant during the SW monsoon (the period of strong wind stress). During this period, the deepening of the ML enhances upto 5m and the cooling of SST enhances upto .5 ^{0}C. The results are exactly symmetric when the experiment is carried out for a 10% decrease in the strength of wind stress. When all these simulations are compared with the observation, the results of the simulation S1 are the best.

In summary, the SST and the MLD predicted by the model for the cases of 10 % increase and decrease in the strength of observed wind field do not differ significantly throughout the year.

B.3.2 ML sensitivity to surface heat fluxes

Solar heat flux

Two simulations of temperature structure are carried out (similar to the S1 experiment) by changing only the solar heat fluxes by 10% keeping the remaining fluxes unchanged. The first simulation (S1Sa) is based on a 10% increase in the solar radiation, and the second simulation (S1Sb) is based on a 10% decrease in solar radiation. The results of the simulations are compared with the results

of the simulation S1 for the case of the exact surface fluxes in the Fig. B.7. The predicted SST and MLD of the simulation S1Sa and S1Sb differ significantly from the S1 prediction. The SST of S1Sa (S1Sb) continuously overestimated (underestimated) than the SST of S1. The MLD of S1Sa (S1Sb) remain shallower (deeper) than the MLD of S1. However, the extent of overestimation (underestimation) in predicted SST and in MLD of S1Sa (S1Sb) are different in different periods of the year depending on the variation in observed solar fluxes. As regarding the increase (decrease) in solar radiation, the extent of the warming (cooling) of SST and the shallowing (deepening) of ML depend on the variability of the solar heat fluxes. During early two months of the NE monsoon (Nov-Dec) the cooling of the SST reduced (enhanced) by 2 ^{0}C and the deepening of ML reduced (enhanced) by 10 m. During January and Spring IM, the enhancement (reduction) in the warming of SST is very significant (4 ^{0}C) but the enhancement (reduction) in the deepening of ML though significant (upto 25 m), are mostly episodic. Unlike the early NE monsoon period, during early two months of the SW monsoon (Jun-July), the cooling in SST was enhanced (reduced) by 2 ^{0}C. During August and subsequent periods of simulation, the warming of SST was enhanced (reduces) by 3 ^{0}C and shallowing (deepening) of ML enhanced by 5 m. When all these simulations are compared with the observation, S1 gives the best results.

In summary, a 10 % change (increase and decrease) in the observed solar radiation can brings significant differences in the predicted surface layer temperature structures (SSTs and MLDs).

Model sensitivity to non-solar surface heat fluxes

The results in the case of 10% increase (decrease) in non-solar heat fluxes are exactly same as the results of the simulation in the case of 10% decrease (increase) in solar radiation.

B.3.3 Causes of general trends of the ML during both the monsoons

During both the monsoons the ML deepens and SST decreases; during the IMs, the ML shallows and SST increases. Weller et al. [3] suggest that the NE monsoon deepening of the ML is driven by convective entrainment and the SW monsoon deepening of the ML is driven by wind mixing. In contrast, earlier studies (McCreary [83], Düing and Leetma [76]) suggested that the SW monsoon ML deepening of the north Arabian Sea is driven by convective entrainment. Therefore the above issues need re-examination. The following experiments are carried out.

1. Very low wind experiment: (wind strength is reduced by 100 times i.e., ~0 m/sec).

2. Very low wind and reduced latent heat flux: (the same wind as in exp. 1 and the latent heat
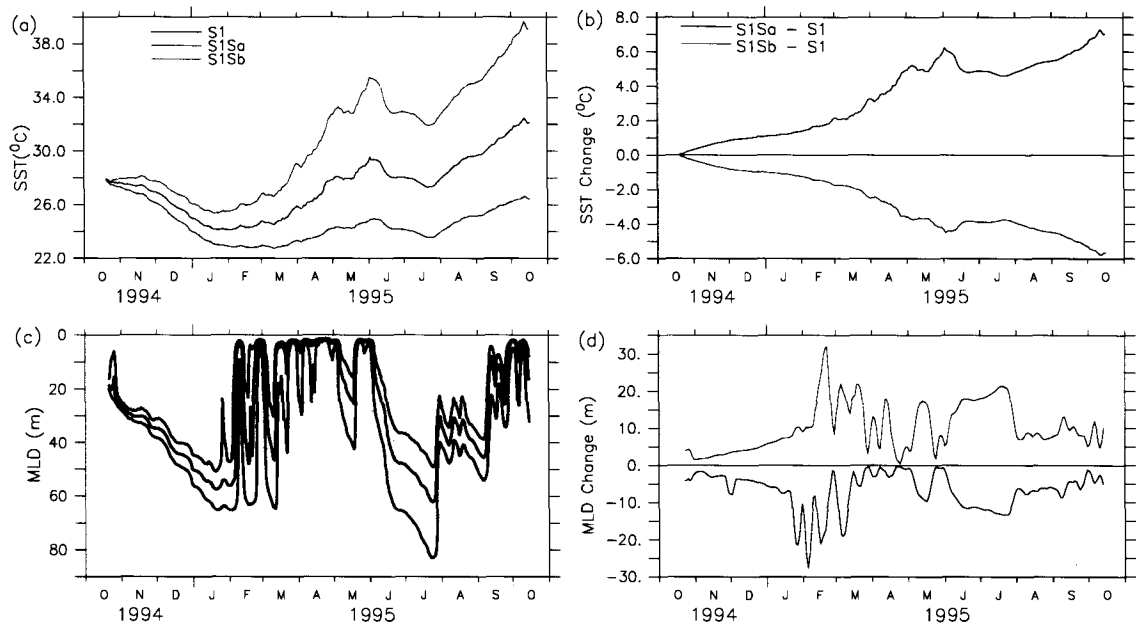
Figure B.7: Results of the sensitivity experiments corresponding to 10% change in the strength of solar radiation: S1, the case of exact solar heating; S1Sa, the case of increase in solar heating; S1Wb, the case of decrease in solar heating.

is reduced by four times)

Low wind experiment

The temperature simulation (W000) of the TKE model is carried out for the light wind condition. The remaining surface fluxes are kept same as in S1. The predicted SST and MLD of W000 are compared with the predicted SST and MLD of S1 in Fig. B.8. As shown, the SST of W000 coincides with the SST of S1 until the arrival of the SW monsoon. During the same period, the MLD of W000 does not differ much from MLD of the simulation S1. When the SW monsoon progresses, W000 started overestimating the SST (over S1) with slower rate for first two months (June-July) and after then the SST of W000 is overestimated rapidly. The evolution of predicted MLD of simulation W000 is underestimated significantly (almost 50 % of S1) during first two months of the SW monsoon. After July, MLD of W000 is reduced to zero during the rest of the year.
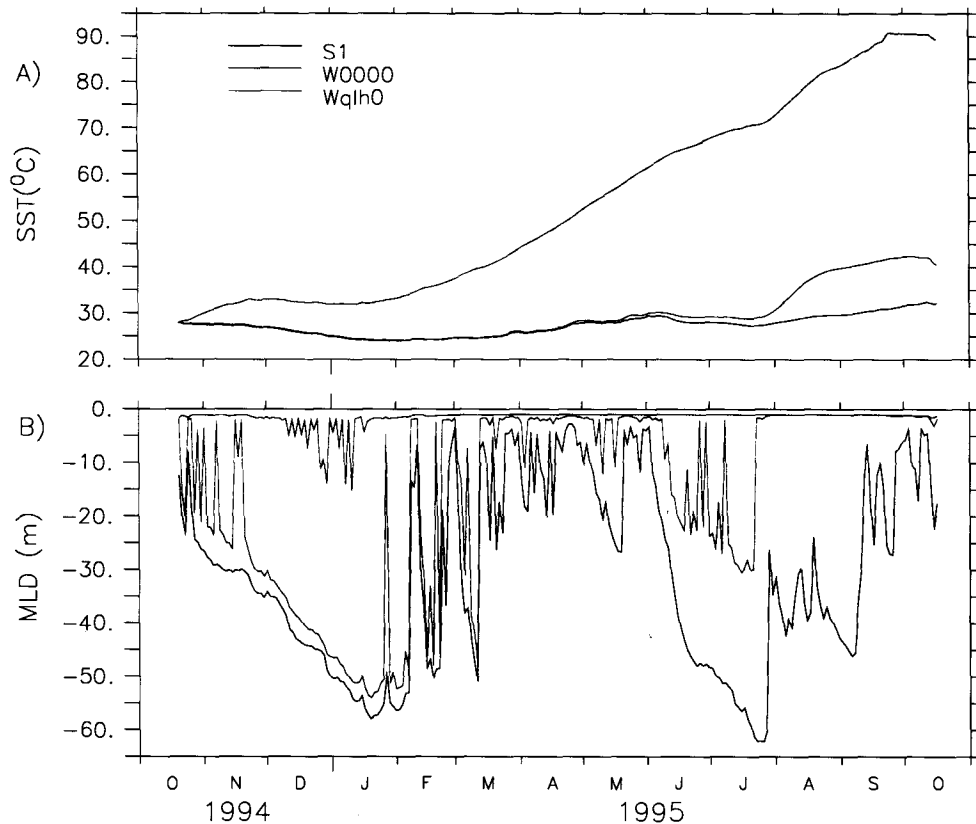
Figure B.8: The results of the simulations carried out to examine the causes of most general trends in the observed MLD and in the observed SST: (A) predicted SST and (B) predicted MLD from the simulations S1 (the case of exact surface wind stress and heat fluxes), W0000 (the case of with negligible wind stress with no change in surface heat fluxes), Wqlh0 (the case of reduced wind stress and reduced net heat loss).

These results show that wind mixing has secondary (minor) role on deepening and cooling of the ML during the NE monsoon, which implies that the surface heat flux must drive the winter cooling and deepening of ML. Further, the simulation shows that the deepening of ML and cooling of SST during early two months of the SW monsoon are not caused by wind stress only, mixing driven by net heat loss at the surface also play role too. During the subsequent period, only wind driven mixing has a significant control over the ML and SST.

Low wind and low heat loss experiment

Now the temperature simulation (Wqlh0) is carried out for the light wind and low heat loss condition. The remaining surface fluxes are kept the same as in S1 (see the Chapter 3.3). The result of this simulation is compared with the simulations S1 and W000 in Fig. B.8. As shown, the predicted SST overestimates the observation throughout the whole year. The ML is reduced to zero throughout the year of the simulation except for the period during December-January, when MLD

is about 10-15 m. This experiment confirmed that deepening of the ML and cooling of the SST during the NE monsoon are mostly due to convective entrainment driven by net buoyancy (heat) loss at the air-sea interface. This also confirmed that the June-July ML deepening and SST cooling are driven by combined effects from wind driven mixing as well as mixing driven by buoyancy (heat) loss at the air-sea interface.

B.4 Conclusion

(1) The numerical experiments corresponding to the salinity and seasonal evolution of biomass (chlorophyll) concentration show that the upper ocean thermal structure in the central Arabian Sea is weakly dependent on these two parameters. (2) Experiments with atmospheric fluxes show that the main trend in the deepening of the ML and cooling of the SST during the NE monsoon are due to a convective entrainment mixing driven by net heat loss at the surface (as a consequence of excess latent heat loss and reduced solar radiation). Contrary to what was proposed by Weller et al. [3] the main trends in deepening of the MLD and the cooling of the SST during the SW monsoon are not only caused by the rapid turbulent mixing driven by wind stress.

Appendix C

Bio-optical models of solar irradiance

A number of bio-optical models of solar irradiance were constructed for various applications to predict under-water light field. In the following, these models are presented in hierchical order (simple to complex).

The vertical attenuation of solar irradiance I(z) is parameterized according to Paulson and Simpson [101] as

$$I(z) = I(0) \times (R \times \exp(-z/\xi_1) + (1 - R) \times \exp(-z/\xi_2)) \qquad \text{(C.1)}$$

Here, subscripts 1 and 2 refer to the red and, blue-green, parts of the penetrating solar light and z is depth, positive downward. In this equation, R is a dimensionless parameter, and ξ_1 and ξ_2 are attenuation coefficients. Between these two attenuation coefficients, ξ_2 is dependent on phytoplankton (biomass) concentration. In the absence of biomass profile, sensitivity experiments are carried out against various optical water types as proposed by Jerlov's [102] to select constant parameters.

In most part of the oceans biomass dominates the attenuation of penetrating light. About half of the solar insolation incident on the sea surface is absorbed within the top meter. The remaining short-wave radiation of blue-green light decreases exponentially with depth following the Lambert-Beer law. Phytoplankton (biomass) is one of the principal absorbers of visible radiation in the sea. The penetration of light, distribution of under-water light field, absorption and scattering properties of the light in oceanic waters mainly depends on the constituents present in the water column. The light available for photosynthesis at different depths depends on a complete spectral and angular distribution of under water light field and the absorption and scattering properties of pure and oceanic waters. This was extensively dealt with, in photo-synthesis and light in

aquatic ecosystems by Kirk [113]. Sathyendranath and Platt [114] studied the spectral irradiance of light at the surface and in the water. They extensively studied the interaction of light field with chlorophyll its absorption its effect on temperature distribution using spectral and non-spectral, uniform and non-uniform biomass models. In view of above finding, equation (1) can be modified as

$$I(z) = I(0) \times \left(R \times \exp(-z/\xi_1) + (1 - R) \times \exp\left(- \int K\, dz\right) \right) \qquad \text{(C.2)}$$

In the simplest case, can $K(1/\xi_2)$ be assumed to spectral independent taken as

$K = 0.0611 + 0.0233 \times Chl$ Sathyendranath and Platt [114],

$K = 0.027 + 0.014 \times Chl$ Kirk [113], or

$K = 0.04 + 0.0088 \times Chl + 0.0054 \times Chl^{2/3}$ Parsons et al. [115],

where Chl is chlorophyll concentration (mg m^{-3}). For the spectral-dependent case the attenuation of solar irradince can be written as

$$I(z) = I(0) \times \left(R \times \exp(-z/\xi_1) + \sum_{r=1}^{r=61} R'_{\lambda_r} \times \exp(- \int K_{\lambda_r} dz) \right)$$
$$\sum_{r=1}^{r=61} R'_{\lambda_r} = 1 - R \qquad \text{(C.3)}$$
$$K_{\lambda_r} = Kw_{\lambda_r} + \chi_{\lambda_r} \times Chl^{e_{\lambda_r}}$$

where R'_{λ_r}s are calculated based on the Reference Solar Spectral Irradiance: Air Mass 1.5 (between 400-700 nm for every five nm interval normalized to whole spectral range) (from: http://rredc.nrel. gov/solar/spectra/am1.5/), and Kw_{λ_r}, χ_{λ_r}, and e_{λ_r} are taken from Table 2 of Morel & Maritorena [111].

The relative performance of these bio-optical model in predicting the under-water light field are presented in Fig. C.1. As shown in figure, three cases of uniform chlorophyll concentration are considered: low (0.1 mg m^{-3}), moderate (0.5 mg m^{-3}), and high (2.0 mg m^{-3}). Predicted I(z) from spectral model (par-spectral) decays much faster than the non spectral model (par - non spectral) in the ocean for all three chlorophyll concentration. For pure oceanic water (no chlorophyll and no other turbid materials) I(z) (parw- spectral) can penetrate much deeper (the photic depth, i.e., 1% of light level lies much below 150 m). Thus choosing the optical model to study the mixed-layer processes is very crucial.
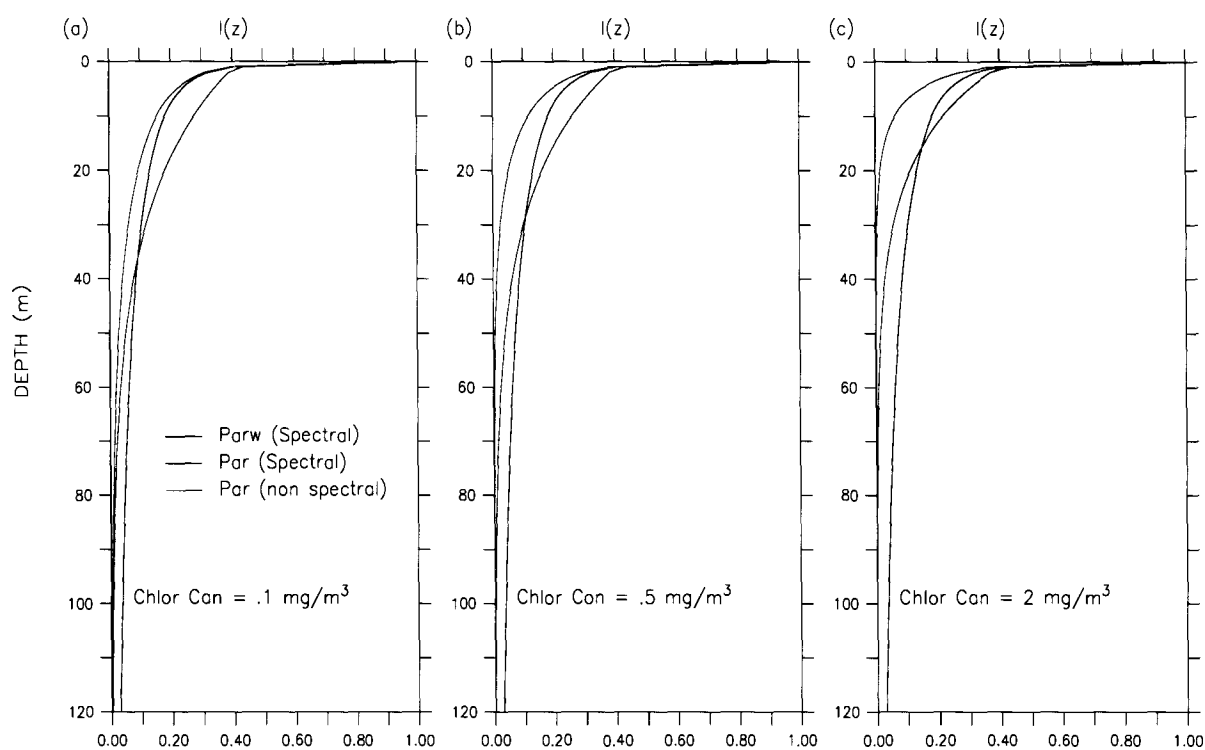
Figure C.1: Under-water solar irradiance predicted from spectral and non spectral bio-optical model for three cases of uniform Chlorophyll concentration: (a) 0.1 mg m^{-3}, (b) 0.5 mg m^{-3}, and (c) 2 mg m^{-3}(see the text for detail).

Appendix D

Additional simulations

D.1 Simulation S2a*: Fischer-based forcing

Simulation of temperature field is carried out by initializing the model on 15 November instead of 20 October (S2a*) similar to S2a. As seen in Fig. D.1, the thermal structure predicted in S2a* is better than in the previous simulation S2a. The predicted SST (Fig. D.1a) parallels the observations throughout the year and the agreement is much better than in S1 during the SW monsoon and during the subsequent period owing to heat removal through the horizontal advection (see Fig. 3.10). The predicted MLD (Fig. D.1b) is not as good as in S2a, but better than in S1. The deepening of ML is significantly underestimated (25 m) during the NE monsoon, and then the prediction almost parallels the observation. The evolution of predicted vertical temperature profile (Fig. D.1c) and the difference between the predicted and observed temperature (Fig. D.1d) show that the temperature of the near-surface layer (upper 40 m) parallels the observation throughout the year, but the temperature in sub-surface (40-160 m) is underestimated. The underestimates are large (7 °C) during the SW monsoon and subsequently. The predicted temperature trend (see Fig. D.1e) mostly matches the observations (Fig. 3.3c). The difference between the predicted and observed temperature trend (Fig. D.1f) is only significant (more than 4 W m^{-3}) in the sub-surface layers during the monsoonal periods.

In summary, the results of above temperature simulations (S2a and S2a*) show that the Fischer et al. [4] estimates of horizontal heat fluxes are not able to improve the model prediction during the early NE monsoon (20 October to mid November-1994). The enormous cooling, driven by horizontal advection of the near-surface layer during this period dominates the model prediction during the rest of the year. Thus, this cooling signal in the horizontal advective heat estimates is suspect. During the rest of the year, the estimates of horizontal heat fluxes may be considered
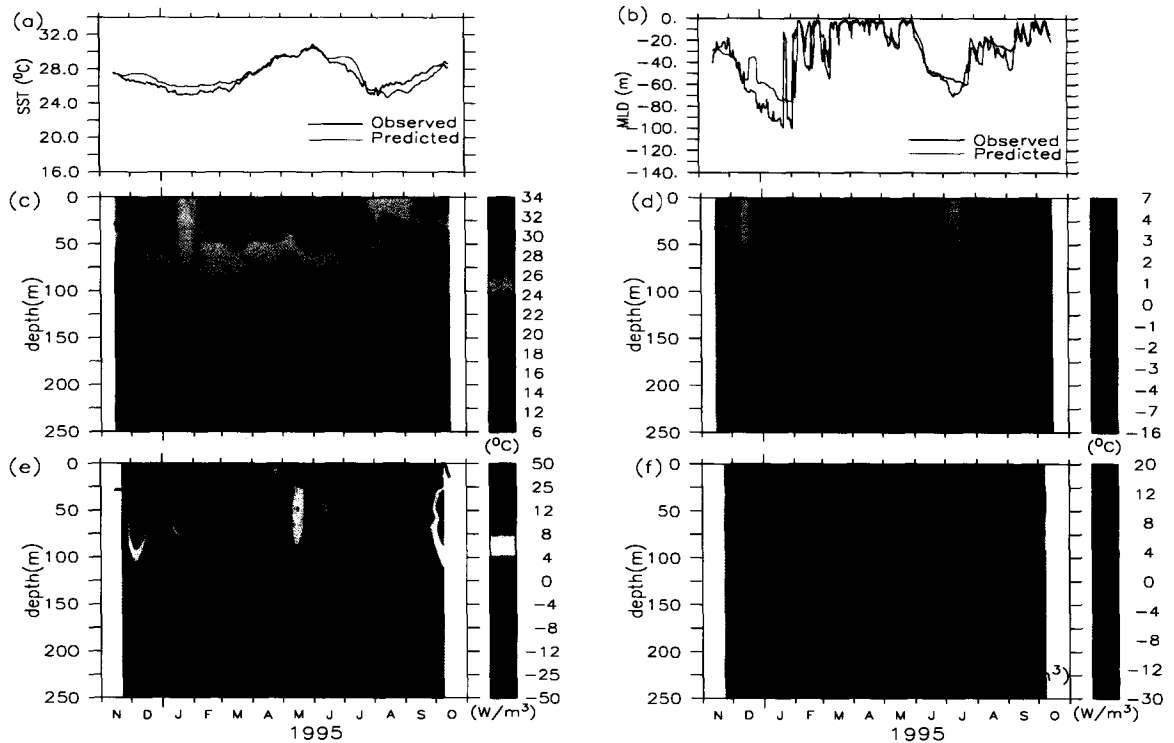
Figure D.1: Results of the numerical simulation S2a*: (a) predicted (red) and observed (black) SST; (b) predicted (red) and observed (black) MLD; (c) vertical structure of temperature (color) and MLD (blue line); (d) predicted minus observed temperature; (e) vertical structure of predicted temperature trend (color) and MLD (blue line); (f) predicted minus observed temperature trend. The data are smoothed as in Fig. 4.1.

as good. Use of the advective field (during mid-November 1994 to mid-October 1995) improved the model prediction significantly in the near-surface layer during the SW monsoon and distorted strongly in the sub-surface due to strong episodic events of the cooling and warming trends associated with it. This implies, the role of vertical advection or the estimates of horizontal advective fluxes might carries much stronger signals than the real signals in the sub-surface layers.

D.2   Simulation S2d: Fischer-based forcing

A simulation (S2d) is carried out similar to the simulation S2c, but the model is initialized on 15 November 1994. The new simulation (S2d) is good and predicted the temperature structure very accurately throughout the year over all depths.

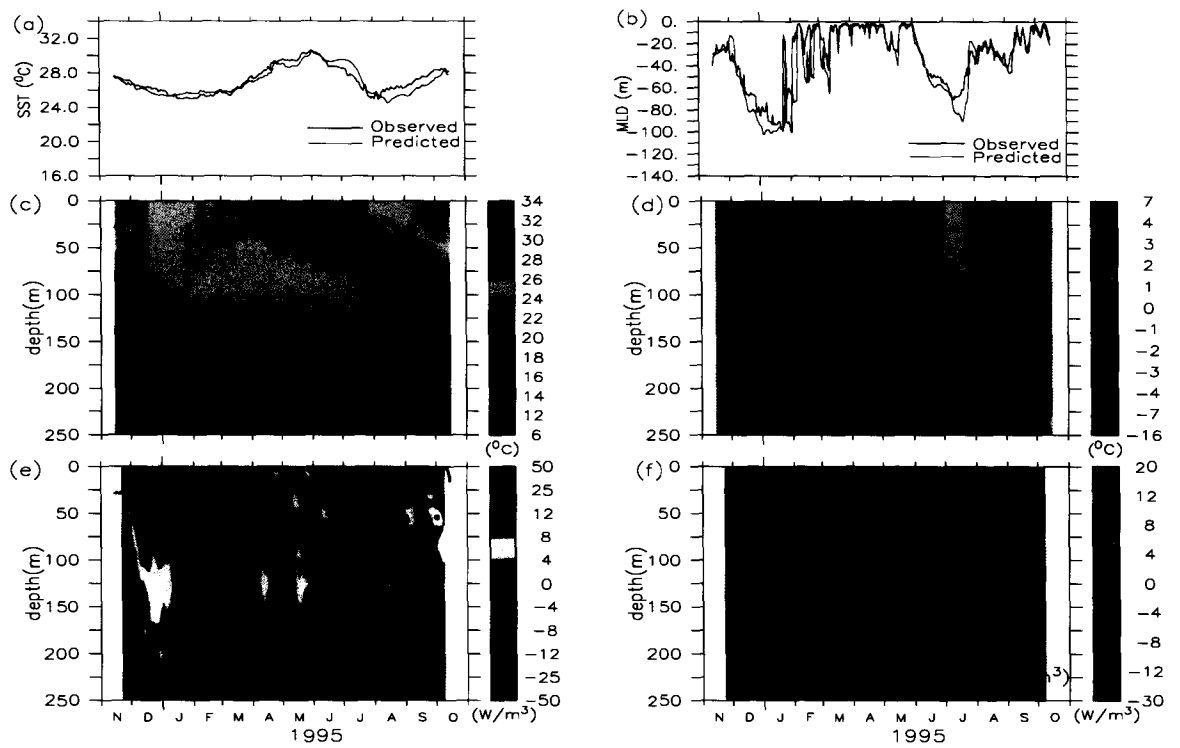Figure D.2: Results of the numerical simulation S2d: (a) predicted (red) and observed (black) SST; (b) predicted (red) and observed (black) MLD; (c) vertical structure of predicted temperature (color) and MLD (blue line); (d) modeled minus observed temperature; (e) vertical structure of predicted temperature trend (color) and MLD (blue line); (f) predicted minus observed temperature trend. The data are smoothed as in Fig. 4.1.

Appendix E

Estimation of vertical velocity from temperature profile

E.1 Theoretical background

Total vertical velocity $w = w_c + w_A$, where w_C and w_A are the cross and along the iso-line (isopycnal/isotherm) component of the vertical velocity. The cross-isothermal component of vertical velocity is due to two diapycnal processes: (i) heating by penetrating solar radiation and (ii) small scale vertical mixing (Gourious and Reverdin , 1992). At the depth below the mixed-layer and below the photic zone, effect of penetrating solar radiation and small scale mixing process are very small, therefore w_C is negligible (much smaller than 0.1 m d^{-1}, which follows from the scale anlysis by Friedrichs and Hofmann [110] 2001).

The along-isoline component of vertical velocity is due to two effects: (i) local upward movement of isoline $\left(\frac{\partial \eta}{\partial t}\right)$ and (ii) advection along a stationary, sloping isoline $\left(u\frac{\partial \eta}{\partial x} + v\frac{\partial \eta}{\partial y}\right)$:

$$w_A = \frac{\partial \eta}{\partial t} + u\frac{\partial \eta}{\partial x} + v\frac{\partial \eta}{\partial y} \qquad (1)$$

where $\eta = \eta(x, y, t)$ is the elevation of isoline.

Let us assume that the deeper ocean (below the mixed layer) is geostrophic, i.e.

$$\begin{cases} u = -\frac{1}{\rho f}\frac{\partial p}{\partial y} \\ v = \frac{1}{\rho f}\frac{\partial p}{\partial x} \end{cases} \qquad (2)$$

As ocean is hydrostatic , i.e. $\frac{\partial p}{\partial z} = -\rho g \Rightarrow \int_{p_0}^{p} \partial p = -\int_{\eta}^{z} \rho g \partial z \Rightarrow$

$$p = p_0 + \rho g(\eta - z) \qquad (3)$$

Where $p_0 = p_0(x, y)$ is the pressure on the surface of iso-line which is the sum of the pressure at the free surface $(p_a(x, y))$ and pressure due to over laying water mass $(\rho g(H_0 - \eta)$, where $H_0(x, y)$ be the thickness of the fluid layer in the absence of motion (see the Fig. 1)

$$p_0 = p_a + \rho g(H_0 - \eta) \qquad (4)$$

Using eq (4) in eq (3)

$$p = p_a + \rho g(H_0 - z) \qquad (5)$$

Now uses of eq (2 and 3) in eq (1), yields

$$w_A = \frac{\partial \eta}{\partial t} + \frac{1}{\rho f}\left(\frac{\partial(p_a + \rho g H_0)}{\partial x}\frac{\partial \eta}{\partial y} - \frac{\partial(p_a + \rho g H_0)}{\partial y}\frac{\partial \eta}{\partial x}\right) \qquad (6)$$

As $P_a \ll \rho g H_0$ (for an instant at 10 m depth $\rho g H_0$ is approximately 10^4 time of $P_a = $ 1atmo)

$$w_A = \frac{\partial \eta}{\partial t} + \frac{g}{f}\left(\frac{\partial H_0}{\partial x}\frac{\partial \eta}{\partial y} - \frac{\partial H_0}{\partial y}\frac{\partial \eta}{\partial x}\right) \qquad (7)$$

In the normal mode of oscillation (small oscillation), it can be assumed that $H_0(x, y)$ can varies linearly with $\eta(x, y)$ i.e.

$$H_0(x, y) = \alpha \eta(x, y) \qquad (8)$$

Where α is a constant. Using equation (8) in second expression of right hand side of equation (8), we have

$$\frac{\partial H_0}{\partial x}\frac{\partial \eta}{\partial y} - \frac{\partial H_0}{\partial y}\frac{\partial \eta}{\partial x} = 0 \qquad (9)$$

Therefore equation (7) become

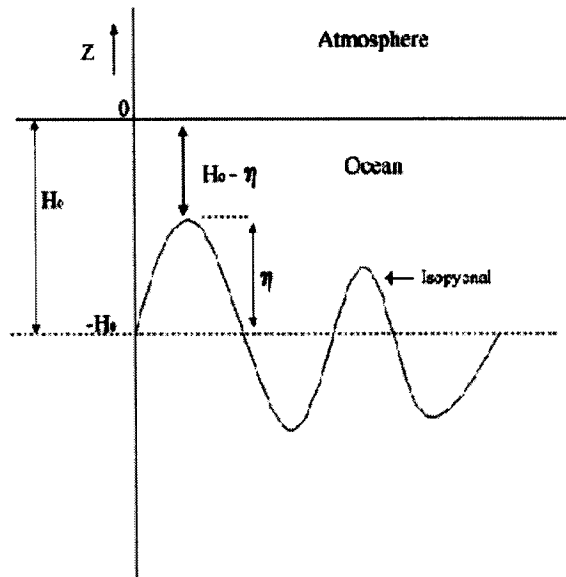$$w_A = \frac{\partial \eta}{\partial t} \qquad (10)$$

Figure E.1: Schematic of vertical movement of isopycnal

E.2 Estimation of vertical velocity at the moored-array observation

In situ vertical velocity is estimated from the mooring temperature profiles as follows. The profiles are averaged over 5 days. The shift during two consecutive 5-day periods is estimated for two layers, 100–160 m and 180–240 m by using a least-squares fit. This shift is assumed to be due to the vertical velocity field. The vertical velocities are estimated at the centre of each layer and are assumed to be 0 at the surface (rigid-lid approximation). The vertical velocity at other depths in the interval 0–250 m layer is estimated by using linear interpolation and extrapolation using these three values. By averaging the profiles over 5 days, the high-frequency signals (dominant semi-diurnal tide, diurnal tide, and inertial gravity waves) are filtered out. Our estimate of vertical velocity is dependent on the assumption that vertical movement of water controls the vertical changes in temperature profiles. The assumption is consistent with the linear quasi-geostrophic approximation (see Pedlosky [116], pages 67–70). The estimate is expected to be more suitable at sub-surface levels, below the mixed layer and below the photic zone (depth up to which solar short-wave radiation can penetrate), where this assumption is better obeyed. Our method of estimating the vertical velocity is similar to that of Friedrichs and Hofmann [110] (see Appendix-B). The resulting vertical velocities are presented in Fig. E.2. The strength of this vertical velocity is up to 0.003 cm s^{-1} (equivalent to 2.6 m day^{-1}; contrast this with the 18 m day^{-1} estimate of Fischer et al. [4]). As shown, the general trends resemble those in SODA, with downwelling prevailing until the end of the NE monsoon, weak vertical movements from February to June, and active upwelling during the SW monsoon. However, the in situ W exhibits more short-scale variability than in
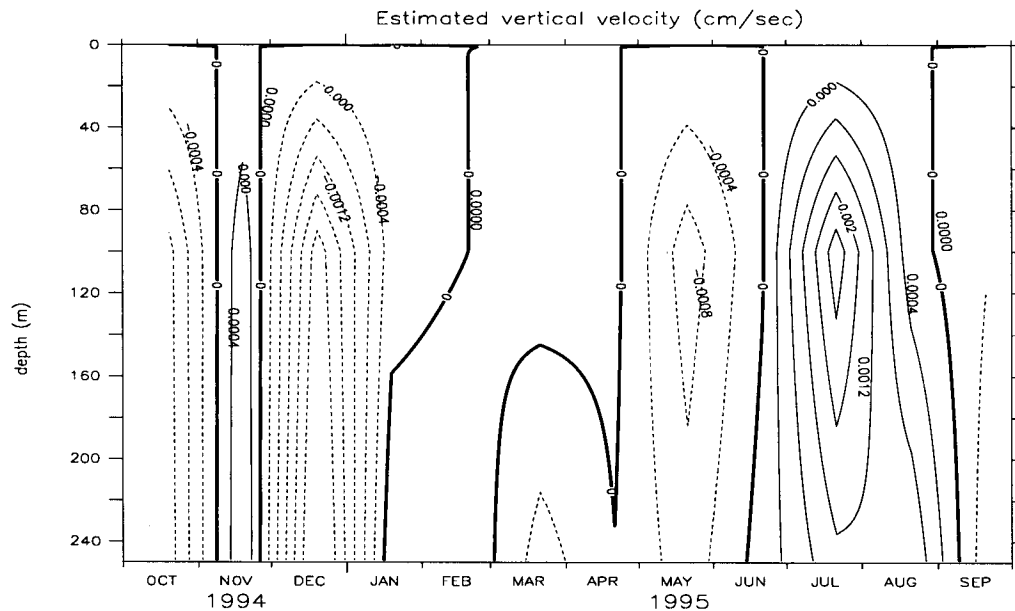
Figure E.2: Contours of vertical velocity (cm/s) based on vertical shift on temperature profile.

SODA. In particular, the downwelling reversed to upwelling from early to late November. Strong downwelling events occur in May and mid-August in sub-surface layers. The July upwelling is much stronger than predicted by SODA. Almost the same estimate of vertical velocity could be obtained by measuring the vertical excursion of different isotherms in the sub-surface layers.

E.3   Examining the vertical velocity (WT) based on T-shift (simulation S3d)

As the vertical velocity from SODA-OGCM is suspected for lacking the small-scale variability, another estimates of vertical velocity (WT) is estimated in the section ?? based on the vertical shift of the temperature profile. The estimates (WT) are used for the vertical advective corrections of the predicted temperature field. The results of the simulation (S3d) are presented in Fig E.3. This simulation (S3d) shows very good agreement between the prediction and the observations. As regards the SST (Fig. E.3a), it is almost unaffected by the change in forcing vertical velocities. In contrast, the vertical structure (Figs. E.3b-c) now exhibits a variability very similar to that in the observations (Fig. 3.3b), in particular for the thermocline layer and for the MLD, and during the periods of intense meso-scale activity (early November to mid-December and August). The remaining departures (Fig. E.3d) are significantly reduced with respect to S3c until mid-July.

In particular, the transient upwelling in November prevents the sub-surface overestimate present in S3c, and the stronger downwelling in December and the transient downwelling in late May prevent most of the S3c sub-surface underestimates. It is after the peak of the SW monsoon that the improvements are the least apparent, with mis-estimates still present in surface (+3 °C) and in sub-surface layers (-2 °C). It is also worth noting that, once the problems which occur in S3c during the NE monsoon have been settled, the thermal structure is well reproduced throughout the inter-monsoon. The most of the warming and cooling trends in the sub-surface are reproduced well (Fig. E.3e-f). Over the year, the mean temperature in the mixed layer differs from the observed mean by -0.28 °C and the temperature profiles are simulated with an accuracy of 2.14±1.58 % (mean ± standard deviation) in terms of absolute relative error while the mean temperature difference is -0.18 °C and the accuracy is (2.72±2.15 %) for the 0 - 250 m layer. The trend in the predicted temperature was integrated over the ML and over the 0 - 250 m layer for S3d. They are compared to the observed trend in Fig. E.4 (in units of heat flux). As shown, this simulation reproduces most of the observed features for both layers. It has, however, to be noted that the model failed to reproduce a few short-term events. These events (a few days long) occurred mainly in January and during the SW monsoon, concerned the whole layer (Fig. E.4 lower panel), and had a marked signature in the ML (Fig. E.4 upper panel).
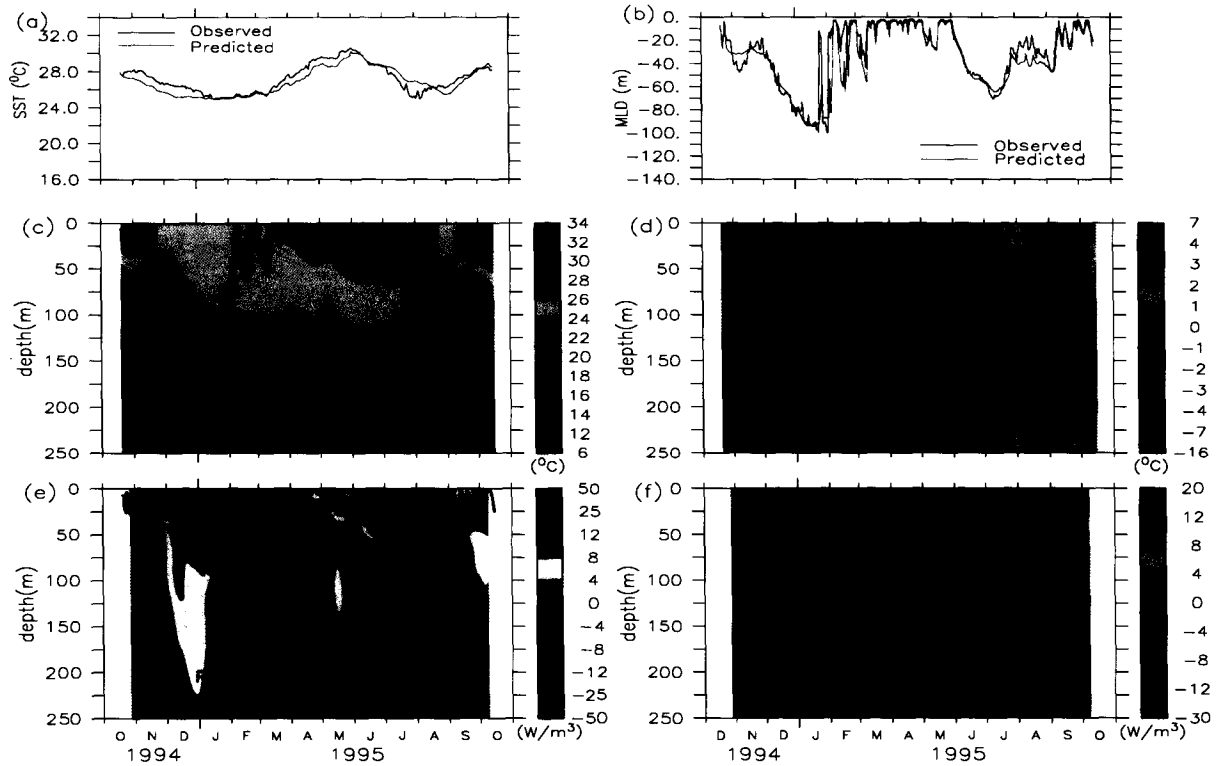
Figure E.3: Results of the numerical simulation S3d: (a) predicted (red) and observed (black) SST; (b) predicted (red) and observed (black) MLD; (c) vertical structure of predicted temperature (color) and MLD (blue line); (d) modeled minus observed temperature; (e) vertical structure of predicted temperature trend (color) and MLD (blue line); (f) predicted minus observed temperature trend. The data are smoothed as in Fig. 4.1.
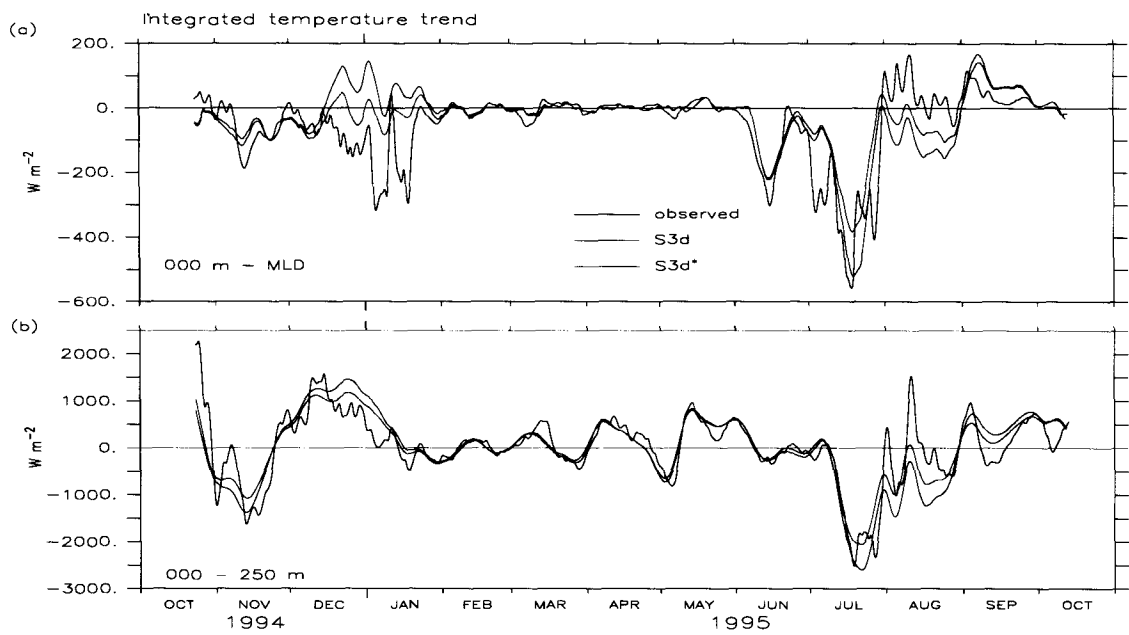
Figure E.4: Evolutions of the observed (black) and the modeled (red) temperature trend integrated over the ML (upper panel) and over the 0-250 m layer (lower panel) for S3 experiment.

Appendix F

Additional figures
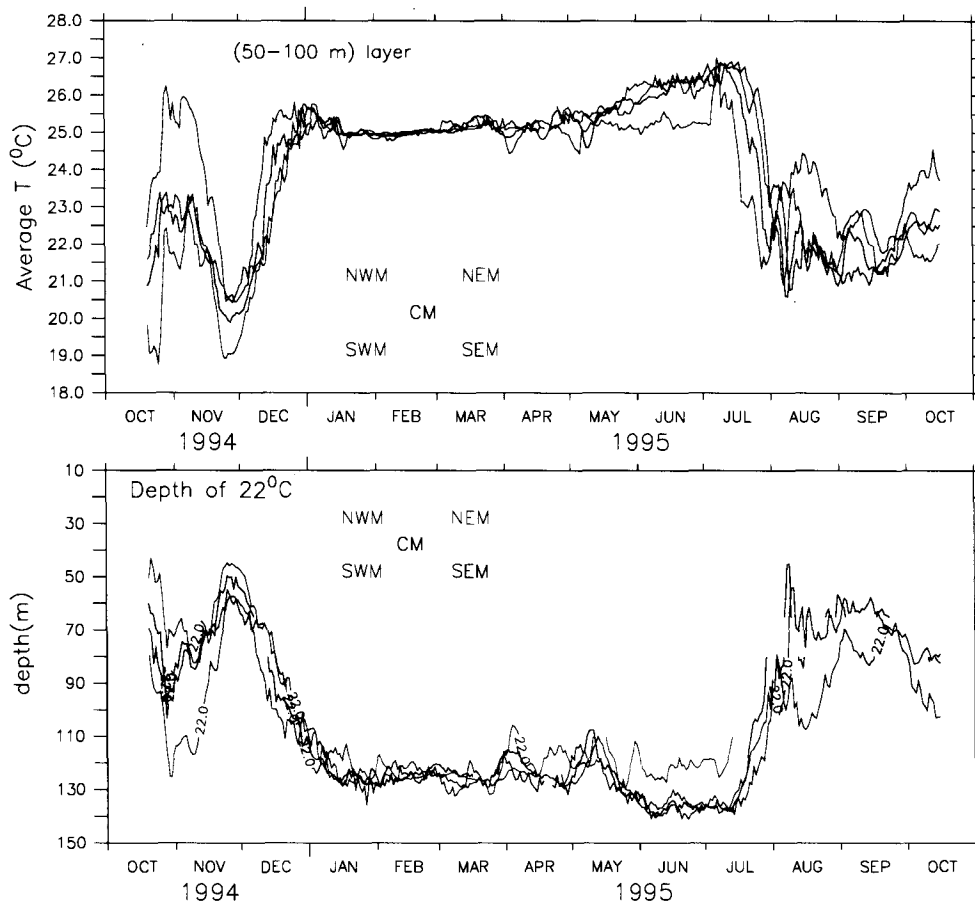
Figure F.1: Averaged temperature evolution between 50 and 100 m (upper panel) and depth of 22°C iso-therm from the four moorings (lower panel). Dark color: central mooring (CM); red color: north west mooring (SWM); green color: south west mooring (SWM); and blue color: south east mooring (SEM); cyan color: north east mooring (NEM) which was missed. During November of the NE monsoon and August of the SW monsoon (August) the SWM shows large differences from other mooring.
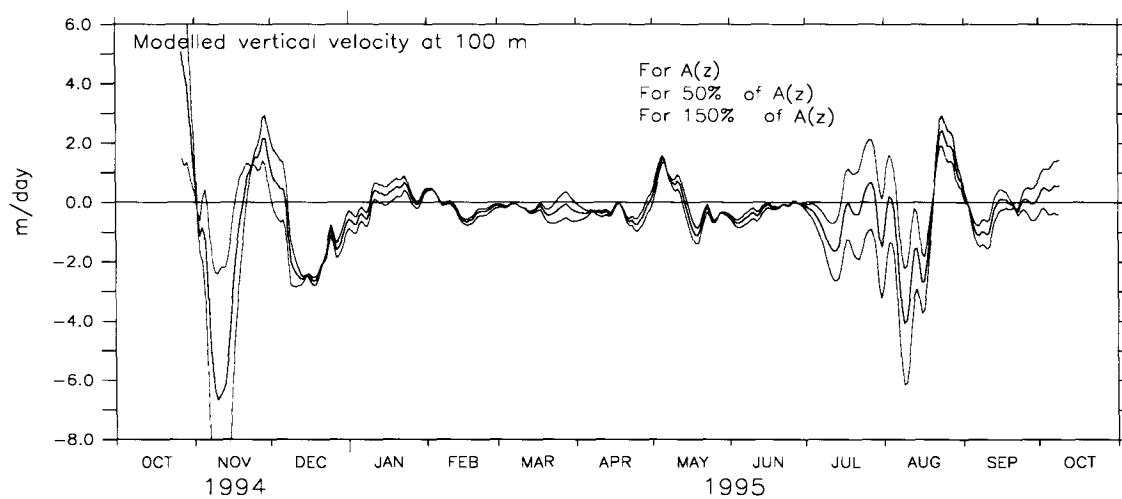
(a)
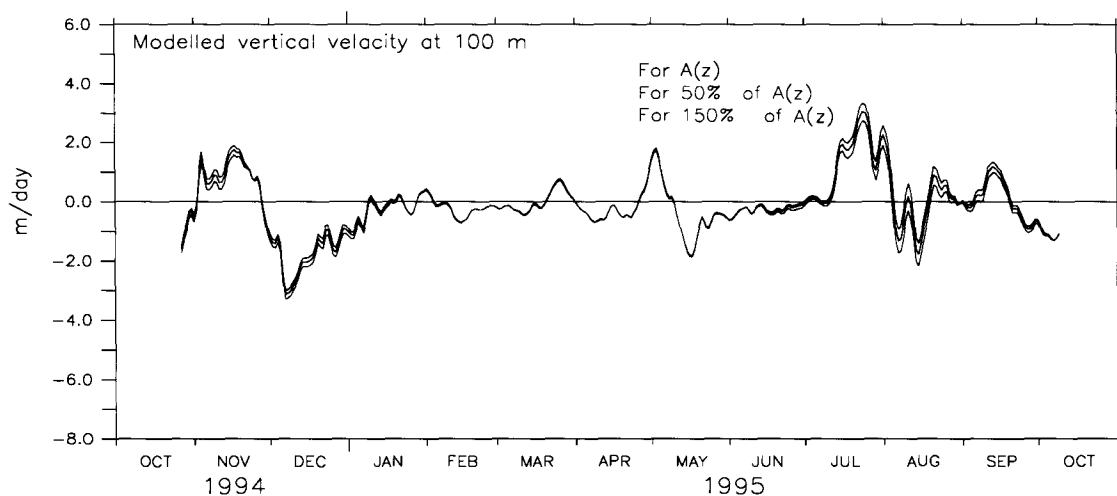
(b)

Figure F.2: (a) Sensitivity of predicted vertical velocity to the Fischer-based horizontal advective heat fluxes. (b) same as (a) but with respect to Reynolds-based horizontal advective heat fluxes.

Bibliography

[1] Findlater, J., 1969. A major low-level air current near the Indian Ocean during the northern summer. *Quaterly Journal of the Royal Meteorological Society*, 95: 362–380.

[2] Weller, R. A., M. F. Baumgartner, S. A. Josey, A. S. Fischer, and J. C. Kindley, 1998: Atmospheric forcing in the Arabian Sea during 1994-1995: observation and comparisons with climatology, and models. *Deep-Sea Research II* 45: 1961–1999.

[3] Weller, R. A., A. S. Fischer, D. L. Rudnick, C. C. Eriksen, T. D. Dickey, J. Marra, C. Fox, R. Leben, 2002. Moored Observations of upper-ocean response to the monsoon in the Arabian Sea during 1994-1995. *Deep Sea Research II* 49: 2195–2230.

[4] Fischer, Albert S., R. A. Weller, D. L. Rudnick, C. C. Eriksen, C. M. Lee, K. H. Brink, C. A. Fox, and R. R. Leben, 2002. Mesoscale eddies, coastal upwelling, and the upper-ocean heat budget in the Arabian Sea. *Deep Sea Research II* 49: 2231–2264.

[5] Peixoto, J. P. and A. H. Oort, 1992: Physics of Climate. *Americal Institute of Physics*, 500 pp.

[6] Houghton, J.T., L.G. Meira Filho, B.A. Callender, N. Hariris, A. Kattenberg, and K. Maskell, 1995. The science of climate change, (eds) *Cambridge University Press*, Cambridge, UK.

[7] Mitchell, J. M., 1976: An overview of climatic variability and its causal mechanisms. *Quaternary Research*, 6: 1–13.

[8] Oceanography Course Team, 2001. Ocean Circulation, Second edition, *The Open University*.

[9] Bjerknes, J. A, 1966. Possible response of the atmospheric Hardley circulation to equatorial anomalies of ocean temperature. *Tellus*, 18: 820–829.

[10] Bjerknes, J., 1969. Atmospheric tele-connections from the equatorial Pacific. *Monsoon Weather Review*, 97: 163–172.

[11] Gray, W. M., 1968. Global view of the origin of tropical disturbances and storms. *Monthly Weather Review*, 96: 669-700.

[12] McBride, J., 1995. Tropical cyclone formation (chapter 3), Global Perspectives on Tropical Cyclones. *Ed. R. L. Elsberry*, World Meteorological Organisation Report WMO/TD-693: 63–105.

[13] Briegel, L. M. and Frank W. M., 1997. Large-scale influences on tropical cyclogenesis in the western North Pacific, *Monsoon weather Review*, 125: 1397–1413.

[14] Lindzen. R.S., and S. Nigam, 1987. On the role of sea surface temperature gradients in forcing low-levl wind and convergence in the Tropics. *Journal of Atmospheric Science*, 44: 2418–2436.

[15] Gray, W. M., 1984. Atlantic seasonal hurricanes frequency. Part 1: El Niño and 30 mb quasi-biennial oscillation influences. *Monthly Weather Review*, 112: 1649–1668.

[16] Goldenberg, S. B., and Shapiro, L.J., 1996. Physical mechanisms for the association of El Niño and west African rainfall with Atlantic major hurricane activity. *Journal of Climate*, 9: 1169–1187.

[17] Lander, M. A., 1994. An exploratory analysis of the relationship between tropical storm formation in the western Pacific and ENSO. *Monsoon Weather Review*, 122: 639–651.

[18] Chan J.C.L., 2000. Tropical cyclone activity over the western North Pacific associated with El Niño and La Niña events. *Journal of Climate*, 13: 2960–2972.

[19] Chu, P.S. and Wang, J., 1997. Tropical cyclones occurrences in the vicinity of Hawaii: are the difference between El Niño and non-El Niño years significant? *Journal of Climate*, 10: 2683–2689.

[20] Hastings, P. A., 1990: Southern Oscillation influences on tropical cyclones activity in the Australian/south-west Pacific region. *International Journal of Climatology*, 10: 291–298.

[21] Evans, J. L., and Allan, R. J., 1992. El Niño/Southern Oscillation modification to the structure of the monsoon and tropical cyclone activity in the Australasian region. *International Journal of Climatology*, 12: 611–623.

[22] Basher, R. E. and Zheng, X., 1995: Tropical cyclones in the southwest Pacific: spatial patterns and relationships to Southern Oscillation and sea surface temperature. *Journal of Climate*, 8: 1249–1260.

[23] Broadbridge, L.W. and Hanstrum, B.N., 1998. The relationship between tropical cyclones near Western Australia and the Southern Oscillation index. *Australian Meteorological Magazine*, 47: 183–189.

[24] Gray, W.M. LAD, 1994. Multiple linear regrassion forecasts of Atlantic tropical storm activity for 1995. *Experimental Long-lead Forecast Bulletin*, 3: 12–13.

[25] Elsner, J.B., G.S. Lehmiller, and T.B. Kimberlain, 1996. Early August forecasts of Atlantic tropical storm activity for the balance of the 1996 season, using Poisson models. *Experimental Long-lead Forecast Bulletin*, 5: 26–38.

[26] Chan, J.C.L, J.E. Shi, and C.M. Lam, 1998. Seasonal forecasting of tropical cyclone activity over the western North Pacific and the South China Sea. *Weather and Forecast*, 13: 997–1004.

[27] NOAA, 2002. www. pmel.noaa.gov.

[28] Vialard, J., and P. Delecluse, 1998. An OGCM study for the TOGA decade. Part I: Role of salinity in the Physics of the Western Pacific Fresh Pool. *Journal of Physical Oceanography*, 28: 1071–1088.

[29] Levitus S. and T.P. Boyer. 1994. World Ocean Atlas 1994 Volume 4: Temperature. NOAA Atlas NESDIS 4. 117 pp.

[30] Sprintall, J., and M. Tomczak, 1992. Evidence of the barrier layer in the surface layer of tropics. *Journal of Geophysical Research*, 97: 7305–7316.

[31] Delcroix, T., G. Eldin, M.-H. Radenac, J. Toole, and E. Firing, 1992. Variation of the western equatorial Pacific, 1974-1988, Journal of Geophysical research, 97 (Suppl.): 3249–3262.

[32] Sprintall, J., and M. J. McPhaden, 1994. Surface layer variations observed in multi year time series measurements from the western equatorial Pacific. *Journal of Geophysical Research*, 99: 963–979.

[33] Vialard, J., and P. Delecluse, 1998. An OGCM study for the TOGA decade. Part II: Barrier-Layer Formation and Variability, *Journal of Physical Oceanography*, 28: 1089–1106.

[34] Shenoi, S. S. C., D. Shankar, and S. R. Shetye, 2002. Differences in heat budgets of the near-surface Arabian Sea and Bay of Bengal: Implications for the summer monsoon. *Journal of Geophysical Research* 107 C6, 10.1029/2000JC000679.

[35] Durand, F., S. R. Shetye, J. Vialard, D. Shankar, S.S.C. Shenoi, C. Ethe, and G. Madec, 2004. Impact of temperature inversions on SST evolution in the southeastern Arabian Sea during the pre summer-monsoon season, *Geophysical Research Letter*, 31, L01305, doi:10.1029/2003 GL018906.

[36] Sathyendranath, S., A. D. Gouveia, S. R. Shetye, and T. Platt, 1991. Biological controls of surface temperature in the Arabian Sea. Nature, 349: 54–56.

[37] Gadgil, S., P. V. Joseph and M. V. Joshi, 1984. Ocean-atmosphere coupling over monsoon regions. *Nature*, 31: 141–143.

[38] Webster, P.J., T. Palmer, M. Yanai, V. Magan, J. Shukla, R. A. Tomas, M. Yanai, and A. Uasunari, 1998: Monsoons: Processes, predictability and the prospects for prediction. *Journal of Geophysical Research*, 103 C7: 14451–14510.

[39] Science Plan of the Indian Climate Research Programme, 1996. *Department of Science and Technology, Government of India, New Delhi*, pp186.

[40] Varadachari, V.V.R., 1990. Oceans and Climate, *Monograph*, Anonymus.

[41] Choudhary, M. H. K and S. Karmarkar, 1982. Diagnostic study on some aspects of the energetics and structural features of the troposhere over the Arabian Sea with advancement of SW monsoon. *In: Results of Summer Monex Field Phase Research (Part B), FGGE Operations Report Vol. 9, ICSU/WMO*: 212–221.

[42] Hastenrath, S., 1985. Climate and circulation of the tropics, *D. Reidel Publishing company, Derdretcht, Holland,* 455 pp.

[43] Hastenrath, S. and Lamb, P. J., 1980. Climatic Atlas of the Indian Ocean Part 2. The Oceanic heat budget. *University of Wisconson Press*, 110pp.

[44] Saha, K.R., 1970. Zonal anomaly of sea surface temperature in the equatorial Indian Ocean and its possible effect upon monsoon circulation. *Tellus*, 22: 403–409.

[45] Saha, K.R., 1974. Some aspects of the Arabian Sea monsoon. Tellus, 26: 464–476.

[46] Rao, L.V.G., V. Ramesh Babu, A.A. Fernandes and V.V.R. Varadachari, 1976. Studies on thennal structure of the northwestern Indian Ocean in reflation to the southwest monsoon over the Indian Peninsula. *In: Proceedings of the symposium on tropical monsoons*. Indian Institute of Tropical Meteorology, Pune, pp. 219.

[47] Rao, A.V.A.K., R.K. Datta, G.S. Mandai and Indu Bala, 1980. Certain aspects of SST and moisture distribution over the Arabian Sea during pre-onset phase of Monsoon 1979. *In: Results of Summer Monex Field Phase Research (part B), FGGE Operations Report Vol. 9 ICSU/WMO*, 167–172.

[48] Nuzhdin, P.V., 1982. On laws covering fluctuations of the Arabian Sea active layer thermodynamics properties and air-sea energy exchange characteristics during the southwest monsoon. *In: GARP International Conference on the scientific results of the monsoon experiment, Bali, ICSU/WMO, Geneva*, 724–727.

[49] Jambunathan, R. and K. Ramamurty, 1975. Sea and air temperature distribution over the Arabian Sea during southwest monsoon, 1973. *Journal of Meteorology and Geophysics*, 26: 465–478.

[50] Anjaneyulu, T.S.S., 1980. A study of the air and surface temperature over the Indian Ocean. *Mausam*, 31: 551–560.

[51] Joseph, P.V., 1981. Seasonal scale persistance of equatorward intrusion of upper tropospheric westerlies over south Asia and monsoon performance dunng 1964 to 1979. *In: GARP International Conference on the Scientific Results of the Monsoon Experiment*. Bali, Indonesia, October 1981. ICSU/WMO, 171–174.

[52] Joseph, P. V., 1981. Ocean-atmosphere interaction on a seasonal scale over north Indian Ocean and Indian monsoon rainfall and cyclone tracks -a preliminary study. *Mausam*, 32: 237–246.

[53] Joseph, P. V. and P. V. Pillai, 1986. Air-sea interaction on a seasonal scale over north Indian Ocean -Part II: Monthly mea" atmopheric and oceamc parameters during 1972 and 1973. *Mausam*, 37: 158–168.

[54] Joseph, P. V., 1976. Monsoon rainfall and cyclone tracks in relation to 500 mb altitudes. 1955–1974. *In: Proceedings of the symposium on tropical monsoons*. Indian Institute of Tropical Meteorology, Pune, pp. 494–504.

[55] Joseph, P. V. and P. V. Pillal, 1984: Air-sea interaction on a seasonal scale over the north Indian Ocean -IJI Part I: Interannual variations of sea surface temperature and Indian summer monsoon rainfall. *Mausum*, 35:323–330.

[56] Golovastov, V.A., V.V. Pokudov and V.B. Kholmanov., 1982. Peculiarities of the water thermodynamics in the tropical Indian Ocean. *In: International Conference on the Scientific results of Monsoon Experiment*. Bali, Indonesia, October 1981. ICSU/WMO, 720–723.

[57] Shukla, J. and B.M. Mishra, 1977. Relationships between sea surface temperature and wind speed over the central Arabian Sea and monsoon rainfall over India. *Monthly Weather Review*, 105, 998–1002.

[58] Weare, B.C., 1979. A statistical study of the relationship between ocean surface temperatures and the Indian monsoon. *Journal of Atmospheric Science*, 36: 2279–2291.

[59] Ramesh Kumar, M.R., S. Sathyendranath, N.K. Viswambharan and L. V.G. Rao, 1986. Sea surface temperature variability over North Indian Ocean, a study of two contrasting monsoon seasons. *Proc. Ind. Acad. Sci. (Earth and Planetary Science)*, 95: 435–446.

[60] Ramesh Kumar, M.R., Sadhuram, Y. and L.V.G. Rao, 1986. Premonsoon sea surface temperature anomaly off the "western Indian Ocean. A probable predictor for monsoon rainfall; Presented at the Seminar on Long-range "forecasting of monsoon rainfall", *India Meteorological Society*, New Delhi, April 16–18.

[61] Cadet, D.L. and B.C. Diehl, 1984. Interannual variability of surface field is over the Indian Ocean during recent decades. *Monthly Weather Review*, 12: 1921–1935.

[62] Webster, P. J., 1994. The role of hydrological processes in ocean-atmosphere interaction. *Review of Geophysics*, 32: 427–476.

[63] Washington, W.M., R.M. Chervin and G. V. Rao, 1977. Effects of a variety of Indian Ocean surface temperature patterns on the summer monsoon circulation: Experiments with NCAR general circulation model. *Pure and Applied Geophysics*, 115: 1335–1356.

[64] Druyan, L.M., 1982. Studies of the Indian Summer Monsoon with a coarse-mesh general circulation model, Part I. Journal of Climatology, 1, 127–139

[65] Washington, W.M., 1981. A review of general circulation model experiments on the Indian monsoon. In: Monsoon Dynamics. Edited by J. lighthill and R.P. Pearce, *Cambridge University Press*, London, p. 111–130.

[66] Shukla, J., 1987. Interannual variability of monsoons. In: Monsoons editted by J.S. Fein and P.L. Stephens, *John Wiley and Sons*, New York, pp. 399–463.

[67] Shukla, K. R., and M.J. Fennesssy, 1994. Simulation and predictability of monsoons. Proc. Int. Conf. on Monsoon Variability and Prediction, Tech. Rep. WCRP-84, Geneva, Swizerland, World Climate Research Programme, 567–575.

[68] Shukla, J., 1975. Effect of Arabian Sea surface temperature anomaly on Indian summer monsoon. A numerical experiment with the GFDL model. *Journal of Atmospheric Science*, 32: 503–511.

[69] Kershaw, R., 1988: Effect of sea surface anomaly on a prediction of the onset of the southwest monsoon over India. *Quarterly Journal of Royal Meteorological Society*, 114: 325–345.

[70] Yang, S., and K. M. Lau, 1998. Influence of sea surface temperature and gound wetness on the Asian summer monsoon. *Journal of Climate*, 11: 3230–3246.

[71] Hatenrath, S. and Lamb, P.J., 1980. On the heat budget of hydrosphere and atmosphere in the Indian Ocean. Journal of Physical Oceangraphy, 10: 694–708.

[72] Golovastov, V.A., 1980. Peculiarities of ocean thermodynamics in the tropical Indian Ocean during the southwest monsoon 1979. *In: Results of Summer Monex Field Phase Research (Part B), FGGE Operations Report* Vol. 3, ICSU/WMO, 186–192.

[73] Golovastov, V.A., V.V. Pokudov and V.B. Kholmanov., 1982. Peculiarities of the water thermodynamics in the tropical Indian Ocean. *In: International Conference on the Scientific results of Monsoon Experiment.* Bali, Indonesia, October 1981. ICSU/WMO, 720–723.

[74] Wyrtki, K., Benonett, E.B., and Rochford, D.J., 1971. Oceanographic Atlas of the International Indian ocean Expedition, N.S.F., Washington, D.C., pp. 1–531.

[75] Colborn, J., 1976. The thermal structure of Indian Ocean, *The University Press of Hawaii*, Honolulu. 177 pp.

[76] Düing, W., A. Leetmaa, 1980. Arabian Sea cooling. a preliminary heat budget. *Journal of Physical Oceanography*, 10: 307–312.

[77] Sastry, J.S. and V. Ramesh Babu, 1984. Summercooling of the Arabian Sea - A review. *Proceedings of the Indian Academy of Sciences (Earth and Planetary Sciences)*, 94: 117–128.

[78] Murty, V.S.N., D.P. Rao and J.S. Sastry, 1983. The lowering of sea surface temperature in the east central Arabian Sea. *Mahasagar -Bulletin of the National Institute of Oceanography, Goa*, 16, 67–71.

[79] Shetye, S. R., 1986. A model study of the seasonal cycle of the Arabian Sea surface temperature. *Journal of Marine Research*, 44: 521–542.

[80] Kraus, E. B., and J. S. Turner, 1967. A one-dimensional model of the seasonal thermocline: II. The general theory and its consequences. *Tellus*, 19, 98–106.

[81] Denman., K. L., 1973. A time-dependent model of the upper ocean, *Journal of Physical Oceanography* 3, 173–184.

[82] Rao, R. R., 1986. Cooling and deepening of the mixed-layer in the central Arabian Sea during MONSOON-77: observation and simulation. *Deep-Sea Research A* 33: 1413-1424.

[83] McCreary, J. P., Jr., P. K. Kundu, and R. L. Molinari, 1993. A numerical investigation of dynamics, thermodynamics and mixedlayer processes in the Indian Ocean. *Progress in Oceanography*, Vol. 31, Pergamon, 181–244.

[84] Wacogne, S., Pacanowski, R., 1996. Seasonal heat transport in a primitive equations model of the tropical Indian Ocean. *Journal of Physical Oceanography* 26: 2666–2699.

[85] Loschning, J., and P. J. Webster, 2000. A coupled ocean-atmosphere system of SST modulation for the Indian Ocean, *Journal of Climate* 13: 3342-3360.

[86] Sigurdson, D.E., T. Dickey, D. Manov, 1995. Arabian Sea Mooring Data report: Deploiment # 1 October 15, 1994–April 20, 1995. Ocean Physics Laboratory, Santa barbara.

[87] Sigurdson, D.E., T. Dickey, D. Manov, 1996. Arabian Sea Mooring Data report: Deploiment # 2 April 22–October 20, 1995. *Ocean Physics Laboratory*, Santa barbara.

[88] Dickey, T.D., J. Marra, D. E. Sigurdson, R. A. Weller, S.S. Kinkade, S.E. Zedler, J.D. Wiggeri, C. Langdon, 1998. Seasonal variability of bio-optical and physical properties in the Arabian Sea: October 1994 - October 1995. *Deep Sea Research II*, 45: 2001-2025.

[89] Price, James F., Robert A. Weller, and Robert Pinkel, 1986. Diurnal cycling: Observations and models of the upper ocean response to diurnal heating, cooling, and wind mixing. *Journal of Geophysical Research*, 91(C7): 8411–8427.

[90] Gaspar, P., 1988. Modeling the seasonal cycle of the upper ocean. *Journal of Physical Oceanogaphy*, 18: 161–180.

[91] Mellor, G. L., and T. Yamada, 1974. A hierarchy of turbulence closure models for planetary boundary layers, *Journal of Atmospheric Science*, 31: 1791–1806.

[92] Bougeault, P., and P. Lacarrere, 1989. Parameterization of orography iduced turbulence in a meso-beta scale model, *Monthly Weather Review*, 117: 1872–1890.

[93] Gaspar, P., Y. Gregoris, and J. M. Lefevre, 1990. A simple Eddy Kinetic Energy Model for simulation of the Oceanic Vertical Mixing: Tests at station Papa and Long-Term Upper Ocean Study Site. *Journal of Geophysical Research* 95 C9: 16179–16193.

[94] Mellor, G. L., and T. Yamada, 1982. Development of a turbulence closure model for geophysical fluid problems, *Review of Geophysics*, 20: 851–875.

[95] Galperin, B., A. Rosati, L.H. Kantha, and G.L. Mellor. 1989. Modeling rotating stratified turbulent flows with application to oceanic mixed layers. *Journal of Physical Oceanography*, 19: 901–916.

[96] Levy, M., L. Memery and J-M. Andre, 1998. Simulation of primary production and export fluxes in the Northwestern Mediterranean Sea. *Journal of Marine Research* 56: 197–238.

[97] Pondaven P., D. Ruiz-Pino, C., Fravalo, P. Treguer, and C. Jeandel, 2000: Inter-annual variability of Si and N bio-geochemical cycles at the southern Ocean JGOFS station Kerfix, 1990–1995. *Deep-Sea research*, part I 47: 223-257.

[98] Blank, B., and P. Delecluse, 1993. Variability of the tropical Atlantic Ocean simulated by general circulation model with two different mixed layer physics. *Journal of Physical Oceanography* 23, 1363–1388.

[99] Gregg, M.C., H. Peters, J. C. Wesson, N. S. Oakey, and T. J. Shay, 1985. Intensive measurements of turbulence and shear in the equatorial undercurrent, *Nature*, 318, 140–144.

[100] Bougeault, P., and J. C. Andre, 1986. On the stability of the third-order turbulence closure for the modeling of the stratosumulus-topped boundary layer, *Journal of Atmospheric Science*, 43, 1574–1581.

[101] Paulson, C. A., J. J. Simpson, 1977. Irradiance measurements in the upper ocean, Journal of Physical Oceangraphy 7: 952–956.

[102] Jerlov, N. G., 1976. Marine Optics, *Elseveir Oceanography Series*, Vol. 14, 231 pp.

[103] Reynolds, R. W., and T. M. Smith, 1994. Improved global Sea Surface Temperature analysis using optimum interpolation. Journal of Climate 7: 929–948.

[104] Saji, N. H., B. N. Goswami, P. N. Vinayachandran, and T. Yamagata, 1999. A dipole mode in tropical Indian Ocean. *Nature* 401, 360–361.

[105] Sreejith, O. P. and S. S. C. Shenoi, 2002. An evaluation of satellite and in situ based sea surface temperature datasets in the North Indtian Ocean region. *International Journal of Remote Sensing*, Vol. 23, no. 24: 5165–5175.

[106] Carton, James. A., Gennady Chepurin, Xianhe Cao, and Benjamin Giese, 2000. A simple Ocean Data Assimilation Analysis of the Global Upper Ocean 1950-95, Part I: Methodology. *Journal of Physical Oceangraphy* 30: 294–309.

[107] Carton, James A., Gennady Chepurin, Xianhe Cao, and Benjamin Giese, 2000. A simple Ocean Data Assimilation Analysis of the Global Upper Ocean 1950–95, Part II: Results. *Journal of Physical Oceangraphy* 30: 311–326.

[108] ECMWF, European Centre for Medium-Range Weather Forecasts— *http://www.ecmwf.int*

[109] Helber, R. W. and R. H. Weisberg, 2001. Equatorial upwelling in the western Pacific warm pool. Journal of Geophysical Research, 106, C5: 8989 (2000JC000401).

[110] Friedrichs, Marjorie A. M., and Eileen E. Hofmann, 2001. Physical control of biological processes in the central equatorial Pacific Ocean. *Deep-Sea Research* I 48, 1023–1069.

[111] Morel, A., and S. Maritorena, 2001. Bio-optical properties of oceanic waters: A reappraisal. *Journal of Geophysical Research*, 106: 7163–7180.

[112] Babu, K.N., Rashmi Sharma, Neeraj Agarwal, Vijay K. Agrawal, and R. A. Weller, 2004. Study of the mixed layer depth variations within the north Indian Ocean using a 1-D model. *Journal of Jeophysical Research*, Vol. 109, C08016, doi:10.1029/2003JC002024.

[113] Kirk, J. T. O, 1994. Light and Photosynthesis in Aquatic Ecosystems. *Cambridge university press*, 509 p.

[114] Sathyendranath, S. and T. Platt, 1988. The spectral irradiance field at the surface and in the interior of the ocean: A model for applications in Oceanography and remote sensing. Journal of Geophysical Research 93 C8: 9270–9280.

[115] Parsons, T. R., M. takahashi, and B. Hargrave, 1984. Biological Oceanographic Processes, *Pergamon*, New York.

[116] Pedolosky, J., 1979. Geophysical Fluid Dynamics. *Springer*. 624pp.

[117] Fischer, A. S., 1997: Arabian Sea mixed layer deepening during the monsoon: Observation and dynamics. M.S. Thesis. *Masschusetts Institute of Thechnology and Woods Hole Oceanographic Institution*, Woods Hole, Massachusetts, 130 pp.

[118] Bruce, J.G, D. R. Johnson, and J. C. Kindle, 1994: Evidence for eddy formation in the eastern Arabian Sea during the northeast monsoon, Journal of Geophysical Research, 99: 7651–7664.

[119] Keen, T. R., J. C. Kindle, and D. K. Young, 1997. The interaction of southwest monsoon upwelling , advection and primary production in the northwest Arabian Sea, *Journal of Marine System*, 13: 61–82.

[120] Miller, J. R., 1976. The salinity effect in a mixedlayer ocean model, *Journal of Physical Oceanography*, Vol. 6, No. 1: 29-35.

[121] Millero, F.S., and A. Poisson, 1981. An international one-atmosphere equation of state of sea-water. *Deep Sea Research*, 28A, 625–629.

[122] Hastenrath, S., 1982: On meridional heat transports in the World ocean. *Journal of Oceanography*, 12: 922–927.

[123] Barnett, T.P., 1984: Long-term trends in surface temperature over the oceans. *Monthly Weather Review*, 112. 303–312.

[124] Gopinathan, C.K. and J.S. Sastry, 1986. Is the summer monsoon rainfall over India related to the Bay of Bengal SST? Presented at the Seminar on Long-range forecasting of monsoon rainfall, *India Meteorological Society*, New Delhi, April 16–18.

[125] Gopinathan, C.K. and D.P. Rao, 1985. Surface temperature of the Indian Ocean before summer monsoon. *Mahasagar -Bulletin of the National Institute of Oceanography*, Goa, 18: 281–292.

[126] Rochford, Peter A., John C. Kindle, Patrik C. Gallacher, and Robert A. Weller, 2000. Sensitivity of the Arabian Sea mixed layer to 1994-1995 operational wind products. *Journal of Geophysical Research*, Vol. 105, No. C6: 14141–14162.

[127] Pedolosky, J., 1979. *Geophysical Fluid Dynamics*. Springer. 624pp.

[128] Prashad, T. G., 2004. A comparison of mixed-layer dynamics between the Arabian Sea and the Bay of Bengal: One-dimensional model results. *Journal of Geophysical Research*, Vol. 109, C03035, doi:10.1029/2003JC002000.

[129] Ekman, V.W., 1905. On the influence of the earth's rotation on ocean currents. *Ark. Mat. Astron. Fys.* 2, No. 11.

[130] Andreson, S. P., R. A. Weller, and R. B. Weller, 1996. Surface buoyancy forcing and the mixed layer of the western Pacific warm pool: Observations and one-dimensional model results. *Journal of Climate*, 9: 3056–3085.

[131] Kitaygorodskiy, S. A., 1961. On the possibility of theoretical calculation of vertical temperature profile in upper layer of the sea. *Izv. Akad. Nauk SSSR, Ser. Geofiz.*, No. 1–6: 313–318.

[132] Adamec, D., R. L. Elsberry, R.W. Garwood, and R. L. haney, 1981. An embedded mixed-layer-ocean circulation model. *Dynamics of Atmosphere and Oceans*, 6: 69–77.

[133] Niller, P.P., and E. B. Kraus, One-dimensional models of the upper ocean, 1977. *Modelling and prediction of the upper layers of the ocean*, edited by E. B. Kraus, pp. 143–172, Pergamon, New York.

[134] Peters, H., M.C. Gregg, and J. M. Toole, 1988. On the parameterization of equatorial turbulence, Journal of Geaphysical research, 93: 1199–1218.

[135] Arakawa, A., 1972. Design of the UCLA general circulation model. Numerical simulation of weather and climate. Technical Report 7, Dept. of Meteorology, University of califernia, Los Angeles, CA, 116 pp.